

KAUNAS UNIVERSITY OF TECHNOLOGY

NASEHA WAFI QAMMAR

ADVANCED MATRIX BASED ALGORITHMS  
IN THE ANALYSIS OF THE ECG SIGNALS  
FOR CARDIAC DISEASE DETECTION AND  
MONITORING

Doctoral dissertation  
Natural Sciences, Informatics (N 009)

2025, Kaunas

The dissertation has been prepared at the Department of Mathematical Modelling of the Faculty of Mathematics and Natural Sciences of Kaunas University of Technology in 2021–2025. The research has been sponsored by the Research Council of Lithuania.

The doctoral right has been granted to Kaunas University of Technology together with Vytautas Magnus University and Vilnius Gediminas Technical University.

**Research supervisor:**

Prof. Dr. Hab. Minvydas Kazys RAGULSKIS (Kaunas University of Technology, Natural Sciences, Informatics, N 009).

**Edited by:** English language editor Birutė Jurkšaitė (Publishing House *Technologija*), Lithuanian language editor Aurelija Gražina Rukšaitė (Publishing House *Technologija*).

**Dissertation Defence Board of Informatics Science Field:**

Prof. Dr. Hab. Rimantas BARAUSKAS (Kaunas University of Technology, Natural Sciences, Informatics, N 009) – **chairperson**;

Prof. Dr. Dalia ČALNERYTĖ (Kaunas University of Technology, Natural Sciences, Informatics, N 009);

Prof. Dr. Hamid Reza KARIMI (Politecnico di Milano, Italy, Natural Sciences, Informatics, N 009);

Assoc. Prof. Dr. Mantas LANDAUSKAS (Kaunas University of Technology, Natural Sciences, Informatics, N 009);

Prof. Dr. Vadimas STARIKOVIČIUS (Vilnius Gediminas Technical University, Natural Sciences, Informatics, N 009).

The dissertation defence will be held on 26 August 2025, at 10 a.m. in a public meeting of the Dissertation Defence Board of the Informatics science field at the Rectorate Hall of Kaunas University of Technology.

Address: K. Donelaičio 73-402, LT-44249 Kaunas, Lithuania

Phone: (+370) 608 28 527; e-mail [doktorantura@ktu.lt](mailto:doktorantura@ktu.lt)

The dissertation was sent on 25 July 2025.

The dissertation is available on the website <http://ktu.edu> and at the libraries of Kaunas University of Technology (Gedimino 50, LT-44239 Kaunas, Lithuania), Vytautas Magnus University (K. Donelaičio 52, LT-44244 Kaunas, Lithuania) and Vilnius Gediminas Technical University (Saulėtekio 14, LT-10223 Vilnius, Lithuania).

© N.W. QAMMAR, 2025

KAUNO TECHNOLOGIJOS UNIVERSITETAS

NASEHA WAFA QAMMAR

PAŽANGŪS MATRICA PAGRĮSTI  
ALGORITMAI ANALIZUOJANT EKG  
SIGNALUS ŠIRDIES LIGOMS APTIKTI IR  
STEBĖTI

Daktaro disertacija  
Gamtos mokslai, informatika (N 009)

Kaunas, 2025

Disertacija rengta 2021–2025 metais Kauno technologijos universiteto Matematikos ir gamtos mokslų fakultete, Matematinio modeliavimo katedroje. Mokslinius tyrimus rėmė Lietuvos mokslo taryba.

Doktorantūros teisė Kauno technologijos universitetui suteikta kartu su Vytauto Didžiojo universitetu ir Vilniaus Gedimino technikos universitetu.

**Mokslinis vadovas:**

prof. habil. dr. Minvydas RAGULSKIS (Kauno technologijos universitetas, gamtos mokslai, informatika, N 009).

**Informatikos mokslo krypties disertacijos gynimo taryba:**

prof. habil. dr. Rimantas BARAUSKAS (Kauno technologijos universitetas, gamtos mokslai, informatika, N 009) – pirmininkas;

prof. dr. Dalia ČALNERYTĖ (Kauno technologijos universitetas, gamtos mokslai, informatika, N 009);

prof. dr. Hamid Reza KARIMI (Milano politechnikos universitetas, Italija, gamtos mokslai, informatika, N 009);

doc. dr. Mantas LANDAUSKAS (Kauno technologijos universitetas, gamtos mokslai, informatika, N 009);

prof. dr. Vadimas STARIKOVIČIUS (Vilniaus Gedimino technikos universitetas, gamtos mokslai, informatika, N 009).

Disertacija bus ginama viešame Informatikos mokslo krypties disertacijos gynimo tarybos posėdyje 2025 m. rugpjūčio 26 d. 10:00 val. Kauno technologijos universiteto Rektorato salėje.

Adresas: K. Donelaičio g. 73-402, LT-44249 Kaunas, Lietuva.

Tel: (+370) 608 28 527; el. paštas [doktorantura@ktu.lt](mailto:doktorantura@ktu.lt)

Disertacija išsiųsta 2025 m. liepos 25 d.

Su disertacija galima susipažinti interneto svetainėje <http://ktu.edu>, Kauno technologijos universiteto bibliotekoje (Gedimino g. 50, LT-44239 Kaunas, Lietuva), Vytauto Didžiojo universiteto bibliotekoje (K. Donelaičio g. 52, LT-44244 Kaunas, Lietuva) ir Vilniaus Gedimino technikos universiteto bibliotekoje (Saulėtekio al. 14, LT-10223 Vilnius, Lietuva).



## CONTENTS

LIST OF TABLES.....	7
LIST OF FIGURES.....	8
LIST OF ABBREVIATIONS.....	11
INTRODUCTION.....	12
1. INTRODUCTION TO CARDIAC DISEASE DETECTION, MONITORING AND METHODS.....	17
1.1 Overview, Impact and Importance of Early Detection and Monitoring of Cardiac Diseases.....	17
1.2 Electrocardiogram (ECG) Signals for Diagnosis and Monitoring.....	18
1.3 Complexity in the Self-Organisation of the Human Cardiovascular System..	19
1.4 Interconnectedness of the Regulatory, the Executive, and the Supply system in the Human Body.....	20
1.5 Non-linear Nature of the Cardiovascular System .....	22
1.6 Perfect Matrices of Lagrange Differences as a Robust Algorithm for ECG Analysis.....	23
1.7 Hankel Matrix-Based Algorithm for Complex Signal Analysis.....	27
1.8 Embedding Techniques for Capturing System Dynamics in the State Space ..	33
1.9 Permutation Entropy for Complex Time Series Analysis .....	34
1.10 Wavelet Techniques for Complex Time Series Analysis.....	35
2. EXPLORING AND EXTENDING MATHEMATICAL METHODS FOR COMPLEX TIME SERIES ANALYSIS.....	37
2.1 Configurable Structure of PMLD for Enhanced ECG Analysis .....	37
2.2 Improving PMLD Sensitivity and Variability Using Higher-Order Matrix Expansion .....	38
2.3 Comparative Analysis: PMLD vs. SMF1 and SMF2.....	39
2.4 Second-Order Time-Delayed Pattern Matrices for Multivariate Time Series Analysis. ....	40
2.5 Calibration of the H-Rank Algorithm Based on Coupled Logistic Maps .....	42
2.6 Statistical Methods for Generating Variation Intervals for Classification and Health Biomarkers .....	45
3. ALGORITHMS AND APPLICATIONS IN CARDIAC SIGNAL ANALYSIS.....	50
3.1 PMLD Matrix-Based Algorithm for Cardiovascular Complexity Collapse during Stress Tests (Load Phase).....	50
3.2 Matrix-Based Algorithm for Complexity Collapse and Cardiovascular Self-Organisation during the Stress Test (the Load and Recovery Phases) .....	63
3.3 Comparative Analysis of Matrix-Based Algorithms for ECG Parameter Analysis.....	79
3.4 Matrix-Based Algorithm for the Detection of Atrial Fibrillation (PMF Expandability from Second- to Fifth-Order).....	84
3.5 Matrix-Based Algorithm for HRV Analysis in Psychological Synchronisation during Meditation .....	92

4.	LIMITATIONS AND FUTURE RESEARCH.....	104
5.	CONCLUSIONS .....	105
6.	SANTRAUKA.....	106
6.1	Įvadas.....	108
6.2	Sudėtingos laiko eilučių analizės matematinių metodų tyrinėjimas ir išplėtimas .....	109
6.3	Širdies signalų analizės algoritmai ir taikymas .....	115
6.4	Išvados.....	126
	REFERENCES .....	127
	CURRICULUM VITAE.....	136
	LIST OF PUBLICATIONS AND CONFERENCES .....	137
	ACKNOWLEDGEMENTS .....	138
	ANNEX.....	139
A.	BIOETHICAL PERMIT BE-1-30 (ORIGINAL) .....	139
B.	BIOETHICAL PERMIT BE-1-30 (TRANSLATED) .....	140
C.	BIOETHICAL PERMIT BE-2-4 (ORIGINAL) .....	141

## LIST OF TABLES

<b>Table 1.</b> Reconstruction of H-rank for the perturbed sequence across varying $\varepsilon$ values.....	31
<b>Table 2.</b> Slope Coefficients and Spearman's Rank Correlation Coefficients for Healthy Individuals during Load and Recovery Phases.....	55
<b>Table 3.</b> Slope Coefficients and Spearman's Rank Correlation Coefficients for Unhealthy Individuals during Load and Recovery Phases.....	56
<b>Table 4.</b> Statistical Conditions for Discerning Significance in Different Phases of the Stress Test.....	57
<b>Table 5.</b> Triangular System Inclusion Criteria for the Slope Coefficient of the New Candidate.....	58
<b>Table 6.</b> Derivation of the Health Indicator Alpha for all Participants in the Study Group.....	67
<b>Table 7.</b> Derivation of the Health Indicator Beta for all Participants in the Study Group.....	67
<b>Table 8.</b> Integration of Health Indicators Alpha and Beta into the Decision Aid System Based on Gamma Values .....	72
<b>Table 9.</b> Variance Metrics for Healthy Candidates in PMF, SMF1, and SMF2.....	82
<b>Table 10.</b> Variance Metrics for Unhealthy Candidates in PMF, SMF1, and SMF2..	83
<b>Table 11.</b> Variance Values of Scalar Time Series Generated by Second- to Fifth-Order PMF for Healthy Individuals .....	86
<b>Table 12.</b> Variance Values of Scalar Time Series Generated by Second- to Fifth-Order PMF for Unhealthy Individuals .....	86
<b>Table 13.</b> Classification Criteria for Decision Support System Development .....	89
<b>Table 14.</b> Healing Meditation Phases: Timing and Descriptions.....	95
<b>Table 15.</b> Statistical Metrics of HRV Data Across Nine Phases of Meditation .....	100
<b>Table 16.</b> Statistical Conditions Across Meditation Phases .....	100
<b>17 lentelė.</b> Sveikų kandidatų dispersijos metrika PMF SMF1 ir SMF2.....	122

## LIST OF FIGURES

<b>Fig. 1.</b> Schematic Diagram Illustrating the Interconnections between the Regulatory, Executive, and Supply Systems [53].....	21
<b>Fig. 2.</b> Diagram Illustrating the Computation of Time-Delay Patterns between Time Series ( $x$ ) and ( $y$ ) Highlighting the Algorithm for Analysing their Temporal Relationships .....	41
<b>Fig. 3.</b> The Master–Slave Coupled Logistic Map: Time Series of the Master System (Red) and the Slave System (Blue); the Coupling Parameter; their Difference; and the H-ranks Computed for the Slave (Blue) and the Master (Red) .....	44
<b>Fig. 4.</b> Simplified Model of Executive, Supply, and Regulatory Systems for Analysing Heart Rate and Blood Pressure Variations during the Stress Test.....	51
<b>Fig. 5.</b> Structure of the Computation Setup .....	53
<b>Fig. 6.</b> Cardiovascular Dynamics of Healthy Individual H10: (a) RR Interval and JT Wave Dynamics, (b) Arterial Blood Pressure Regulation, (c, d) ABP and Heart Rate Phase Relationship .....	59
<b>Fig. 7.</b> Cardiovascular Dynamics of Unhealthy Individual U4: (a) RR Interval and JT Wave, (b) ABP Regulation, (c, d) ABP and Heart Rate Phase Relationship .....	60
<b>Fig. 8.</b> Gaussian Distribution Curves: (a) Load Phase Slope Coefficients for Healthy (green) vs. Unhealthy (magenta) Individuals; (b) Recovery Phase Slope Coefficients for the Same Groups.....	61
<b>Fig. 9.</b> Test Candidate 1 Analysis: (a) Heart Rate and ABP Variations, (b) Relative Changes During Load Phase, (c) Candidate’s Position in Variation Interval, (d) Blood Pressure Regulation Trajectory.....	62
<b>Fig. 10.</b> Test Candidate 2 Analysis: (a) Heart Rate and ABP Variations, (b) Relative Changes During Load Phase, (c) Candidate’s Position in Variation Interval, (d) Blood Pressure Regulation Trajectory.....	63
<b>Fig. 11.</b> Computational Results for Healthy Subject Denoted as HA: (Subplot A) RR Intervals, (Subplot B) JT Intervals, (Subplot C) Normalised Intervals, (Subplot D) Difference Signal and Adaptation Index, (Subplot E) Delay Pattern and Modified Index, (Subplot F) Shan Wavelet Analysis.....	68
<b>Fig. 12.</b> Computational Results for Healthy Subject Denoted as HB: (Subplot A) RR Intervals, (Subplot B) JT Intervals, (Subplot C) Normalised Intervals, (Subplot D) Difference Signal and Adaptation Index, (Subplot E) Delay Pattern and Modified Index, (Subplot F) Shan Wavelet Analysis.....	69
<b>Fig. 13.</b> Computational Results for Healthy Subject Denoted as HC: (Subplot A) RR Intervals, (Subplot B) JT Intervals, (Subplot C) Normalised Intervals, (Subplot D) Difference Signal and Adaptation Index, (Subplot E) Delay Pattern and Modified Index, (Subplot F) Shan Wavelet Analysis.....	70
<b>Fig. 14.</b> Computational Results for Healthy Subject Denoted as HD: (Subplot A) RR Intervals, (Subplot B) JT Intervals, (Subplot C) Normalised Intervals, (Subplot D) Difference Signal and Adaptation Index, (Subplot E) Delay Pattern and Modified Index, (Subplot F) Shan Wavelet Analysis.....	71

<b>Fig. 15.</b> Computational Results for Unhealthy Subject Denoted as UA: (Subplot A) RR Intervals, (Subplot B) JT Intervals, (Subplot C) Normalised Intervals, (Subplot D) Difference Signal and Adaptation Index, (Subplot E) Delay Pattern and Modified Index, (Subplot F) Shan Wavelet Analysis .....	73
<b>Fig. 16.</b> Computational Results for Unhealthy Subject Denoted as UB: (Subplot A) RR Intervals, (Subplot B) JT Intervals, (Subplot C) Normalised Intervals, (Subplot D) Difference Signal and Adaptation Index, (Subplot E) Delay Pattern and Modified Index, (Subplot F) Shan Wavelet Analysis .....	74
<b>Fig. 17.</b> Computational Results for Unhealthy Subject Denoted as UC: (Subplot A) RR Intervals, (Subplot B) JT Intervals, (Subplot C) Normalised Intervals, (Subplot D) Difference Signal and Adaptation Index, (Subplot E) Delay Pattern and Modified Index, (Subplot F) Shan Wavelet Analysis .....	75
<b>Fig. 18.</b> Computational Results for Unhealthy Subject Denoted as UD: (Subplot A) RR Intervals, (Subplot B) JT Intervals, (Subplot C) Normalised Intervals, (Subplot D) Difference Signal and Adaptation Index, (Subplot E) Delay Pattern and Modified Index, (Subplot F) Shan Wavelet Analysis .....	76
<b>Fig. 19.</b> Overall Health Status of Healthy Person (HA) Using Semi-Gauge Indication Tool.....	76
<b>Fig. 20.</b> Overall Health Status of Unhealthy Person (UA) Using Semi-Gauge Indication Tool .....	77
<b>Fig. 21.</b> Structure of the Computational Setup: (A) Mathematical Computations, (B) Statistical Techniques, (C) Probabilistic Evaluation and Biomarker Significance ...	85
<b>Fig. 22.</b> Gaussian Distribution: (a) 3 <sup>rd</sup> -Order PMF Distribution, (b) 5 <sup>th</sup> -Order PMF Distribution; Black Horizontal Arrows Denote Variation Intervals .....	88
<b>Fig. 23.</b> Test Candidate 1 Classification: 3 <sup>rd</sup> - and 5 <sup>th</sup> -Order PMF Architecture.....	91
<b>Fig. 24.</b> Test Candidate 2 Classification: 3 <sup>rd</sup> - and 5 <sup>th</sup> -Order PMF Architecture.....	92
<b>Fig. 25.</b> HRV Monitoring for Eight Healers and One Healee: Blue Plots represent Healers' RR Intervals, Red Plot represents Healee's RR Intervals; Time Series Analysed Throughout the Experiment .....	96
<b>Fig. 26.</b> H-Ranks Graph Throughout the Experiment: (a) H-Ranks of Eight Healers (Blue), (b) Mean H-Rank of Healers (Black), (c) H-rank of Healee (Red) .....	97
<b>Fig. 27.</b> H-Ranks Graph for Participants: (a) Mean H-Ranks of Eight Healers (Black), (b) Healee's H-Ranks (Red) .....	98
<b>Fig. 28.</b> Embedded Attractors and Phase Plane Representation: Nine Trajectories for 4,500 Seconds (75 minutes); Red for Healee (Starting at the Magenta Circle), Black for Healers (Starting at the Green Circle) .....	99
<b>Fig. 29.</b> Statistical Analysis of H-Rank: Box Plots for Nine Experiment Phases. The Red Box Plots Represent the Healee and the Black Box Plots Represents the Healers .....	101
<b>Fig. 30</b> HRV Complexity via Permutation Entropy (PE).....	102
<b>31 pav.</b> Kandidato atlikto testo analizė.....	116
<b>32 pav.</b> Sveiko subjekto skaičiavimo rezultatai žymimi kaip $H_A$ .....	118
<b>33 pav.</b> Testo kandidatų klasifikacija: 3 ir 5 eilės PMF architektūra .....	123

**34 pav.** Dalyvių H reitingų grafikas: (a) aštuonių gydytojų vidutiniai H reitingai (juoda), (b) Healee H reitingai (raudona).....124

## **LIST OF ABBREVIATIONS**

ABP – arterial blood pressure  
ANS – autonomic nervous system  
AP – amplitude of the P wave, the height of the P wave reflecting atrial depolarisation  
CNS – central nervous system  
CVD – cardiovascular disease  
CWT – continuous wavelet transform  
DP – duration of the P wave, the time interval representing atrial depolarisation  
DWT – discrete wavelet transform  
ECG – electrocardiogram  
HR – heart rate  
HRV – heart rate variability  
IBI – inter-beat interval  
JT – duration of the JT wave, the interval between the J point and the end of the T wave  
LRS – linear recurrence sequence  
MA – moving average  
PE – permutation entropy  
PMF – primary matrix framework  
PMLD – perfect matrices of Lagrange differences  
QRS – duration of the QRS complex, representing ventricular depolarisation  
RR – inter-beat interval, the time between consecutive R wave peaks in the ECG  
RMSE – root mean square error  
SMF – secondary matrix framework  
SVD – singular value decomposition  
VN – vagus nerve  
WHO – World Health Organisation  
WMA – weighted moving average

# INTRODUCTION

## Relevance of the Topic

The dissertation aims to address the growing need for innovative computational methods analysing complex biomedical time series, specifically electrocardiogram (ECG) signals. From a conceptual standpoint, the human body may be viewed as a dynamic collection of interconnected systems that work together to maintain internal stability and general health. The circulatory system, in particular, illustrates the intricacy of this arrangement by performing vital functions such as carrying oxygen and nutrients, stabilising body temperature, and removing waste materials to ensure optimal physiological performance [1]. Its proper performance is vital to maintaining life, as even minimal disruptions can lead to serious health complications, such as cardiac arrhythmias and sudden cardiac arrests [2]. Given its importance, the precise diagnosis and monitoring of cardiovascular abnormalities remain a top priority in medical research. Electrocardiogram (ECG) readings, which describe the electrical activity of the heart, are a vital diagnostic tool in this case. However, the issue lies in the intrinsic diversity and complexity of these signals, which can be influenced by many physiological and external factors [3].

Over the years, various mathematical, statistical, and artificial intelligence techniques have been developed to analyse ECG signals, and these methods have proven valuable for diagnostic purposes. However, there is always room for improvement, particularly because traditional techniques often struggle to detect subtle variations in the cardiovascular system. For example, each individual exhibits a distinct physiological profile throughout their life, with heartbeat dynamics that continuously vary and never replicate exactly over time [4, 5]. While the foundational anatomy of the human body remains consistent across individuals, physiological characteristics display significant differences [6]. These variations are also pronounced in the cardiovascular system, which is uniquely adapted to each person's genetic and lifestyle influences [6, 7]. Such complex variability underscores the complexity of the human body, making the study of cardiovascular function and its implications both challenging and fascinating [8, 9]. This challenge is especially pronounced when dealing with non-linear and non-stationary data, which are common characteristics of real-world cardiac signals [10]. For example, traditional time-domain and frequency-domain analyses may not fully capture the non-linear dynamics of cardiac signals [11]. These methods focus on identifying characteristic features associated with arrhythmias, often neglecting the nuances of short-term fluctuations, which can be critical for accurately diagnosing transient arrhythmic episodes. Additionally, numerous advanced and effective machine-learning methods have been developed and applied to ECG signal analysis [12]. However, the majority of these machine-learning models depend heavily on large-scale datasets for training purposes. While it is well established that many effective AI-based and traditional methods have been employed for ECG analysis, it is equally important to acknowledge that these methods come with certain limitations. These limitations often relate to the failure to detect subtle individual variations in ECG signals [13]. When the goal is to capture such subtle variations, matrix-based algorithms can be highly



effective for analysing small-scale ECG datasets. The application of these algorithms could significantly enhance the detection of arrhythmias and other cardiac irregularities, even in scenarios with limited data availability.

The use of advanced matrix-based algorithms, such as the perfect matrices of Lagrange differences (PMLD), Hankel matrices, the Secondary Matrix Framework (SMF), Second-Order Time-Delayed PMLD matrices, in combination with a set of simple-to-advanced statistical techniques, is of particular relevance due to their capability to extract, quantify, and interpret subtle variations in physiological signals that are often indicative of underlying cardiac conditions. These techniques provide a higher resolution of the structural changes in ECG signal patterns, facilitating the detection of irregularities in heart rhythms that are often missed by conventional and other popular techniques.

The dissertation also aims to conduct a detailed comparison of the suggested matrix-based approaches with other existing techniques, such as Singular Value Decomposition (SVD), Linear Recurrence Sequences (LRS), and Permutation Entropy (PE). This comparison is critical for understanding the strengths and limitations of each approach in dealing with non-linear and non-stationary properties of ECG data. Also, the proposed health indicators derived from the matrix frameworks and statistical techniques are another innovative aspect of this research. Such indicators provide quantifiable measures of cardiac health status, which can be directly used by clinicians to identify cardiac diseases and assess their progress.

**The object of this investigation** is to develop and analyse matrix-based algorithms for analysing ECG parameters, including their algebraic relationships and applications for detecting short-term fluctuations occurring in the cardiovascular system.

**The aim of this investigation** is to propose and validate matrix-based algorithms for ECG time-series analysis and to develop a machine-trained model using the intelligent indicators necessary for the early diagnosis of various cardiovascular conditions.

### **Objectives**

1. To investigate the algebraic interrelationships between the ECG parameters (RR, JT) for the early detection of cardiovascular processes (known as the collapse of complexity, which occurs at the end of the load phase during the stress test) by applying the Second-Order PMLD matrix-based algorithm along with other statistical analysis techniques.
2. To explore the algebraic interrelationships between the ECG parameters (RR, JT) for the early detection of cardiovascular processes (the self-organisation of the cardiovascular system, which occurs throughout the stress test, and the collapse of complexity, which occurs at the end of the load phase) by using the Second-Order Time-Delayed PMLD matrix-based algorithm and a series of statistical analysis methods.
3. To evaluate the performance of the introduced PMLD matrix-based algorithms against two other matrix-based algorithms (SMF1 and SMF2) in

static ECG analysis for detecting atrial fibrillation episodes by analysing the algebraic interrelationships among three ECG parameters (RR, JT, QRS).

4. To investigate the expandable structure of the PMLD analysis for detecting atrial fibrillation episodes by analysing the algebraic interrelationships among five ECG parameters (RR, JT, QRS, AP, DP) using the PMLD algorithm and other statistical computational techniques.
5. To analyse the RR inter-beat interval using the Hankel matrix-based approach for detecting complexity-matching phenomena during the guided meditation activity.

### **The Novelty of the Work and its Practical Importance**

The novelty of this thesis lies in the development and application of matrix-based algorithms to analyse the algebraic relationships between ECG parameters, thus providing new insights into short-term fluctuations occurring in the cardiovascular system that are often overlooked by traditional methods. The proposed algorithms are compared with existing mathematical approaches, thereby highlighting their enhanced sensitivity to subtle variations in ECG signals. These analyses contribute to the development of a machine-learning model for classification purposes, thus offering a novel approach to detecting and diagnosing underlying cardiac conditions. Furthermore, the integration of decision support systems emphasises their practical application, facilitating improved clinical decision-making and enhancing diagnostic accuracy in real-world medical scenarios.

### **Methods, Software, and Experimental Tools**

In this thesis, the ECG capturing methods were facilitated by two main collaborators. The collaboration with the Department of Cardiology at the Lithuanian University of Health Sciences (LSMU) facilitated the use of the Kaunas Load system for ECG data acquisition [14]. This system captures 12-lead ECG parameters either during stress tests or at rest. The collected ECG data are recorded into a computer system, where they undergo an expert review by a medical professional. The expert inspects the ECG recordings, adjusts any necessary settings, and ultimately generates results, which are saved in a text file for further analysis.

Additionally, through collaboration with the HeartMath Institute, 24-hour ambulatory HRV recordings were obtained using high-resolution HRV recorders. Ambu Blue Sensor L microporous disposable electrodes were applied in a modified V5 position. The RR inter-beat intervals were calculated from the electrocardiogram at a sampling rate of 1000 Hz, and the RR intervals were stored in the HRV recorder's memory. Subsequently, the HRV data were downloaded to a workstation, where they were edited for artefacts caused by movement and ectopic beats using DADiSP 6.7.

MATLAB was chosen as the primary software tool for the development of all algorithms and to perform all computations in this thesis. Its built-in features, high computational efficiency, and user-friendly interface made it well-suited for the rapid analysis of ECG parameters.

### **Provided for the Defence**

This thesis presents matrix-based algorithms for analysing and evaluating the algebraic relationships among ECG parameters. The following algorithms are proposed for this purpose:

1. Perfect Matrices of Lagrange Differences: While these have previously been analysed for the second-order matrix using only two ECG parameters, their applicability is now extended to higher orders, which enhances ECG analysis.
2. Two other matrix architectures are also analysed for ECG analysis. Their performance is evaluated based on their ability to satisfy the PMLD matrix criteria, ensuring that these matrices qualify as optimal matrices. Once these matrix architectures are confirmed to adhere to the PMLD rules, they are further assessed for their scalability, including the potential to increase matrix size, adapt to varying degrees of freedom, and accommodate expandable dimensions.
3. Second-Order Time-Delayed PMLD Matrix Algorithm: This matrix-based algorithm offers another unique representation of the PMLD matrix architecture, specifically designed for ECG analysis.
4. Hankel Matrix-Based Algorithm: In this thesis, this matrix-based algorithm is adapted for identifying the complexity-matching phenomenon.

These proposed matrix-based algorithms provide a new framework for analysing ECG parameters, particularly in understanding short-term fluctuations occurring within the human cardiovascular system. A key advantage of these algorithms is their ability to function effectively with small datasets—a feature rarely achieved with current artificial intelligence models, which typically require large datasets for accurate performance. Moreover, the outcomes of these matrix-based algorithms are compared with existing mathematical algorithms to assess their relative effectiveness.

### **Approbation of the Results**

This thesis is based on four scientific publications and one extensive computational work conducted on the HRV data. The four articles have been published in high-impact journals (Q1 and Q2) indexed by the Web of Science (WoS). These papers contribute key findings to the following fields:

1. Qammar et al. (2022) examine the complexity of arterial blood pressure regulation during stress tests (*Diagnostics*, 12(5), p. 1256).
2. Qammar et al. (2024) explore the early diagnosis of self-organisation issues in the cardiovascular system by analysing the relationship between the RR and JT intervals (*Diagnostics*, 14(13), p. 1410).
3. Qammar et al. (2022) address the detection of atrial fibrillation episodes through 3D algebraic relationships between cardiac intervals (*Diagnostics*, 12(12), p. 2919).
4. Qammar et al. (2024) present a comparative analysis of matrix architectures for the early diagnosis of atrial fibrillation episodes (*Applied Sciences*, 14(14), p. 6191).

5. The computational work performed on the HRV data presents the mathematical characterisation of complexity matching during a healing circle meditation.

The results of the dissertation have been presented at two international conferences:

1. **65<sup>th</sup> Scientific and Technical Conference on Biomedical Engineering**

Riga Technical University (RTU), Riga, Latvia

Date: 22 April 2024

Title: *Understanding the Complexity of Arterial Blood Pressure Regulation through the Lens of Perfect Matrices of Lagrange Differences*

Presentation format: Oral presentation.

2. **Heart Rhythm Congress (HRC)**

International Convention Centre, Birmingham, UK

Date: 7 October 2024

Title: *Enhancing Atrial Fibrillation Detection: A Multifaceted Computational Approach Incorporating Higher-Order Perfect Matrices of Lagrange Differences (PMLD) and Decision Support Systems*

Presentation format: Poster presentation (published in the *European Journal of Arrhythmia & Electrophysiology* (2024; 10))

Presenting author: Naseha Wafa Qammar

Co-author: Minvydas Ragulskis

### **The Size and Structure of the Dissertation**

This doctoral dissertation contains an introduction section, four main chapters, and concluding insights from those chapters, as well as the overall conclusion of the thesis, limitations and future research directions, a summary in Lithuanian, a bibliography, and a list of publications. The volume of the dissertation is 142 pages. It contains 30 figures and 16 tables. A total of 149 sources are cited in the thesis.

# **1. INTRODUCTION TO CARDIAC DISEASE DETECTION, MONITORING AND METHODS**

## **1.1 Overview, Impact and Importance of Early Detection and Monitoring of Cardiac Diseases**

Cardiac diseases remain the leading cause of mortality and morbidity worldwide and account for a significant burden on the healthcare system. According to the World Health Organization (WHO) report, cardiovascular diseases (CVDs) are responsible for an estimated 17.9 million deaths each year, representing 31 per cent of all global deaths [15]. The increasing prevalence of risk factors such as hypertension, diabetes, obesity, and smoking, to name a few, has further exacerbated this global health crisis [16]. The economic impact of CVDs is likewise substantial; for instance, high treatment costs place additional pressure on healthcare systems overall [16]. Cardiac diseases encompass a wide range of conditions, including, but not limited to, coronary artery disease, heart failure, arrhythmias, and valvular heart diseases, each with its own set of diagnostic challenges. Coronary artery disease, characterised by the narrowing or blockage of coronary arteries, is one of the most common forms and can lead to life-threatening events such as myocardial infarction [17]. Heart failure, a condition in which the heart is unable to pump blood effectively, affects millions of individuals globally and significantly reduces the quality of life, as well as the life expectancy, of patients already diagnosed with cardiac diseases [18, 19]. In summary, the challenges posed by these diseases clearly underscore the importance of advanced and reliable diagnostic methods in improving overall patient health outcomes [20].

Early detection and monitoring of cardiac diseases is essential in preventing severe complications and improving survival rates. The progression of cardiac conditions can often be subtle, meaning that patients remain asymptomatic until the disease has progressed significantly [21]. However, timely diagnosis allows for the initiation of preventive measures and interventions that can slow down disease progression. For instance, early identification of atherosclerosis through imaging techniques and biomarkers can guide the implementation of lifestyle modifications and pharmacological therapies to reduce the risk of developing cardiovascular-related problems [22]. It is well known that advancements in diagnostic technologies have already revolutionised the field of cardiology. Non-invasive imaging modalities such as echocardiography, cardiac magnetic resonance imaging (MRI), and computed tomography (CT) can provide detailed anatomical and functional information, thereby allowing clinicians to diagnose conditions with greater accuracy and confidence [23]. Likewise, wearable devices and telemonitoring systems have also emerged as powerful tools for continuous cardiac monitoring, providing real-time data that can be used to detect arrhythmias, monitor heart rate variability, and remotely manage chronic cardiac conditions [24]. These innovations have made cardiac care more accessible and have the potential to transform the management of cardiovascular diseases compared to a few years ago [25]. In addition to imaging, the penetration of health biomarkers in cardiac disease diagnosis has also gained significant attention. Cardiac troponins, for example, are well-established markers for myocardial

infarction and have become the cornerstone of acute coronary syndrome diagnosis [26]. The integration of genetic and molecular diagnostics is also paving the way for personalised medicine approaches, where genetic predisposition and individual risk factors are taken into account to tailor treatment plans [27].

## **1.2 Electrocardiogram (ECG) Signals for Diagnosis and Monitoring**

The electrocardiogram (ECG) is a fundamental and widely used diagnostic tool in the field of cardiology which records the electrical activity of the heart over time. The ECG signal provides crucial information about the heart rhythm, its rate, and the pathways through which electrical impulses travel across the heart muscle. This electrical activity is captured as a wave pattern comprising important parameters, such as the duration of the P wave, the duration of the QRS complex, the amplitude of the P wave, the T wave, and the RR inter-beat interval. Each parameter corresponds to specific events in the cardiac cycle. For example, the P wave indicates atrial depolarisation, the QRS complex represents ventricular depolarisation, the T wave signifies ventricular repolarisation, and the RR inter-beat interval measures the time between consecutive R-wave peaks, an aspect important for assessing heart rate variability (HRV) [28, 29]. The process of recording ECG signals involves placing electrodes at specific positions on the body, typically across the chest and limbs, to measure the electrical signals generated by cardiac cells as they undergo polarisation and depolarisation [30]. These signals, despite being small, can be accurately detected and amplified for analysis. The interpretation of an ECG involves analysing the waveforms and intervals between cardiac events. Any deviation from normal patterns can indicate conditions such as arrhythmias, ischemic heart disease, myocardial infarction, and others [31, 32]. The ability of an ECG to provide real-time feedback on cardiac function has made it an essential tool in both clinical and ambulatory settings [33]. With advancements in technology, the analysis methods for ECG signals have evolved, too. For example, sophisticated automated systems incorporate machine learning and artificial intelligence (AI) methods to enhance the precision and robustness of cardiac diagnoses [34, 35]. Additionally, ECGs are also pivotal in monitoring disease progression as changes in electrical activity can reflect underlying pathological shifts in heart function [36].

The role of the ECG in detecting and monitoring cardiac diseases is crucial. It is one of the most accessible and non-invasive diagnostic techniques used globally to identify and assess a wide array of cardiovascular conditions. For instance, the early detection of arrhythmias, such as atrial fibrillation, through ECG monitoring has been shown to significantly reduce the risk of stroke and other serious complications [37, 38]. Furthermore, in cases of other cardiac illnesses, such as atrial fibrillation, prompt ECG analysis can guide clinicians in making critical treatment decisions for timely medical interventions [39]. ECG analysis also plays a crucial role in long-term monitoring of patients with chronic heart conditions. Ambulatory ECG monitoring, such as Holter monitoring, enables continuous observation of cardiac activity over 24 to 48 hours, allowing for the capture of intermittent or subtle events that might be missed during standard ECG recordings [40]. These days, advanced wearable technologies, including smartwatches and other portable devices, are not only capable

of recording ECG signals instantly but also offer individuals a convenient way to monitor their heart health regularly [41]. As advancements in cardiovascular disease detection and monitoring continue to evolve over time, there remains significant room for further improvements in terms of accuracy, robustness, efficiency, and other critical factors. Consequently, research in this field is continuously progressing. It is equally important to emphasise that to make advancements in cardiovascular health, it is essential to understand the complex dynamics of the human cardiovascular system, which works in harmony with other body systems in a complex and interconnected manner. The following section delves into a detailed overview of the cardiovascular system as a complex system, supported by extensive literature and discussion.

### **1.3 Complexity in the Self-Organisation of the Human Cardiovascular System**

Understanding the complexities of cardiovascular health and disease requires an understanding of the human body as a complex system. The concept of the human body as a complex system dates back to early physiological studies that recognised the body as a network of interrelated processes, each contributing to overall function. Researchers like Claude Bernard emphasised the significance of the “milieu intérieur,” or interior environment, as a self-regulating system that preserves stability despite external changes [42]. The human body is characterised by complex interactions among various subsystems, including the neurological, endocrine, and immunological systems. These subsystems interact through feedback loops, which are critical for maintaining equilibrium and helping the organism to adapt to varying internal and external stimuli [43]. This self-organising tendency, in which global patterns arise from modest interactions, is a hallmark of complex systems [44]. The cardiovascular system demonstrates the intricacy of the human body. It is more than just a collection of organs and blood vessels; it is a dynamic network that self-organises to satisfy the body’s metabolic demands. The heart, blood arteries, and blood all work together to maintain blood pressure, transmit oxygen and nutrients, and eliminate waste. The system’s complexity stems from the non-linear interactions between various components, where small changes in one section of the system might have major impacts elsewhere [45]. The ability of the cardiovascular system to self-organise was demonstrated by early research. For example, Guyton’s studies on circulatory dynamics throughout the 1960s demonstrated how a complex interaction between the autonomic nervous system, kidney function, and vascular resistance maintains blood pressure and cardiac output [46]. As a result of this interaction, a feedback loop is created that continuously modifies cardiovascular function to maintain efficiency and stability. Furthermore, it is challenging to comprehend the cardiovascular system’s emergent characteristics, like the capacity to control blood flow and synchronise heartbeats, by examining its different parts separately [47]. The system’s complexity is further highlighted by its capacity to adjust to physical stressors like exercise and posture modifications. Mechanisms such as the baroreceptor reflex and local autoregulation of blood flow help the cardiovascular system dynamically reorganise during these activities to sustain blood flow and

oxygen delivery to important organs [48]. As mentioned previously, an in-depth understanding of the connectivity and interplay between the various organs in the human body is crucial for comprehending the functioning of the cardiovascular system. Thus, the following section delves into the literature and relevant discussion surrounding the three major systems in detail.

#### **1.4 Interconnectedness of the Regulatory, the Executive, and the Supply system in the Human Body**

Fig. 1 depicts a schematic diagram of the interconnectivity of the Regulatory system, the Executive system, and the Supply system of the human body. The three systems must work in unison to keep the body functioning normally [49]. Each of the systems is responsible for performing a certain task. For example, the Regulatory system is accountable for regulating a variety of processes; the Executive system is responsible for controlling the activity of working muscles in the body; and the Supply system is in charge of controlling blood circulation within the body [49]. Each of these systems is interconnected and interlinked in a complex fashion, resulting in a multi-layered control system [50, 51]. The schematic in Fig. 1 is inspired by [52] and is adopted in [49, 53] to study the complex processes occurring during circulatory regulation. In the human body, among many control systems, cardiac regulation is responsible for the cardiac and circulatory functions [51]. The complex processes taking place during circulatory regulation can be seen through the lens of (1) long-term circulatory regulation, (2) intermediate-term circulatory regulation, and (3) short-term or rapid circulatory regulation. Whether at rest or in motion, examining the response of the circulatory system is crucial, and it can provide important information about the functioning of the heart. For example, during the physical exercise, subtle changes occur in the circulatory system as part of short-term regulation. The data collected during this short-term regulation provides valuable insights for diagnostic purposes [51].



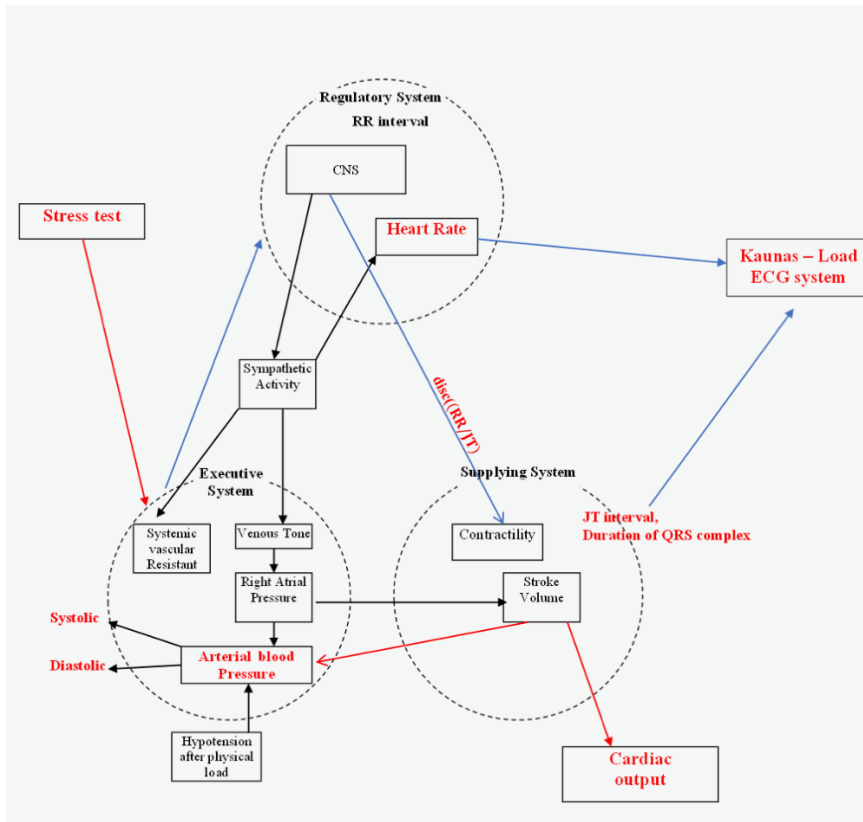


**Fig. 1.** Schematic Diagram Illustrating the Interconnections between the Regulatory, Executive, and Supply Systems [53]

As the exercise is commenced, an immediate increase in the heart rate (HR) occurs. This rapid response is primarily attributed to the autonomic nervous system, which is responsible for involuntary bodily functions, including heart rate regulation [54]. The rate at which the heart beats is directly related to the intensity, or, in other words, the type of the exercise performed [55]. The immediate increase in the heart rate at the onset of the exercise is driven by the rapid activation of the sympathetic nervous system and the reduction in vagal influence. As the intensity of the exercise increases, the heart rate continues to rise proportionally. At high intensity, the sympathetic nervous system takes a leading role in driving the increased heart rate. This intricate coordination ensures that the cardiovascular system efficiently meets the metabolic demands of the body during physical exercise [55, 56]. Regulating arterial blood pressure (ABP) is also one of the vital tasks of the cardiovascular system during the exercise [51, 57]. The intensity of the exercise leads to muscle engagement, which in turn increases ABP. Rising minute volume and heart rate reduce the vagal influence, thereby triggering sympathetic activation and causing ABP elevation. While small muscle groups do not experience sympathetic-induced vasoconstriction, in exercises involving large muscle groups, sympathetic activation is crucial for

regulating blood flow, especially in upper limb muscles, ensuring ABP [57-59]. Systolic and diastolic blood pressure reciprocate during the exercise and are functional indicators used diagnostically in clinics. As the exercise increases, the systolic arterial blood pressure reciprocates and stabilises within 2–3 minutes of the exercise. At the same time, the diastolic arterial blood pressure either remains constant or decreases slightly. The measure of an increase and decrease in the arterial blood pressure thus provides valuable information about a person's cardiovascular performance during the exercise [60, 61]. According to the European and American standard experimental protocols for blood pressure measurement, for a normal person engaged in intense exercise, the increase in systolic pressure is about 250 mmHg, and the corresponding diastolic blood pressure is 110 mmHg [62, 63]. An excessive increase in blood pressure during the exercise leads to the identification of certain conditions, such as hypertension or mortality due to cardiovascular dysfunction [64]. Individuals having high blood pressure or hypertensive individuals usually tend to exhibit higher systolic as well as diastolic arterial blood pressure, which causes an increase in peripheral resistance compared to individuals with normal blood pressure regulation. Several variables impact peripheral resistance, including blood viscosity, vessel diameter, and length [65]. These complex processes characterise the human cardiovascular system as an organ with significant non-linearities in its behaviour, which are further explored in the subsequent section.

### **1.5 Non-linear Nature of the Cardiovascular System**

The RR inter-beat interval of a healthy human exhibits a time series which is characterised by multifractal properties [66], thus placing these time series within a unique category of complex signals. These properties contribute to the inherent variability observed in an individual's heartbeats from one moment to the following [8]. Consequently, ECG analysis has long been a focal point of research, with both conventional and increasingly sophisticated algorithms being developed to address the intricacies of the ECG signal for purposes such as diagnostics. However, no single algorithm is universally optimal, as each method is tailored to specific analytical goals. Therefore, it is considered best practice to corroborate findings using multiple techniques on the same ECG signal. For example, time-domain analyses provide insight into overall heart rate variability (HRV), which reflects autonomic control over the heart, while frequency-domain analyses can offer more specific information about the balance between sympathetic and parasympathetic nervous activity [4]. These traditional methods have laid the groundwork for understanding cardiovascular dynamics but often fall short of fully capturing the complexity of physiological signals. To address this, non-linear analyses, such as fractal and multifractal analysis, have emerged as powerful tools. These techniques reveal the underlying chaotic nature of heart rate fluctuations, demonstrating that the heart's rhythm exhibits patterns that vary over multiple time scales [67, 68].

Multifractal detrended fluctuation analysis (MFDFA), for instance, has become a widely used method for examining these properties in ECG data. By assessing how fluctuations scale with time, MFDFA enables researchers to quantify the degree of

multifractality present in heartbeat intervals. This provides a more nuanced understanding of cardiovascular health, as alterations in multifractal patterns have been linked to various pathological conditions, including atrial fibrillation, heart failure, and increased mortality risk [69]. Furthermore, techniques like recurrence quantification analysis (RQA) and entropy-based measures are frequently employed to assess the complexity of heart dynamics [70]. These non-linear methods can detect subtle changes in heart rhythm that may be early indicators of cardiovascular dysfunction, offering a valuable tool for both diagnosis and prognosis [71]. The clinical implications of understanding the non-linear nature of the cardiovascular system are profound. For example, by applying these advanced signal processing techniques, clinicians can better assess the risk of adverse cardiac events, personalise treatment plans, and monitor disease progression in patients with known cardiovascular conditions. Additionally, insights from non-linear analyses have practical applications in developing wearable technologies for continuous heart monitoring, which are becoming increasingly relevant in both preventive and emergency medical care [72]. The human cardiovascular system exemplifies the complexity of the body's self-organising mechanisms. Its non-linear, dynamic nature necessitates a comprehensive approach to research and diagnosis, combining traditional and modern analytical techniques. As our understanding of these multifaceted processes deepens, the potential for innovative diagnostic tools and therapies will continue to expand, ultimately improving patient outcomes and advancing the field of cardiovascular medicine [67].

### **1.6 Perfect Matrices of Lagrange Differences as a Robust Algorithm for ECG Analysis**

The concept of perfect matrices of Lagrange differences (PMLD) was initially introduced by Ziaukas et al. [13] as a viable matrix-based algorithm for analysing complex time series, such as ECG signals. Building on this foundation, Šiaučiūnaitė et al. applied the PMLD algorithm to visualise intricate cardiovascular processes during electrical auricular vagus nerve stimulation, specifically analysing JT/QRS and RR/JT cardiac intervals [53]. This algorithm was further utilised to detect ischemic episodes through the analysis of JT/ST intervals [73] and to characterise transitions through the anaerobic threshold by examining the RR/QRS interval [74]. These studies are meticulously designed to showcase the PMLD matrix-based approach as an effective and reliable algorithm for analysing various cardiovascular processes during both different physical activities and periods of rest. It is well stated in [13] that, in a scalar time series, derivatives can be calculated using Lagrange differences at key points in the data. While it is known that deriving such values can often amplify the noise present in the series, these derivatives can also be used strategically to highlight minor variations in dynamic processes that are not otherwise apparent [13, 75]. With this understanding, it is important to utilise scalar values from time series, such as  $x$  and  $y$ , and their cross differences. The aim is to develop a single scalar attribute that encapsulates the dynamic interaction between scalar time series  $x$  and  $y$ .

By employing square second-order matrices populated with various values and their differences, it is possible to compute a unique parameter that captures a specific characteristic of these matrices. The local matrix architecture of the Lagrange differences is well explained by Ziaukas et al. [13]. For a matrix to be a perfect matrix of Lagrange differences, the assembly of elements should adhere to the following six criteria:

1. Each element within the matrix is distinct.
2. The principal diagonal contains the zero-order differences.
3. The secondary diagonal is composed of first-order differences.
4. The indices of  $x$  and  $y$  can assume one of three possible values to generate the current, forward, and backward time moments within the matrix structure:  $(n - \delta, n, n + \delta)$ , where  $n$  denotes the current moment and parameter  $\delta$  is used to represent the time lag ( $\delta \in \mathbb{N}$ ).
5. The perfect matrix of Lagrange differences must ensure lexicographical balance, meaning that each expression within the matrix contains an equal number of  $x$  and  $y$  elements.
6. Temporal balance must also be achieved in the perfect matrix of Lagrange differences, with each element's expression having an equal number of indices with subscripts  $-\delta$  and  $+\delta$ .

Only eighteen distinct matrices adhere to these criteria [13]. The following are examples of non-perfect matrices that do not comply with these criteria:

- $$\begin{pmatrix} y_n & x_{n+\delta} - y_{n+\delta} \\ x_{n-\delta} - y_{n-\delta} & y_n \end{pmatrix}$$

A perfect matrix cannot be constituted if there is no lexicographical balance (i.e. the number of  $y$ 's is greater than the number of  $x$ 's).

- $$\begin{pmatrix} x_n & x_{n+\delta} - y_{n+\delta} \\ x_{n+\delta} - y_{n+\delta} & y_n \end{pmatrix}$$

A perfect matrix cannot be constituted if there is no temporal balance of elements (i.e. the number of pluses  $\delta$  is greater than the number of minuses  $\delta$ ).

- $$\begin{pmatrix} y_n & x_{n+\delta} - y_{n+\delta} \\ x_{n-\delta} - y_{n-\delta} & 0 \end{pmatrix}$$

A perfect matrix cannot be constituted if there is a null element present.

However, a perfect matrix can be constituted if the six elements of the matrix are mapped perfectly into the matrix trajectory by adhering to the rules established for the scalar series  $x$  and  $y$ , as follows:

$$L_{\delta,k}^{(s)} = \begin{pmatrix} x_n & x_{n+\delta} - y_{n+\delta} \\ x_{n-\delta} - y_{n-\delta} & y_n \end{pmatrix}; \quad (1)$$

where  $n$  is the current moment in time,  $\delta$  is the time lag, and  $s$  is the number of the perfect matrix of Lagrange differences ( $s$  ranges from 1 to 18).

### Optimisation of Parameters in ECG Signal Analysis Using Lagrange Differences

In the study referenced as [13], the RR inter-beat interval and the duration of the JT wave are analysed for ten individuals using the perfect matrix of Lagrange differences. The ECG recordings were obtained during a bicycle ergometry exercise,

which involves continuous pedalling with an incrementally increasing load and is terminated when the participant can no longer continue. The study found that the RR inter-beat interval varied throughout the exercise for each individual, with differences in how each participant responded to the maximum load.

To determine the structural coefficient representing the interaction between RR and JT cardiac intervals, denoted as  $str$ , the ratio of the maximum to the minimum absolute eigenvalue  $\left(\frac{|\max \lambda_k|}{|\min \lambda_k|}\right)$  of the perfect Lagrange differences matrix was used in [13]. The highest and lowest absolute eigenvalues ( $\max \lambda_k$  and  $\min \lambda_k$ ), along with the discriminant ( $disc = (a_{11}a_{22})^2 + 4a_{21}a_{12}$ ), were selected for the analysis. A time delay of one second was applied to the measurements [13].

The scaled inverse values of the load are represented as  $l_k$  for  $k = 1, 2, \dots, 1199$ . Correspondingly, the specific parameters calculated for the perfect matrix of Lagrange differences, derived from the RR inter-beat interval (x-time series) and JT wave (y-time series), are denoted as  $p_k$  for  $k = 1, 2, \dots, 1199$ . The objective of the optimisation problem is to identify the most appropriate parameter that minimises the root mean square error (RMSE) between  $l_k$  and  $p_k$ . Before initiating the optimisation process, the values of  $p_k$  are normalised within the range  $[0, 1]$ . ECG records from ten individuals are used to tune the optimal parameters computationally. The value of  $N$  varies for each individual because the stopping moment of the bicycle ergometry exercise differs from person to person. Instead of selecting a single perfect Lagrange difference matrix, the root mean square error (RMSE) is averaged across all 18 perfect matrices. In this analysis, the parameter  $\delta = 1$  is fixed [13]:

$$\arg \min \left( \sqrt{\frac{1}{N} \sum_{k=1}^N (l_k - p_k)^2} \right). \quad (2)$$

Using the formula in (2), it was analysed that the minimum absolute eigenvalue ( $\min |\lambda_k|$ ) produces the best value for only one individual. Therefore, the authors of [13] chose the maximum absolute eigenvalue ( $\max |\lambda_k|$ ) as the most suitable parameter for capturing the local relationships described by the perfect Lagrange matrices. Thus, the computational experiments are conducted using  $\max |\lambda(L_{\delta,k}(s))|$ , where  $L_{\delta,k}(s)$  represents the perfect matrix of Lagrange differences centred around the time moment  $k$ . This criterion was consistently applied for computational purposes throughout the study, wherever the perfect Lagrange difference matrices were utilised for ECG analysis [13].

### Smoothing Techniques for Scalar Time Series in ECG analysis

As noted earlier, it was highlighted that the RR inter-beat interval and JT wave exhibit ongoing changes throughout the exercise due to individual variations in response to the external load. This dynamic behaviour is also evident in the time series ( $x$ ) and ( $y$ ) derived from these measurements. To manage these fluctuations effectively, the moving average technique is considered one of the most straightforward approaches [76, 77]. A combination of moving average with internal and external smoothing is also an effective approach for removing noise and artefacts from the ECG signal. In the case of ECG signal analysis using perfect matrices of

Lagrange differences, the radius of internal smoothing, denoted as  $\Delta$ , specifies the number of parameter values considered for averaging when computing perfect matrix of Lagrange differences across different settings of delta ( $\delta$ ). For instance, the method of averaging within the dataset itself, without incorporating external data, is described by the following approach [13]:

$$\frac{1}{\Delta} \sum_{\delta=1}^{\Delta} \max |\lambda \left( L_{\delta,k}^{(s)} \right)|. \quad (3)$$

Following equation (3), the parameter values at different time moments  $k$  are subjected to external smoothing via the moving average method. External smoothing utilises only odd-numbered window widths ( $m$ ), ensuring the averaging process is centred symmetrically around each time point  $k$ . The reconstructed parameter value is denoted as  $p_k(s, \Delta, m)$ , where  $k$  refers to the time moment,  $\Delta$  represents the internal smoothing radius, and  $m$  is the external smoothing width. The relevant equation for this method is [13]:

$$p_k(s, \Delta, m) = \frac{1}{2m+1} \sum_{j=k-m}^{k+m} \sum_{\delta=1}^{\Delta} \max |\lambda \left( L_{\delta,k}^{(s)} \right)|. \quad (4)$$

In the case where internal smoothing is not applied, the process of external smoothing is described by the following equation:

$$p_k(s, 1, m) = \frac{1}{2m+1} \sum_{j=k-m}^{k+m} \max |\lambda \left( L_{\delta,k}^{(s)} \right)|. \quad (5)$$

To examine the effects of internal and external smoothing, the authors in [13] used a synthetic dataset defined as  $x = (x_1, \dots, x_7) = (1, 3, 2, 0, 4, 3, 1)$  and  $y = (y_1, \dots, y_7) = (2, 1, 0, 4, 3, 1, 1)$ . Calculating  $p_k(1, 2, 1)$ , it becomes evident that moderate levels of internal and external smoothing, specifically with  $m = \Delta = 3$ , effectively reduce the root mean square error (RMSE) for nearly all perfect matrices of Lagrange differences. Consequently,  $m = \Delta = 3$  has been chosen as the standard setting for the computations in [13]. While the PMLD has been applied in ECG analysis, significant opportunities for enhancement and further exploration remain. Notably, the cited studies have largely focused on basic matrix structures, primarily utilising second-order matrices to analyse two ECG parameters. Key questions, such as extending the local matrix architecture of PMLD to higher-order matrices, assessing the impact of degrees of freedom within the matrix elements on analytical outcomes, and comparing the PMLD approach with other matrix designs, have yet to be thoroughly addressed.

In this work, the author builds upon the foundational concept of PMLD, addressing these demanding questions in ECG analysis. In addition, the author will also focus on various ECG parameters, including the QRS complex duration, P wave duration, P wave amplitude, duration of the JT wave, and the RR inter-beat interval. Furthermore, the PMLD will be employed to study the self-organisation of the cardiovascular system and to diagnose episodes of atrial fibrillation. The author of the study will also evaluate the effectiveness of PMLD by comparing it against other matrix architectures introduced by Navickas et al. [75].

## 1.7 Hankel Matrix-Based Algorithm for Complex Signal Analysis

The majority of time series encountered in real-world applications exhibit chaotic and non-linear behaviour and are contaminated by noise. Therefore, forecasting such time series data poses significant difficulties across numerous domains. Complex, chaotic systems are often utilised to address theoretical and practical issues in fields such as signal processing, socioeconomics, and bioinformatics [78]. Both long-term and short-term time series prediction approaches exhibit fundamental distinctions in their methodologies. Long-term prediction methods typically involve constructing a comprehensive model of the underlying process, which is subsequently used to forecast future behaviour over extended time horizons. This approach requires a thorough understanding of the dynamics governing the system and often leverages complex models to capture long-term trends and patterns. On the other hand, short-term prediction approaches mainly focus on providing forecasts for the near future by modelling the process within a shorter time frame. These methods are designed to generate immediate predictions and are generally more responsive to recent data. However, a notable challenge in short-term prediction is the limited availability of data, which hampers the development of robust models capable of making accurate forecasts over short durations. This data scarcity can impede the ability to capture transient fluctuations and nuanced behaviours in the system. When it comes to forecasting real-world time series data, it is well understood that no one-size-fits-all solution exists. Therefore, the field of short-term time series forecasting is still evolving. Among the notable examples are [79], [80], [81], and [82]. With the push for more sophisticated time series forecasting methods, a range of novel techniques has emerged. For example, researchers have developed the Hybrid Monte Carlo algorithm [83] and wavelet-based decomposition methods [84]. Other innovations include combining various forecasting models into a single approach [85] and reconstructing the inherent algebraic structures that govern the evolution of the time series to improve accuracy [80]. In the study cited as [78], it has been stated that in order to effectively model the non-linear aspects of real-world data, advanced methods beyond conventional statistical techniques are necessary. Additionally, [84] points out that proper data preprocessing is essential for implementing certain forecasting approaches successfully.

Enhancing the performance of short-term time series predictors can be achieved by breaking down the original series into a set of simpler components, each of which can be forecasted separately. [84] emphasised the need for preprocessing irregular data by applying a weighted moving average to identify key weight variables that optimise the decomposition process. This approach often involves using a linear homogeneous recurrence relation of order  $p$  with constant coefficients to refine the predictions:

$$y_m = \beta_{p-1}y_{m-1} + \beta_{p-2}y_{m-2} + \cdots + \beta_0y_{m-p}; \quad (6)$$

where  $\beta_k$  for  $k = 0, 1, 2, \dots, p-1$  are constants. This defines a linear recurrence sequence (LRS), where the sequence's evolution is governed by its initial values  $y_l$ , for  $l = 0, 1, \dots, p-1$ . The corresponding characteristic polynomial is:

$$Q(\lambda) = \lambda^p - \beta_{p-1}\lambda^{p-1} - \beta_{p-2}\lambda^{p-2} - \dots - \beta_0; \quad (7)$$

where the roots  $\lambda_1, \lambda_2, \dots, \lambda_p$  describe the sequence that satisfies the recurrence. If all roots  $\lambda_1, \lambda_2, \dots, \lambda_p$  are distinct, the general solution to the recurrence relation is:

$$y_m = \lambda_1 \gamma_1^m + \lambda_2 \gamma_2^m + \dots + \lambda_p \gamma_p^m; \quad (8)$$

where the coefficients  $\gamma_1, \gamma_2, \dots, \gamma_p$  are chosen to match the initial conditions of the sequence. It is important to note that if the LRS is real, then all roots are either real or appear in complex conjugate pairs.

When the roots of the characteristic polynomial are multiple, the recurrence relation can be expressed as:

$$y_m = \sum_{i=1}^r \sum_{j=0}^{n_i-1} \delta_{ij} (\lambda_i^j) \lambda_i^m; \quad (9)$$

where  $r$  is the number of distinct roots,  $n_i$  is the multiplicity index for the  $i$ -th root, and  $n_1 + n_2 + \dots + n_r = p$ .

The procedure for reconstructing the LRS model from a sequence  $\{y_m\}_{m=0}^{\infty}$  becomes more intricate if the order of the LRS is not known in advance. This often involves applying the Hankel transform to the sequence  $\{y_m\}_{m=0}^{\infty}$ , which results in the sequence  $\{h_m\}_{m=0}^{\infty}$ , where  $h_m = \det(H_m)$  and  $H_m$  is the Hankel matrix:

$$\begin{bmatrix} h_0 & h_1 & \dots & h_{p-1} \\ h_1 & h_2 & \dots & h_p \\ \vdots & \vdots & \ddots & \vdots \\ h_{p-1} & h_p & \dots & h_{2p-2} \end{bmatrix}.$$

The dimensions of the Hankel matrix are defined as  $((p+1) \times (p+1))$ . If there exists such  $p \geq 1$  that  $h_{p+1} \neq 0$  but  $h_m = 0$  for all  $m \geq p$ , then  $\{y_m\}_{m=0}^{\infty}$  is an LRS whose order is  $p-1$ , and the corresponding characteristic polynomial reads as follows:

$$\det \begin{bmatrix} h_0 & h_1 & \dots & h_{p-1} \\ h_1 & h_2 & \dots & h_p \\ \vdots & \vdots & \ddots & \vdots \\ h_{p-1} & h_p & \dots & h_{2p-2} \\ 1 & \rho & \dots & \rho^p \end{bmatrix} = 0. \quad (10)$$

The variable  $p$  is introduced as part of the characteristic polynomial when the LRS has multiple roots. Specifically,  $p$  corresponds to a coefficient related to the multiplicity of the roots of the characteristic polynomial. There can only be considered the case, as stated earlier, when the roots of (10) are all distinct (because a real-world time series is always contaminated by noise).  $H = USV^T$  is the result of a singular value decomposition (SVD) of a real matrix  $H$ , where  $U$  comprises orthonormal eigenvectors of  $H^T H$  and  $S$  is a diagonal matrix whose elements are the sorted square roots of the eigenvalues  $H^T H$ . SVD is then applied to this Hankel matrix in order to decompose the matrix into its three constituent matrices. The singular values on the



diagonal of the Hankel matrix indicate the significance of different components within the time series data. By identifying the singular values greater than a specified threshold  $\epsilon$ , the rank or complexity of the data at different points in time can be determined [86].

**Example 1.** Let us consider a period-3 sequence  $\{1, 2.1, 3.3, 1, 2.1, 3.3 \dots\}$ . The Hankel transform yields the sequence:

$$h_1 = x_1 = 1;$$

$$h_2 = \begin{vmatrix} 1 & 2.1 \\ 2.1 & 3 \end{vmatrix} = -1.41;$$

$$h_3 = \begin{vmatrix} 1 & 2.1 & 3.3 \\ 2.1 & 3.3 & 1 \\ 3.3 & 1 & 2.1 \end{vmatrix} = -25.408; \text{ and}$$

$$h_4 = \begin{vmatrix} 1 & 2.1 & 3.3 & 1 \\ 2.1 & 3.3 & 1 & 2.1 \\ 3.3 & 1 & 2.1 & 3.3 \\ 1 & 2.1 & 3.3 & 1 \end{vmatrix} = 0.$$

Clearly, all higher-order determinants  $h_k = 0$ ,  $k = 4, 5, \dots$ , because at least two rows of the Hankel determinants are equal. Note that periodic sequences comprise only a small part of all possible LRS, and the order of the linear recurrence defines the memory horizon of the mathematical model governing the evolution of the time series.

The determination of the LRS order by computing Hankel determinants is not a feasible approach due to two major reasons. First of all, the evaluation of a sequence of determinants of very large matrices becomes a rather difficult and numerically expensive problem [86]. Secondly, all real-world time series are contaminated by inevitable noise, which prevents the identification of the LRS order.

Let us consider that  $\{x_j\}_{j=1}^{+\infty}$  is an LRS, and its order is  $r_x$ ;  $\{y_j\}_{j=1}^{+\infty}$  is an LRS, and its order is  $r_y$ . Then the order of  $\{\alpha x_j + \beta y_j\}_{j=1}^{+\infty}$  ( $\alpha, \beta \in \mathbb{R}$ ) is  $\max(r_x; r_y)$  [86]. This property yields the following consequence. The LRS order of any real-world time series is infinite simply due to the presence of noise. To illustrate this, let us consider a discrete realisation of random numbers  $\{\delta_j\}_{j=1}^{+\infty}$  (it does not matter whether the distribution is Gaussian or not). The LRS order of time series  $\{\delta_j\}_{j=1}^{+\infty}$  is infinite (it is not an LRS). Otherwise, it would be possible to reconstruct a mathematical model of noise, which would contradict the definition of noise. However, then, the order of  $\{\alpha x_j + \beta \delta_j\}_{j=1}^{+\infty}$  is infinite, even if  $\beta$  is small. In other words, the order of an LRS contaminated even by a small additive noise is infinite.

Clearly, it is necessary to develop mathematical algorithms capable of identifying the mathematical model of a time series before this series is contaminated by noise. Instead of forming the sequence of Hankel matrices, one needs to define the maximal detectable order of an LRS. Let us assume that this maximal order is  $d$ . Then, the H-rank of a sequence (even if this sequence is not an LRS) is defined as the number

of squared singular values of the Hankel matrix  $H_d$  larger than  $\varepsilon$  [86]. Squared singular values of  $H_d$  are computed using standard SVD routines. It is shown in [86] that the number of non-zero squared singular values of  $H_d$  is equal to the order of the LRS (if the original time series is indeed an LRS).

A proper selection of  $d$  and  $\varepsilon$  can help utilise the H-rank algorithm as an efficient tool for assessing the complexity of real-world time series [80, 87]. Let us consider a time series  $\{x_j\}_{j=1}^{+\infty}$  contaminated by noise  $\{\delta_j\}_{j=1}^{+\infty}$ :

$$\{\tilde{x}_j\}_{j=1}^{+\infty} = \{x_j + \delta_j\}_{j=1}^{+\infty}. \quad (11)$$

Then, the  $d$ -dimensional Hankel matrix reads as follows:

$$H_d = \begin{bmatrix} x_1 + \delta_1 & x_2 + \delta_2 & \cdots & x_d + \delta_d \\ x_2 + \delta_2 & x_3 + \delta_3 & \cdots & x_{d+1} + \delta_{d+1} \\ \vdots & \vdots & \ddots & \vdots \\ x_d + \delta_d & x_{d+1} + \delta_{d+1} & \cdots & x_{2d-1} + \delta_{2d-1} \end{bmatrix}. \quad (12)$$

Note that  $H_d$  remains a symmetric matrix after the original time series is perturbed by noise. Subtle differences between the spectrum of the perturbed matrix and the H-ranks of the perturbed time series are discussed in detail in [80].

**Example 2.** Let us consider the same period-3 sequence used in Example 1. Let us set  $d = 5$ . Then,  $H_5$  reads as follows:

$$H_5 = \begin{bmatrix} 1 & 2.1 & 3.3 & 1 & 2.1 \\ 2.1 & 3.3 & 1 & 2.1 & 3.3 \\ 3.3 & 1 & 2.1 & 3.3 & 1 \\ 1 & 2.1 & 3.3 & 1 & 2.1 \\ 2.1 & 3.3 & 1 & 2.1 & 3.3 \end{bmatrix}. \quad (13)$$

Singular values of the period-3 sequence read as follows:

$$\{\sigma_j^2\}_{j=1}^5 = \{10.7669, 3.1060, 3.0391, 0.0000, 0.0000\}. \quad (14)$$

Three non-zero singular values indicate that the order of the original LRS is equal to three.

**Example 3.** Let us consider the same period-3 sequence used in Example 1. Let us perturb this sequence by normally distributed random noise with zero mean and standard deviation equal to 0.1:

$$\{\delta_j\}_{j=1}^{+\infty} = \left\{ \begin{array}{l} -0.0649, 0.1181, -0.0758, -0.1110, -0.0846, -0.0573, \\ -0.0559, \dots \end{array} \right\}. \quad (15)$$

Let us set  $d = 5$ . Then,  $H_5$  reads as follows:

$$H_5 = \begin{bmatrix} 0.9351 & 2.2181 & 3.2242 & 0.8890 & 2.0154 \\ 2.2181 & 3.2242 & 0.8890 & 2.0154 & 3.2427 \\ 3.2242 & 0.8890 & 2.0154 & 3.2427 & 0.9441 \\ 0.8890 & 2.0154 & 3.2427 & 0.9441 & 2.1178 \\ 2.0154 & 3.2427 & 0.9441 & 2.1178 & 3.2803 \end{bmatrix}. \quad (16)$$

Singular values of the perturbed period-3 sequence read as follows:

$$\{\sigma_j^2\}_{j=1}^5 = \{10.5170, 3.1849, 3.0062, 0.1841, 0.1233\}. \quad (17)$$

Let us choose some discrete values of  $\varepsilon$  and then count the number of singular values greater than  $\varepsilon$  (see Table 1). By doing that, we can reconstruct the H-rank of the perturbed sequence.

**Table 1.** Reconstruction of H-rank for the perturbed sequence across varying  $\varepsilon$  values

$\varepsilon$	$(\sigma_1)^2$	$(\sigma_2)^2$	$(\sigma_3)^2$	$(\sigma_4)^2$	$(\sigma_5)^2$	H-rank
0	10.5170	3.1849	3.0062	0.1841	0.1233	5
0.1	10.5170	3.1849	3.0062	0.1841	0.1233	5
1	10.5170	3.1849	3.0062	0.1841	0.1233	3
5	10.5170	3.1849	3.0062	0.1841	0.1233	1
15	10.5170	3.1849	3.0062	0.1841	0.1233	0

Table 1 shows that the parameter  $\varepsilon$  plays an important role in determining the H-rank of a sequence. If  $\varepsilon$  is too low, all squared singular values will be greater than  $\varepsilon$ . If  $\varepsilon$  is too large, all squared singular values will be lower than  $\varepsilon$ , as seen in Table 1. It can be observed that the order of the period-3 sequence contaminated by noise is reconstructed correctly at  $\varepsilon = 1$  (Table 1). It is important to note that reconstructed squared singular values converge to the squared singular values of the non-perturbed time series when the variance of the noise tends to zero [80]. Therefore, the values of  $\varepsilon$  capable of reconstructing the correct value of the H-rank of the perturbed sequence (Table 1) would be smaller if the variance of the additive noise were smaller as well.

The parameter  $\varepsilon$  determines the sensitivity of the H-rank algorithm. For experimental data, there is no a priori knowledge neither about the mathematical model governing the evolution of the underlying time series, nor the intensity or the type of the additive noise. However, as shown in [80, 87], H-ranks can be effectively and efficiently used to approximate the algebraic complexity of real-world time series. The rule of thumb is to set such a value of  $\varepsilon$  that the reconstructed H-rank is equal (on average) to half of  $d$ . In other words, the sensitivity of the H-rank algorithm should be tuned in such a way that the output is around the middle range of the measurement scale (between 0 and  $d$ ).

Existing Hankel matrix-based methodologies have been extensively applied in various aspects of ECG signal analysis, including time series prediction [86], feature extraction of the ECG [88], complexity evaluation of ECG parameters [89], as well as generating H-ranks of the heart's electrical and hemodynamic processes [90].

Despite significant advancements in applying Hankel matrices to ECG analysis, substantial untapped potential remains for exploring the applicability of Hankel matrix-based algorithms to complex dynamical processes within the cardiovascular system. For example, HRV shows the body's ability to adjust to changing physiological conditions, which frequently shifts throughout moments of quiet and focused attention. When the mind enters a state of deep relaxation, such as during certain mental clarity and mindfulness techniques, HRV shows significant modulation. These changes are most obvious in situations such as meditation, where the body's autonomic reaction becomes more balanced, making it a compelling area for further investigation. Additionally, examining the cumulative effects of HRV across different subjects could yield valuable insights into the physiological and psychological dynamics of group activities. The author of the study delves into these areas by applying the Hankel matrix-based approach.

### Moving Average Technique

The moving average technique helps to smooth out short-term fluctuations and highlight the trends and patterns in the data by averaging each value in the observation window with its neighbouring values within a specified window size [91]. The moving average algorithm can use equal or different weights. For the simple moving average technique, one can start by averaging the first group of numbers from the series. This process of shifting and averaging is iterated across the entire dataset, as detailed by [92]. A weighted average incorporates multiplicative weighting factors to apply differential importance to data points across a specified window, thereby influencing their contribution to the overall average. The weighted moving average (WMA) is formally defined through the convolution of a data sequence with a fixed weighting function, as encapsulated by the following equation:

$$\{y_j\}_{j=0}^{+\infty} = \{\sum_{s=0}^{L-1} w_{L-s} x_{s+j}\}_{j=0}^{+\infty}; \quad (18)$$

where each element of the new sequence is the mean of  $L$  consecutive values from the original sequence. Considering the sequence  $\{y_m\}_{m=0}^{\infty}$  as an LRS, the application of the WMA over a window of length  $L$  transforms it into another LRS, as detailed in equations (18) and (19):

$$y_j = \sum_{s=0}^{L-1} w_{L-s} x_{s+j} \sum_{k=1}^{r_k} \sum_{l=0}^{n_k-1} u_{kl} (s+j) \rho_{ks+j-1} = \sum_{k=1}^{m_k} \sum_{l=0}^{n_k-1} u_{ktjl} \rho_{kj}. \quad (19)$$

When using specific weight coefficients  $w$ , indices  $k$ , and roots  $\rho_k$ , some values of the parameters  $u_{kt}$  might become zero, leading to a lower order of the LRS than the original sequence. It is important to note that  $u_{kt}$  values are independent of the index  $j$ . In summary, equation (19) extends the weighted moving average concept by introducing a nested recurrence structure that is influenced by specific coefficients, indices, and roots. This structure enables the transformation of the original sequence into a new form with potentially lower order and refined characteristics. The WMA method is instrumental in filtering out essential characteristics in the analysis of complex systems, as indicated by Landauskas et al. [86].

## 1.8 Embedding Techniques for Capturing System Dynamics in the State Space

To analyse non-linear time series and track the system's progression in  $m$ -dimensional space, it is essential to reconstruct the dynamic behaviour of the underlying system. Takens' time-delay embedding theorem [93] is the most commonly used method, which requires estimating two parameters: the embedding dimension  $m$  and the time delay  $\tau$ . The embedding dimension optimises the time series' spread within the  $m$ -dimensional space, preserving the system's dynamics [93]. Takens suggests that the embedding dimension should be greater than twice the actual dimension of the system plus one. In situations where the system's properties are not well understood beforehand, it is often beneficial to use alternative methods for estimating the embedding dimension, such as evaluating the coherence of the embedded data points [94]. Although the uniform embedding technique is widely applied to reconstruct attractors and is effective in many pattern recognition tasks, it faces challenges, particularly when analysing multiple periodicities in non-stationary biological signals.

In non-linear time series analysis, a key objective is to reconstruct the system's dynamics within a state space, often referred to as  $m$ -dimensional space. The goal of this reconstruction is to identify a closed subset within the state space, known as the system attractor, which encompasses all potential state vectors and their dynamics, assuming the system is dissipative. Reconstructing the system's original attractor from the time series data is a challenging task. However, the time-delay embedding theorem provides a method to generate a comparable attractor. The state vectors of a time series are defined using a uniform reconstruction or embedding process  $s = \{x[0], x[1], \dots, x[n]\}$ , where  $n$  represents the length of the series, and they are given by:  $x[\vec{t}] = \{x[t], x[t - \tau], \dots, x[t - (m - 1)\tau]\}$ , where  $m$  is the embedding dimension—the smallest number of coordinates needed to represent the time series in the state space without overlap—and  $\tau$  is the time delay, which determines the shape and distribution of the reconstructed attractor. Since the  $\tau$  parameter is kept constant during the process, this method is termed “uniform embedding”.

The study of Timofejeva et al. [95] on attractor embedding was instrumental in exploring the synchronisation of human heart rhythms with the Earth's magnetic field. In their research, the optimal time delay parameter was used as a geometric characteristic of the embedded attractor. When data series are smoothed using a WMA algorithm, the optimal time delay can be reconstructed for both overlapping and non-overlapping observation windows. The optimal time delay is identified by determining when the reconstructed attractor occupies the largest area in a two-dimensional phase plane [95]. In [53], the author adeptly employs phase maps of bioelectrical signals to examine the dynamic processes triggered by vagus nerve stimulation. By mapping these dynamics in a phase plane, the study not only illustrates but also quantifies the stability of the attractors, thereby shedding light on the complex mechanisms within the explored cardiovascular system. Erem et al. [96] also emphasise that attractor mapping is a well-established and widely acknowledged approach for the analysis of similar dynamic phenomena.

To refine the classification of non-linearities, non-uniform embedding techniques offer a notable advancement over conventional uniform approaches. Unlike methods that use a single scalar time delay  $\tau$  for reconstructing the state space, non-uniform embedding involves testing a time lag vector  $\vec{T} = (\tau_1, \tau_2, \dots, \tau_{m-1})$ . This is reflected in the non-uniform embedding vector  $\{x[t], x[t + \tau_1], x[t + \tau_1 + \tau_2], \dots, x[t + \tau_1 + \dots + \tau_{m-1}]\}$ . While non-uniform embedding can provide a more nuanced representation of system dynamics, it is computationally intensive, limiting its use to smaller datasets and specific tasks, such as time series modelling and prediction. Time series complexity can be defined using metrics like Lempel-Ziv or Kolmogorov complexity, while chaotic behaviour is often quantified by calculating the maximum Lyapunov exponent. Dimensionality estimation techniques are another method for assessing time series complexity. These non-uniform embedding techniques are used by the author of this thesis to visualise the HRV data of the psychological synchronisation between the two groups. Both uniform and non-uniform embedding techniques are instrumental in various time series analyses and have proven to be effective in dealing with complex time series that occur in the real world. Although the embedding methods are effective for attractor reconstruction, permutation entropy (PE) might also yield better outcomes, as it is also considered one of the important methods for calculating the complexity of a time series [97, 98].

### 1.9 Permutation Entropy for Complex Time Series Analysis

Permutation entropy (PE) is a measure used in time series analysis to quantify the complexity or randomness of a system. The PE technique was introduced by Christoph Bandt and Bernd Pompe in 2002 and serves as an efficient and accessible technique for analysing patterns and dynamics within time series [99]. The method is grounded in the comparison of adjacent values, allowing for the creation of complexity measures that can be applied to real-world data. In the work of Bandt and Pompe, they demonstrated that PE exhibits behaviour comparable to Lyapunov exponents when applied to chaotic dynamical systems, with particular effectiveness in the presence of noise, whether dynamical or observational [99]. For non-linear time series, PE was proposed as a complexity measure by Zunino et al. [100]. If there is a time series  $\{z_i\}$  of length  $M$ , it can be reconstructed into the  $n$ -dimensional state space as follows:

$$Z_h^{n,\theta} = \{z_h, z_{h+\theta}, \dots, z_{h+(n-1)\theta}\}, h = 1, 2, \dots, M - (n-1)\theta; \quad (20)$$

where  $n$  is the embedding dimension and  $\theta$  is the time delay. The elements in the vector  $Z_h^{n,\theta}$  are then arranged in ascending order:

$$z_h + (r_1 - 1)\theta \leq z_h + (r_2 - 1)\theta \leq \dots \leq z_h + (r_n - 1)\theta. \quad (21)$$

In situations where equality occurs, such as:

$$z_h + (r_{i_1} - 1)\theta = z_h + (r_{i_2} - 1)\theta; \quad (22)$$

the elements are ordered by their indices  $r$ , where  $r_{l_1} \leq r_{l_2}$  then  $z_h + (r_{l_1} - 1)\theta < z_h + (r_{l_2} - 1)\theta$ , otherwise  $z_h + (r_{l_1} - 1)\theta > z_h + (r_{l_2} - 1)\theta$ . The sequence corresponding to each vector  $Z_h^{n,\theta}$  is:

$$T_h = [r_1, r_2, \dots, r_n], h = 1, 2, \dots, M - (n - 1)\theta. \quad (23)$$

There are  $n!$  possible sequences, and the frequency of each sequence type is calculated by [100]:

$$Q_w^{n,\theta} = \frac{\text{Count}(w)}{M - (n - 1)\theta}, w = 1, 2, \dots, n!; \quad (24)$$

where  $\text{Count}(w)$  is the number of occurrences of each sequence type, and the total number of sequences is  $M - (n - 1)\theta$ . The order- $n$  permutation entropy is defined as:

$$H_{PE}(n) = -\sum_{w=1}^{n!} Q_w^{n,\theta} \ln(Q_w^{n,\theta}), 0 \leq H_{PE}(n) \leq \ln(n!). \quad (25)$$

For convenience,  $H_{PE}(n)$  can be normalised by dividing it by  $\ln(n!)$ , resulting in [100]:

$$h_{PE}(n) = \frac{H_{PE}(n)}{\ln(n!)}. \quad (26)$$

## 1.10 Wavelet Techniques for Complex Time Series Analysis

Wavelet analysis is also a powerful computational tool for uncovering hidden patterns in complex signals, such as ECG data, that are not easily detected by traditional Fourier transform methods due to limitations related to the sampling frequency. Unlike Fourier analysis, which decomposes a signal into a sum of harmonics with fixed frequency resolution [101, 102], wavelet analysis decomposes the signal into scaled and shifted versions of a base function, known as the mother wavelet [103, 104]. This makes wavelet analysis particularly effective in analysing signals with transient features, such as ECG signals, where rapid changes occur over short time intervals. In ECG signal processing, wavelet analysis is used to extract key features such as the QRS complex and P and T waves and to detect arrhythmias or other abnormalities [105]. The ability of wavelets to focus on specific features of the signal at multiple scales makes them ideal for this type of analysis. The initial application of wavelet transforms was proposed in the early 1980s by Morlet [101], and since then, wavelet analysis has become a fundamental tool in the time-frequency analysis of signals, enabling the examination of both the frequency content of the signal and how this content evolves over time. This is particularly important for physiological signals, such as ECG, where different features may appear at varying scales and times [101].

The two main classes of wavelet transforms are the Continuous Wavelet Transform (CWT) and the Discrete Wavelet Transform (DWT). The CWT represents a signal in terms of scaled and shifted versions of the mother wavelet and is mathematically defined by:

$$W_x(a, b) = \frac{1}{\sqrt{|a|}} \int_{-\infty}^{\infty} x(t) \psi^* \left( \frac{t-b}{a} \right) dt; \quad (27)$$

where  $x(t)$  is the time series representing the input signal,  $\psi(t)$  is the mother wavelet, which is a localised function in both time and frequency domains,  $W(a, b)$  represents the wavelet coefficients as a function of scale  $a$  and translation  $b$ ,  $a$  is the scale parameter that controls the dilation or compression of the wavelet,  $b$  is the translation parameter that shifts the wavelet along the time axis, and  $\psi^*(t)$  denotes the complex conjugate of the mother wavelet. The scale parameter  $a$  is related to the frequency resolution analysis. For instance, large values of  $a$  correspond to analysing the signal at lower frequencies, capturing coarse details, while small values of  $a$  correspond to higher frequencies, capturing finer details. The translation parameter  $b$  shifts the wavelet along the time axis, allowing the analysis to focus on different parts of the signal.

In contrast, the DWT is often used in computational applications due to its efficiency. The DWT samples the wavelet transform on a discrete grid, typically with dyadic scales and shifts, and is defined as:

$$W_x[j, k] = \frac{1}{\sqrt{2^j}} \sum_{n=0}^{N-1} x[n] \psi \left( \frac{n-2^j k}{2^j} \right); \quad (28)$$

where  $j$  and  $k$  are integers that represent the scale and translation components,  $N$  is the number of samples in the signal, and  $\psi(t)$  is still the mother wavelet, now sampled at discrete intervals. The DWT decomposes the signal into approximation coefficients (low-frequency components) and detail coefficients (high-frequency components).



## 2. EXPLORING AND EXTENDING MATHEMATICAL METHODS FOR COMPLEX TIME SERIES ANALYSIS

In the previous chapter, a comprehensive discussion was provided on several contemporary mathematical algorithms for analysing real-time complex time series data, including Perfect Matrices of Lagrange Differences (PMLD), the Hankel matrix-based approach (H-rank), embedding attractors (uniform and non-uniform), permutation entropy (PE), and wavelet analysis. Each of these techniques has demonstrated promising results in complex time series analysis. However, there remains significant potential for further refinement and investigation within these methods. For instance, the PMLD matrix-based algorithm has been applied to ECG signals focusing primarily on two ECG parameters [13, 53]. The efficacy of the PMLD algorithm when applied to a broader range of ECG parameters is yet to be fully explored, as the complexity of the matrix increases with additional parameters. Furthermore, comparing the PMLD method with other matrix-based approaches could reveal whether it is optimal or if alternative matrix techniques might also offer additional value in ECG analysis. The initial introduction of the PMLD approach by Ziaukas et al. [13] and its subsequent application by Šiaučiūnaitė et al. [53] for studying complex cardiovascular processes prompt further investigation into its effectiveness across other cardiovascular diagnostic measures. Similarly, the Hankel matrix-based approach, utilised by Landauskas et al. [86] to integrate the Hankel matrices with weighted moving averaging for optimising time series prediction, has not yet been applied to the HRV dataset for the detection of group synchronisation purposes. Additionally, PE has yet to be evaluated for its applicability to HRV data, leaving an opportunity to assess its utility in this context.

This chapter provides a thorough examination and analysis of these mathematical algorithms, aiming to illuminate opportunities for extending existing techniques, such as PMLD and Hankel matrix-based approaches. Additionally, this section will propose new mathematical algorithms and assess their applicability to ECG data analysis.

### 2.1 Configurable Structure of PMLD for Enhanced ECG Analysis

As discussed in previous sections, the PMLD has been successfully applied to the analysis of ECG signals [13, 53]. A particularly noteworthy, yet underexplored, aspect of PMLD is the inherent flexibility in its matrix configuration, offering a unique degree of freedom that allows for the interchangeability of matrix elements without altering the matrix's maximum absolute eigenvalue [13]. This feature is especially relevant when analysing complex physiological signals, where different configurations might unveil distinct characteristics of the underlying dynamics.

To illustrate, consider a second-order matrix derived from two synchronously recorded time series ( $x_n: n = 0, 1, 2, 3 \dots$ ) and ( $y_n: n = 0, 1, 2, 3 \dots$ ). Within the constraints of the six predefined criteria that define a perfect Lagrange matrix [13], there are four distinct configurations in which these elements can be arranged. Each

configuration represents a different structural arrangement of the matrix, offering a unique lens through which the data can be interpreted:

$$A_1 = \begin{bmatrix} x_n & x_{n+1} - y_{n+1} \\ x_{n-1} - y_{n-1} & y_n \end{bmatrix}, \quad (29)$$

$$A_2 = \begin{bmatrix} x_n & y_{n+1} - x_{n+1} \\ y_{n-1} - x_{n-1} & y_n \end{bmatrix}, \quad (30)$$

$$A_3 = \begin{bmatrix} x_n & x_{n+1} - y_{n+1} \\ y_{n-1} - x_{n-1} & y_n \end{bmatrix}, \quad (31)$$

$$A_4 = \begin{bmatrix} x_n & y_{n+1} - x_{n+1} \\ x_{n-1} - y_{n-1} & y_n \end{bmatrix}. \quad (32)$$

Though these configurations may differ only slightly, their implications for the analysis can be profound. The choice of a specific matrix structure can lead to variations in the interpretation of the signal's dynamics, and thus, the outcomes of the analysis. For instance, selecting a particular configuration might enhance the sensitivity of the analysis. This flexibility in configuration also opens up new avenues for tailoring the PMLD approach to specific research objectives. Depending on the study's goals, researchers can choose the configuration that best aligns with their analytical needs. This could involve exploring multiple configurations to determine which yields the most insightful results, or it could mean developing new criteria for selecting the optimal configuration based on the characteristics of the time series being analysed.

Moreover, this degree of freedom within PMLD could have significant implications for extending its application beyond the ECG signal analysis. For example, it could be adapted to analyse other physiological signals, such as respiratory patterns or neural oscillations, where the relationship between multiple time series is of interest. In such cases, the choice of matrix configuration could play a critical role in uncovering subtle interactions between physiological processes that might otherwise go unnoticed. In conclusion, the PMLD's flexibility in matrix configuration represents a powerful tool for researchers, offering the potential to customise the analysis of scalar time series in ways that best meet the demands of their specific study.

## 2.2 Improving PMLD Sensitivity and Variability Using Higher-Order Matrix Expansion

The idea of matrix order is central to advancing the ECG data analysis, particularly when aiming to improve sensitivity and variability in the results. Increasing the matrix order enriches the analytical framework, enabling it to capture more complex relationships and subtle details within the multivariate data. This process can be linked to enhancing a machine learning algorithm with additional layers or features, allowing the proposed model to process and interpret more intricate

patterns. It is important to note that the term “machine-trained model” refers specifically to the computational techniques proposed herein, which emulate conventional machine-training models in terms of accuracy. This is evident in their ability to produce more efficient results as additional data is incorporated into the algorithm. However, it is important to clarify that these models differ from traditional machine learning models such as supervised learning methods (e.g. decision trees, support vector machines, and neural networks) and unsupervised learning methods (e.g. clustering algorithms like k-means and dimensionality reduction techniques like principal component analysis).

When applying this concept to ECG parameter analysis, higher-order matrices offer a more detailed and comprehensive view of the data, incorporating more ECG parameters. For example, one can view the matrix architecture as a sophisticated analytical tool; increasing its order allows for the integration of a broader range of ECG parameters and the assessment of relationships between them. This expanded capacity results in enhanced sensitivity, meaning the matrix can more effectively detect subtle variations in the ECG signals [106]. Moreover, higher-order matrices contribute to increased variability in the analysis. Variability, in this sense, refers to the dispersion of data points and how they spread across Gaussian distribution curves (these issues are discussed later in the thesis). This broader variability is critical for distinguishing between different cardiac conditions and improving the classification accuracy of test subjects. By accommodating a wider range of data distributions, higher-order matrices help to identify better and characterise diverse physiological states, which is essential for accurate diagnosis.

### 2.3 Comparative Analysis: PMLD vs. SMF1 and SMF2

Navickas et al. [107] introduced two matrix architectures for examining the relationships between two time series,  $(x_n: n = 0, 1, 2, 3 \dots)$  and  $(y_n: n = 0, 1, 2, 3 \dots)$ . Given the two time series, the second-order matrix framework SMF1 is defined as [107]:

$$\begin{bmatrix} 2x_n & x_{n+1} - y_{n+1} \\ x_{n-1} - y_{n-1} & 2y_n \end{bmatrix}. \quad (33)$$

From (33), it is evident that all six conditions required for the PMLD are also met by SMF1. The primary distinction between equation (1) and equation (33) is that the elements on the main diagonal are scaled by a constant factor. As noted in [13], the multiplication of the zero-order differentials by a scalar will reduce the algorithm’s ability to detect subtle changes within the time series; therefore, ECG analysis can be better explored by using PMLD matrices.

The structure of SMF1 also allows for straightforward expansion to higher dimensions (the third-order matrix). For example, if three time series  $(x_n: n = 0, 1, 2, 3 \dots)$ ,  $(y_n: n = 0, 1, 2, 3 \dots)$ , and  $(z_n: n = 0, 1, 2, 3 \dots)$  are considered, they can be integrated into the PMLD framework as follows:

$$\begin{bmatrix} 2x_n & x_{n+1} - y_{n+1} & x_{n+1} - z_{n+1} \\ y_{n-1} - x_{n-1} & 2y_n & y_{n+1} - z_{n+1} \\ z_{n-1} - x_{n-1} & z_{n-1} - y_{n-1} & 2z_n \end{bmatrix}. \quad (34)$$

Note that all six requirements for the PMLD are also applied to equation (34). Navickas et al. [107] also proposed another matrix architecture for analysing complex time series. It is denoted by SMF2 and can be read as:

$$\begin{bmatrix} x_n + z_n & x_{n+1} - y_{n+1} & z_{n+1} - x_{n+1} \\ x_{n-1} - y_{n-1} & 2y_n & y_{n+1} - z_{n+1} \\ z_{n-1} - x_{n-1} & y_{n-1} - z_{n-1} & z_n + x_n \end{bmatrix}. \quad (35)$$

The major difference between the SMF1 (34) and the SMF2 (35) lies in the elements on the main diagonal. Unlike SMF1, the lexicographical balance is not preserved in (34). Also, the SMF1 matrix can be expanded to higher orders; however, multiplying the zero-order derivative elements by a scalar greater than one actually reduces its ability to detect subtle variations in the analysed signals, as explained in [13]. On the other hand, the SMF2 architecture cannot be expanded to higher orders because it does not meet the necessary conditions for matrix expandability, as explained in [13]. If the ability to expand the matrix is not essential, such as when using only two cardiac intervals for analysis, then these proposed matrix architectures are well-suited for the task. As highlighted in [75], no single algorithm is universally superior; the choice depends on the specific analytical needs. Therefore, the best approach is to evaluate all matrix architectures and select the one that performs most effectively.

## 2.4 Second-Order Time-Delayed Pattern Matrices for Multivariate Time Series Analysis

To compute time-delay patterns between the time series  $(x)$  and  $(y)$ , we define a set of indices  $I = \{k - R, k - R + 1, \dots, k + R\}$ , where  $R$  represents the radius of averaging. The time series  $(y)$  is shifted to the right by  $\delta$  time steps relative to  $(x)$ . The mean difference between corresponding elements of  $(x)$  and  $(y)$  within the index set  $I$  is calculated as:

$$D(k, \delta, R) = \frac{1}{2R+1} \sum_{j \in I} \alpha_j \cdot (x_j - y_{j+\delta}); \quad (36)$$

where  $\alpha_j$  are weighting coefficients determined by a Gaussian-type distribution centred around  $j = k$ , and  $k$  is the current point in time. These coefficients  $\alpha_j$  follow the continuous representation of the Gaussian distribution function:

$$f(t) = \frac{1}{\beta} e^{-\frac{1}{2} \left( \frac{t-k}{\sigma} \right)^2}; \quad (37)$$

where  $\beta$  normalises the coefficients such that  $\sum_{j \in I} \alpha_j = 1$ , and  $\sigma$  controls the spread of the Gaussian function. As  $\sigma$  increases,  $\alpha_j$  approaches uniformity across  $I$ ; as  $\sigma$  decreases to zero,  $\alpha_j$  emphasizes the central point  $k$ . For the given computations,  $R = 2$  and  $\sigma = 20$  are defined. These parameters standardise the radius of averaging and the spread of the Gaussian distribution across subsequent analyses. This methodology

provides a robust framework for quantifying the temporal relationships and dependencies between the time series ( $x$ ) and ( $y$ ) through weighted averaging, ensuring sensitivity to local variations and systematic changes in the time series data over time. The pictorial representation of the proposed algorithm is depicted in Fig. 2.

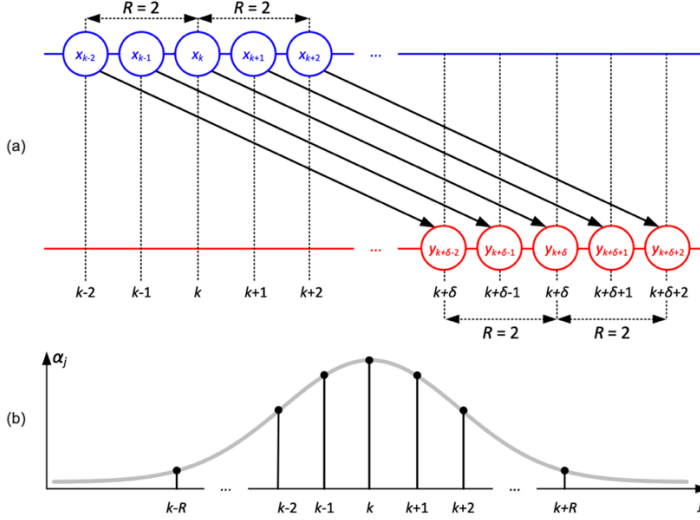


**Fig. 2.** Diagram Illustrating the Computation of Time-Delay Patterns between Time Series ( $x$ ) and ( $y$ ) Highlighting the Algorithm for Analysing their Temporal Relationships

The proposed algorithm computes the time-delay patterns between two time series ( $x$ ) and ( $y$ ) and is used to analyse the algebraic relationship between the RR inter-beat interval and the duration of the JT wave during the stress test. It iterates over each time moment  $k$  and calculates the mean differences between the segments of ( $x$ ) and the corresponding time-shifted segments of ( $y$ ) within a specified radius  $R$  and across different time delays. These differences are weighted using a Gaussian-type distribution centred around  $k$ , emphasising the temporal alignments between the two time series. The resulting time-delay patterns are stored in the predefined matrix architecture. This computational approach aids in analysing the ECG parameters for understanding the complex relationship between the RR and JT intervals and their adaptations within the cardiovascular system during a stress test.

Wavelet analysis is another powerful tool for examining complex time series data. It is particularly valuable in ECG analysis, where different frequency components can represent distinct physiological processes. Unlike traditional Fourier methods, wavelet analysis provides a more versatile approach, capable of capturing both slow and rapid variations within signals. The use of built-in applications within MATLAB significantly simplifies the application of computational techniques, such as wavelet analysis, making them accessible and efficient for complex signal processing tasks like ECG analysis. For instance, the one-dimensional CWT offers a straightforward yet powerful method for analysing the parameters of ECG signals. By

decomposing the ECG signal into different scales, 1D-CWT enables the detection of various physiological events and can aid in identifying arrhythmias or other cardiac abnormalities. Furthermore, MATLAB's graphical interface enhances this process by providing options, such as the colouration mode, which allows for detailed visual analysis of the wavelet coefficients. In colouration-by-scale mode, the coefficients are individually scaled at each wavelet scale, facilitating the examination of features across different resolutions. Alternatively, in the all-scale colouration mode, the wavelet coefficients at all scales are combined to create a comprehensive visualisation, offering an overall perspective of the signal's structure [108]. When performing wavelet analysis on ECG data, features such as the sampling period, typically set at one heartbeat by default, and the selection of specific wavelets like the Shan wavelet [108], allow for precise control during the analysis process. The Shan wavelet, when applied at scales 1–64, effectively captures the intricate details of the ECG signal. The analysis is further enhanced by focusing on coefficients at the median scale (e.g. scale 32 when analysing scales 1–64), which balances the capture of both coarse and fine details. The flexibility and precision of these tools make the Shan wavelet an invaluable resource in biomedical signal processing, enabling researchers to uncover hidden patterns and dynamics within ECG parameters with relative ease [108].

## 2.5 Calibration of the H-Rank Algorithm Based on Coupled Logistic Maps

To thoroughly understand how the H-rank algorithm operates on HRV data, it is crucial first to evaluate its effectiveness using a synthetic dataset. The synthetic dataset chosen for this analysis is derived from the master–slave coupled logistic map equations. This chaotic model generates time series that serve as an ideal example to showcase the efficiency of the H-rank algorithm in extracting the algebraic elements needed to reconstruct the original complex time series. Moreover, this exploration will help visualise the synchronisation process between the two systems (the master and the slave), thereby highlighting the effectiveness of the H-rank algorithm.

The master–slave coupled (MSC) logistic map model is extensively explored in the study of chaotic systems and synchronisation, with applications spanning from neuroscience to secure communications [109, 110]. The master–slave coupled logistic map has been widely cited in the literature, with a particularly notable reference being the work by Brown et al. [111]. In the MSC model, the master system controls the dynamics, and the slave system follows its lead, allowing synchronisation between the two systems to be observed. Synchronisation in chaotic systems can take many forms, such as amplitude envelope synchronisation, where the overall amplitude patterns are matched [112], or lag synchronisation, where one system's behaviour lags behind but is still correlated with the other system [113]. The MSC model, when analysed with the H-rank technique, reveals these intricate forms of synchronisation, demonstrating the algorithm's ability to detect subtle interactions between coupled chaotic systems [114–116].

The equation of the MSC model reads as follows:

$$x_{k+1} = r_k x_k (1 - x_k), \quad (38)$$

$$y_{k+1} = r_y q_k (1 - q_k), \quad (39)$$

$$q_k = \Delta x_k + y_k \cdot (1 - \Delta). \quad (40)$$

Equation (38) represents the well-known logistic map. In this model, the discrete variable  $x_k$  is constrained to the interval  $[0, 1]$ , assuming the initial value  $x_0$  is also within this range, and the parameter  $r_k$  is between 0 and 4. For simulation purposes,  $x_0$  is set to 0.1 and  $r_k$  is set to 3.9, ensuring the chaotic behaviour in the master system. The dynamics of the slave system are governed by the equation (39), where the parameter  $r_y$  is set to 3.89. The interaction between the master and slave systems is governed by the equation (40), and the coupling strength is regulated by the coupling parameter  $\Delta$ . When  $\Delta$  is set to 0, the master and the slave systems operate independently. Conversely, when  $\Delta$  is equal to 1, the master and slave systems are fully coupled, meaning that the slave system is entirely influenced by the master system. These dynamics are visually represented in Fig. 3. There are four subplots shown in Fig. 3, arranged from top to bottom. In Fig. 3, the first subplot shows the time series for the master and slave systems. The coupling parameter is shown in the second subplot. The difference between the two systems is shown in the third subplot, and the H-ranks computed for the two systems are shown in the fourth subplot. When  $\Delta$  is small, the H-ranks of the two systems show significant disparity, reflecting the greater complexity of the master system compared to the slave system due to the different parameters in their logistic maps. As the two time series begin to synchronise, the H-ranks of the systems converge closely, though not perfectly, since  $\Delta$  is not set to 1.

## MSC Logistic map

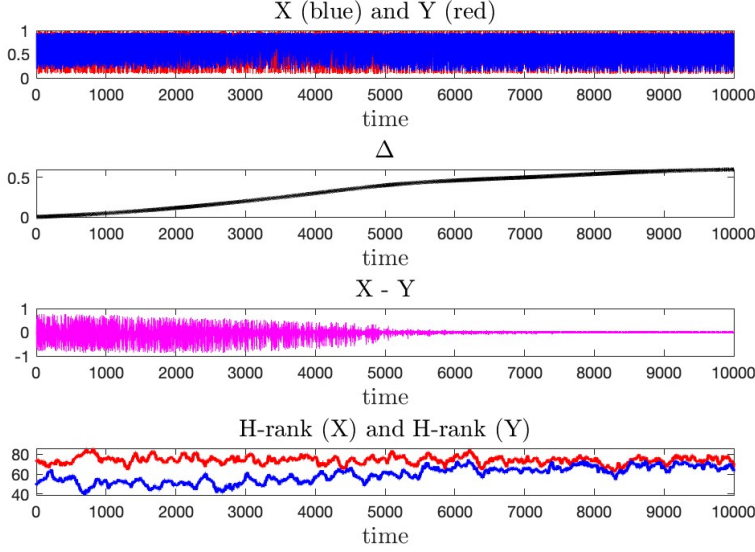


**Fig. 3.** The Master–Slave Coupled Logistic Map: Time Series of the Master System (Red) and the Slave System (Blue); the Coupling Parameter; their Difference; and the H-ranks Computed for the Slave (Blue) and the Master (Red)

To enhance the clarity of trends and reduce noise in scalar time series data obtained from the H-rank algorithm-based approach, applying a simple moving average (SMA) can be highly effective. For instance, when analysing HRV data, where the H-rank values are derived using the H-rank algorithm, the SMA can be employed to smooth these values. In mathematical terms, if the HRV time series is represented by  $x(k)$  with a total length  $L$ , the SMA at a specific time point  $k$  is calculated using the following formula:

$$y(k) = \frac{1}{2m+1} \sum_{s=-m}^m x(k+s); \quad (41)$$

where  $x(k)$  denotes the original value of the time series at time  $k$ ,  $m$  is the window size for the moving average, which determines how many neighbouring values are included in the averaging process, and  $y(k)$  represents the smoothed value at time  $k$ . The SMA works by averaging the value of  $x(k)$  with  $m$  preceding and  $m$  following values in the time series, thereby reducing the impact of short-term fluctuations and highlighting longer-term trends.

Permutation entropy (PE) can also be utilised to analyse the complexity of HRV data across multiple time series by reconstructing the time series into a  $m$ -dimensional state space with a time delay of 1. For each segment of the time series, a permutation vector is created based on the order of values within the  $m$  dimensional vector. Specifically, if the time series is denoted as  $y(t)$ , each segment is represented as:

$$Z_h^{m,1} = \{y_h, y_{h+1}, \dots, y_{h+(m-1)}\}. \quad (42)$$



The values in each segment are then ordered to form a permutation sequence  $T_h$ . The frequency of each possible permutation pattern is computed across the entire time series, resulting in a histogram of permutation occurrences. The permutation entropy  $H_{PE}(m)$  is calculated using:

$$H_{PE}(m) = -\sum_{w=1}^{n!} Q_w^{m,1} \ln(Q_w^{m,1}); \quad (43)$$

where  $Q_w^{(m,1)}$  represents the relative frequency of permutation  $w$  within the time series. Specifically, if the focus is on the number of forbidden patterns—that is, the permutations that do not occur in the data—then the variable  $Z_n$  (where  $n = 1, 2, 3, \dots$ ) tracks the count of these forbidden patterns for different data streams. As the length of the time series increases, monitoring the number of forbidden patterns helps to understand how the complexity and randomness of the HRV data evolve. This analysis highlights the structural dynamics and potential irregularities in the HRV time series by quantifying the distribution and occurrence of permutation patterns.

This section explored a variety of pre-existing mathematical algorithms designed to analyse complex time series data, which can be effectively adapted for ECG signal analysis. These algorithms are suitable for handling time series derived from both static ECG recordings and those obtained during stress tests. In the case of ECG recordings containing two time series representing different cardiac conditions, the data is first transformed into a matrix structure using specialised techniques (already discussed in detail). The elements of this matrix represent ECG parameters such as the RR interval, P wave duration, QRS complex duration, and P wave amplitude, allowing for their algebraic relationships to be analysed. Once the ECG parameters are analysed using the matrix-based method, the next step is to generate a scalar time series. This scalar time series is referred to as the “feature-enhanced time series” because it has undergone specific transformations, allowing its features to be amplified or highlighted using specialised techniques that enable the extraction of key characteristics from the ECG data. The resulting feature-enhanced time series is then used for further statistical analysis, offering deeper insights and enabling additional analyses, which are explained in detail in the subsequent section.

## 2.6 Statistical Methods for Generating Variation Intervals for Classification and Health Biomarkers

The feature-enhanced time series is subjected to further analysis using various statistical techniques. The purpose of the statistical investigation is twofold. First, the aim is to generate the distributions of the two classes, healthy (H) and unhealthy (U) subjects and then generate the variation intervals based on those distributions. Second, the aim is to develop health indicator(s). However, these statistical processes are not straightforward and involve multiple steps, which will be outlined in detail below.

These steps range from simple to more advanced statistical methods used to examine the feature-enhanced time series. Additionally, this thesis introduces some original mathematical formulas designed to contribute to the creation of health indicator(s). Since this process incorporates and builds on pre-existing knowledge about the two classes (healthy and unhealthy subjects), it can be considered crucial

for the development of a machine-trained model. As will be highlighted later, the integration of more data into the proposed techniques will further enhance accuracy and classification outcomes.

In the analysis of the feature-enhanced time series, a variety of statistical techniques can offer valuable insights. A fundamental aspect of this analysis involves summarising the central tendency and dispersion of the featured-enhanced time series. Descriptive statistics, such as the mean ( $\mu$ ), the variance ( $\sigma^2$ ), or the standard deviation ( $\sigma$ ), usually offer some insight. The mean of the featured-enhanced time series is given by:

$$\mu = \frac{1}{N} \sum_{i=1}^N z_i; \quad (44)$$

where  $N$  represents the total number of observations in the time series, and  $z_i$  represents each value in the feature-enhanced time series. Similarly, the variance, which measures the spread of the data, is calculated as:

$$\sigma^2 = \frac{1}{N} \sum_{i=1}^N (z_i - \mu)^2; \quad (45)$$

where  $\mu$  is the mean of the time series as calculated in equation (45), and  $z_i$  represents each value in the feature-enhanced time series. These two fundamental statistical measures – the central tendency of the data and its dispersion – are crucial for understanding the behaviour of the feature-enhanced time series. They provide insights into how data points are distributed and how they vary within a class. This is particularly useful when analysing two distinct groups, as the healthy and unhealthy classes may exhibit similar patterns within their respective groups but show significant differences when compared to each other. For instance, when analysing  $X$  number of subjects in the healthy class and  $Y$  number of subjects in the unhealthy class, these basic statistics can provide a single representative value for each subject in those classes. Therefore, they help to summarise the overall behaviour of healthy and unhealthy classes in a simple yet meaningful way.

Once the basic statistics are performed to obtain a clear distinction between the two classes, further statistical analysis may also be beneficial, especially when the goal is to understand the distribution of the data points. If the aim is to look for normally distributed data points, the empirical rule (often referred to as the 68–95–99.7 rule) comes into play. This rule states that for a normal distribution, approximately 68% of the data points fall within one standard deviation ( $\sigma$ ) around the mean ( $\mu$ ); approximately 95% fall within two standard deviations, and 99.7% fall within three standard deviations. Mathematically, the one-sigma portion of this rule can be expressed as:

$$P(\mu - \sigma \leq X \leq \mu + \sigma) \approx 0.6827; \quad (46)$$

where  $X$  is a random variable that follows a normal distribution,  $\mu$  is the mean of the distribution, and  $\sigma$  is the standard deviation.

Building on this, the Gaussian distribution (or normal distribution) can provide further insights into the data distribution for the two classes. A Gaussian distribution

is a continuous probability distribution characterised by its bell-shaped curve, symmetric about the mean. It is mathematically expressed as:

$$f(x) = \frac{1}{\sigma\sqrt{2\pi}} e^{-\frac{(x-\mu)^2}{2\sigma^2}}; \quad (47)$$

Again,  $\mu$  is the mean,  $\sigma$  is the standard deviation, and  $x$  is the random variable. Another important statistical measure is the Anderson–Darling (AD) test. The AD test is a statistical method used to evaluate whether a given dataset follows a normal distribution. It is a modification of the Kolmogorov–Smirnov test, specifically designed to give more weight to the tails of the distribution. The AD test helps determine whether the transformed components follow a normal distribution, thus validating the model’s assumptions. Mathematically, the AD test is defined as follows [117, 118]:

$$A^2 = -N - \frac{1}{N} \sum_{i=1}^N \left( (2i-1) [\ln F(Y_i) + \ln(1 - F(Y_{N+1-i}))] \right); \quad (48)$$

where  $N$  is the sample size,  $F$  is the cumulative distribution function (CDF) of the reference distribution, and  $Y_i$  is the ordered data points.

The use of simple statistics on the feature-enhanced time series yields the data points for each time series, which are then used to create the distributions for the two classes. These distributions facilitate the generation of a variation interval using the one-sigma rule, forming the foundation for the proposed classification technique. At this stage, the entire setup is referred to as a machine-trained model. The rationale is straightforward: as more data points are added, meaning more subjects are included, the distributions of the data points become more refined, and the variation intervals become more accurate, improving the overall classification model.

Once the classification model is established, the ECG of a test subject (which is referred to as (R)) can be evaluated within this classification. First, the subject’s ECG is processed using the matrix-based algorithm, then the feature-enhanced time series is generated. Similar statistical methods are applied to extract the data point (the variance value) for this time series (R). The value of (R) is then evaluated against the three distinct conditions, with an interpolation coefficient (I) calculated accordingly. The first condition defines the equation for the signature corresponding to the healthy class, establishing a reference point for classification against other health status categories.

**Condition No 1:** The equation for the signature for the healthy class reads:

$$R \leq (\mu_h - \sigma_h) \text{ then } (I = 0). \quad (49)$$

**Condition No 2:** The equation for the signature for the unhealthy class reads:

$$R \geq (\mu_u + \sigma_u) \text{ then } (I = 1). \quad (50)$$

**Condition No 3:** The equation for the signature for the intermediate class reads:

$$(\mu_h - \sigma_h) \leq R \leq (\mu_u + \sigma_u) \text{ then } I = \frac{R - (\mu_h - \sigma_h)}{(\mu_u + \sigma_u) - (\mu_h - \sigma_h)}. \quad (51)$$

These conditions are applied to classify (R) into the healthy or unhealthy category. For example, in diagnosing atrial fibrillation (AF) episodes, the ECG of a test candidate is first computationally processed using a matrix-based algorithm and later it is processed through the entire statistical routine to be classified as either healthy or unhealthy.

Similarly, if the goal is to analyse the self-organisation of the cardiovascular system during physical activity for two classes, the initial step involves computing the parameters of the ECG using a matrix-based algorithm. Then, the feature-enhanced scalar time series is obtained. Following this step, key parameters such as the velocity of adaptation (denoted as A) and the modified velocity of adaptation (denoted as B), along with other indicators, are calculated. The parameters A and B are used to calculate the first health indicator, referred to as alpha ( $\alpha$ ). First, the difference between A and B is calculated:

$$X = \frac{A-B}{A} \times 100\%. \quad (52)$$

Then, the health indicator  $\alpha$  is derived by normalising (X) across the entire class:

$$\alpha = \frac{X - \min(X)}{\max(X) - \min(X)}. \quad (53)$$

Similarly, another health indicator, beta ( $\beta$ ), can be calculated when analysing the variability in the parameter(s) signal during the different phases of the exercise using Shan wavelet analysis. Depending on the study's objectives, the signal may be divided into three segments (say  $C_1, C_2, C_3$ ), and then the means of those segments ( $\mu_{C_1}, \mu_{C_2}, \mu_{C_3}$ ) are calculated. In this context, the author of the thesis proposes dividing the signal into three segments and interpolating it with a quadratic equation,  $y = ax^2 + bx + c$ , across those three segments. To do so, it is important to find the deviation between the mean of the middle segment  $\mu_{C_2}$  and the average of the outer segments  $\mu_{C_1}$  and  $\mu_{C_3}$ , respectively. This segment deviation is termed d and reads as follows:

$$d = \frac{\mu_{C_1} + \mu_{C_3}}{2} - \mu_{C_2}; \quad (54)$$

where  $\mu_{C_1}$ ,  $\mu_{C_2}$ , and  $\mu_{C_3}$  represent the means of the first, second, and third segments, respectively. Another health indicator,  $\beta$ , can be defined as:

$$\beta = \frac{d - \min(d)}{\min(d) - \max(d)}. \quad (55)$$

Note that the health indicators alpha ( $\alpha$ ) and beta ( $\beta$ ) define two different aspects of the functionality of the cardiovascular system during the stress test. These two aspects occur during the load and recovery phases, respectively, and therefore, it is important to determine the overall response—or, in other words, the combined effect—of these two aspects. Thus, the overall health status of an individual's cardiovascular system is represented by the parameter gamma ( $\gamma$ ), which is calculated as:

$$\gamma = \frac{\alpha + \beta}{2}. \quad (56)$$

Another useful statistical tool that can be used to analyse the HRV data of the two classes is the box plot representation. A box plot graphically depicts the data distribution based on a five-number summary: the minimum, the first quartile ( $Q_1$ ), the median, the third quartile ( $Q_3$ ), and the maximum. The interquartile range (IQR), defined as ( $Q_3 - Q_1$ ), highlights the spread of the middle 50% of the data, with data points outside  $Q_1 - 1.5 \times \text{IQR}$  or  $Q_3 + 1.5 \times \text{IQR}$  considered potential outliers. This method is particularly effective in understanding the variability and skewness of ECG intervals across different subjects.

It is equally important to consider that the proposed results can be effectively communicated to a broader audience, including those without technical expertise, through the use of straightforward visualisation tools. Such tools can make the interpretation of complex data easier. One effective method for visualising the classification results is by employing a semi-gauge indication tool. The semi-gauge indication tool is designed based on the specific criteria and conditions outlined in earlier sections. Its significance lies in two key aspects: first, it is built upon the extensive mathematical and statistical analysis based on the predefined conditions; second, it helps to visualise the overall outcomes, thereby providing a clear and meaningful representation of the analysis. The semi-gauge uses a three-colour scheme—green, yellow, and red—to convey the results. Green indicates a healthy status, suggesting that the individual’s cardiovascular system is functioning well and responding appropriately. Yellow represents a cautionary status, indicating that the individual may have some irregularities or areas of concern that should be monitored, though immediate medical attention might not be necessary. Red, in the semi-gauge indication tool, signals an unhealthy status, suggesting that the individual is likely experiencing significant issues with their cardiovascular system and may require immediate medical intervention. This visual representation allows even those without a background in statistics or medical diagnostics to quickly grasp the significance of the results.

The following chapter will provide a comprehensive and detailed explanation of the application of matrix-based algorithms and statistical techniques for various diagnostic measures. These measures may include the self-organisation of the cardiovascular system under external load in two different classes, the collapse of complexity during the physical exercise, the early detection of atrial fibrillation episodes, and HRV analysis for the examination of complexity matching. Each of these applications represents a critical area of research due to their significant clinical importance. Consequently, they are analysed using both established and newly proposed state-of-the-art algorithms to ensure accurate and meaningful results.

### **3. ALGORITHMS AND APPLICATIONS IN CARDIAC SIGNAL ANALYSIS**

#### **3.1 PMLD Matrix-Based Algorithm for Cardiovascular Complexity Collapse during Stress Tests (Load Phase)**

Perfect matrices of the Lagrange differences (PMLD) have been utilised for analysing ECG parameters in the following research studies [13, 73, 119]. These studies demonstrated that PMLD is an effective matrix-based algorithm, even for small datasets. In this work, PMLD is also adopted to analyse the interplay between heart rate (HR) and arterial blood pressure (ABP) during physical activity, known as the stress test. This is crucial because an individual may appear physically fit and healthy, yet their cardiovascular response to exercise may be suboptimal. Such diagnoses are important for generating cardiovascular health warnings, enabling individuals to seek medical attention if necessary.

It is also well anticipated that both hypertensive and normotensive persons experience subtle and relative variations in the heart rate (HR) and the arterial blood pressure (ABP) regulation during physical activity. However, the analysis of these subtle changes can help to determine an individual's cardiovascular response to physical activity and their ability to handle the physical load (the stress test). The stress test consists of two phases: the load phase and the recovery phase. This study aims to examine the interplay between HR and ABP, particularly during the loading phase of the exercise. This analysis helps to understand the collapse of complexity that occurs during the load phase and reveals subtle changes that are occurring in the cardiovascular system in response to the physical exercise. This analysis is based on prior knowledge about the study subjects, where ECG data is collected from two groups: those with normal arterial blood pressure (referred to as the healthy group) and those with elevated blood pressure (referred to as the unhealthy group). Various statistical techniques are also applied to identify the range of variation in ECG signals, which helps in the development of classification techniques. Additionally, a decision support system has been developed to test and classify new subjects based on these findings.

The human cardiovascular response during physical activity may be evaluated by variations in HR and ABP, as both exhibit a direct relationship [49]. The physical exercise stimulates the activity of the sympathetic nervous system. To meet the rising metabolic demands in the skeletal muscles, the circulatory system must effectively manage the transport of oxygen and carbon dioxide. Thus, the three systems shown in Fig. 4 (a simplified version of Fig. 1) are activated during the exercise and must function coherently and simultaneously. In Fig. 4, the emphasis is mainly focused on the heart rate and blood pressure dynamics during the exercise only [53, 65, 120, 121].

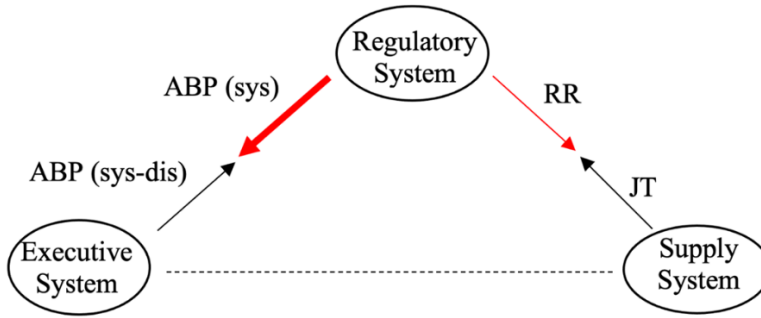


**Fig. 4.** Simplified Model of Executive, Supply, and Regulatory Systems for Analysing Heart Rate and Blood Pressure Variations during the Stress Test

In Fig. 4, a two-way connection is illustrated by red and black arrows between the regulatory system and the supply system, as well as between the regulatory system and the executive system. The connectivity between the supply system and the executive system is depicted by a dotted line because it is not examined in this work.

The relationship between the regulatory system and the supply system shows the changes in heart rate, characterised by the ECG parameters, the RR interval and the JT wave. The RR cardiac interval provides information on the functioning of the heart, brain, and autonomic nervous system interaction. Changes in this interval impart information about the ability of the cardiovascular system to self-regulate, adapt, and respond flexibly to potential changes [122-124].

The JT wave shows the functionality of the lower chambers of the heart during the stress test [121]. The JT interval has two parts:  $JT_a$ , which marks the start of the T wave peak, and  $T_e$ , which marks the end of the T wave peak. During the exercise, the nervous system triggers changes in the JT wave and body metabolism affects repolarisation. Thus, a shorter JT wave represents quicker repolarisation and metabolic responses, while a longer JT wave signifies a slower response. This difference is known as the JT interval variance and is represented as  $JT_d$ , showing uneven activity of the heart muscle. In healthy individuals, the JT shortens to 160 ms during the exercise, but in those with heart disease, it shortens more significantly during the exercise [124-126].

The difference between systolic and diastolic blood pressure signifies the relationship between the regulatory system and the supply system. It is represented as (sys-dis) (see Fig. 4). As mentioned earlier, during the exercise, normotensive individuals experience a linear rise in the systolic blood pressure within the range of 200 to 249 mmHg, whereas the diastolic blood pressure stays closer to the resting level. For hypertensive individuals, both the systolic and diastolic blood pressure tend to increase during the exercise [127].

As noted in earlier paragraphs, both normotensive and hypertensive persons experience an increase in the heart rate and the blood pressure during the physical activity. It is hypothesised in this study that monitoring the rate at which these subtle variations occur in heart rate and blood pressure is significant and provides substantial information about the cardiovascular system's functionality, which is useful for

diagnostic purposes. In other words, the goal is to follow the regulation path during physical exercise. This study is especially notable for the application of PMLD matrices. Furthermore, statistical analysis techniques are also adopted for the development of a decision support system to create health biomarkers.

### **Bioethical Statement**

This study meets all the criteria for experimental ethics. Permission to conduct the experimental studies was granted by the Kaunas Regional Biomedical Research Ethics Committee (No. BE-1-30). All participants provided informed written consent to conduct the biomedical studies (see Annexes A and B).

### **Stress Test and the Experiment Protocol**

The stress test is typically performed on a stationary bicycle ergometer to monitor the cardiovascular response to increased physical activity systematically. At the beginning of the exercise, the load is set to a specified value in watts and is gradually raised to a predetermined range at a certain rate. This phase of the exercise is known as the load phase, during which the heart rate increases. The load phase is immediately followed by the recovery phase, during which the individual's cardiovascular system gradually returns to its resting state [49, 53].

In this study, the Kaunas Load System is used to synchronously register 12-lead ECG data for a cohort of twenty-one individuals during the stress test [14, 128]. The Kaunas Load system is facilitated by the Institute of Cardiology, Lithuanian University of Health Sciences. The protocol commenced on 4 June 2020. The initial load of the bicycle ergometer is set to 50 watts. It is important for participants to maintain a consistent spinning rate of 60 revolutions per minute (*rpm*). The exercise is terminated when the individual fails to maintain this constant spinning rate. This protocol also aligns with the initial clinical indications for experiment termination according to the American Heart Association (AHA) exercise protocols [64].

### **Demographic Characteristics of the Study Cohort**

A total of twenty-one subjects were tested in this study. All participants were non-athletic, physically active men. Ten participants had normal blood pressure regulation and were categorised as healthy subjects, denoted as  $H_n$ .  $H$  indicates the healthy cohort, and  $n$  represents the number of individuals in the cohort. The remaining eleven participants had a history of hypertension and were classified as unhealthy subjects, denoted as  $U_n$ . The demographic profile of the twenty-one individuals includes the mean and standard deviation data for their height ( $178.88 \pm 0.071$  m), weight ( $80.53 \pm 10.01$  kg), average age ( $41.11 \pm 10.21$  years), and body mass index ( $25.10 \pm 2.06$  kg/m<sup>2</sup>) [49].

### **Dataset Overview and Software Description**

As previously noted, 12-lead ECG data were recorded using the Kaunas Load system. The ECG data include temporal and amplitude information for the following ECG parameters: JT wave (measured in milliseconds, ms); QRS complex segment (measured in milliseconds, ms); RR wave inter-beat interval (measured in milliseconds, ms); P wave duration (DP) (measured in milliseconds, ms); P wave amplitude (AP) (measured in millivolts, mV); and time (measured in milliseconds,



ms). The total duration of the experiment did not exceed twenty minutes. The retrieved information was stored in a .txt-format text file, and all computations were performed using MATLAB software. The primary focus of this study revolves around the RR inter-beat interval and the JT wave duration in order to find temporal algebraic relationships between these two ECG parameters and thereby characterise the interplay between HR and ABP [49].

### Structural Configuration of the Proposed Algorithm

The architectural layout of this study is visually presented in Fig. 5. The entire framework of the study is classified into three main blocks. Each of these blocks is thoroughly explained and discussed below.

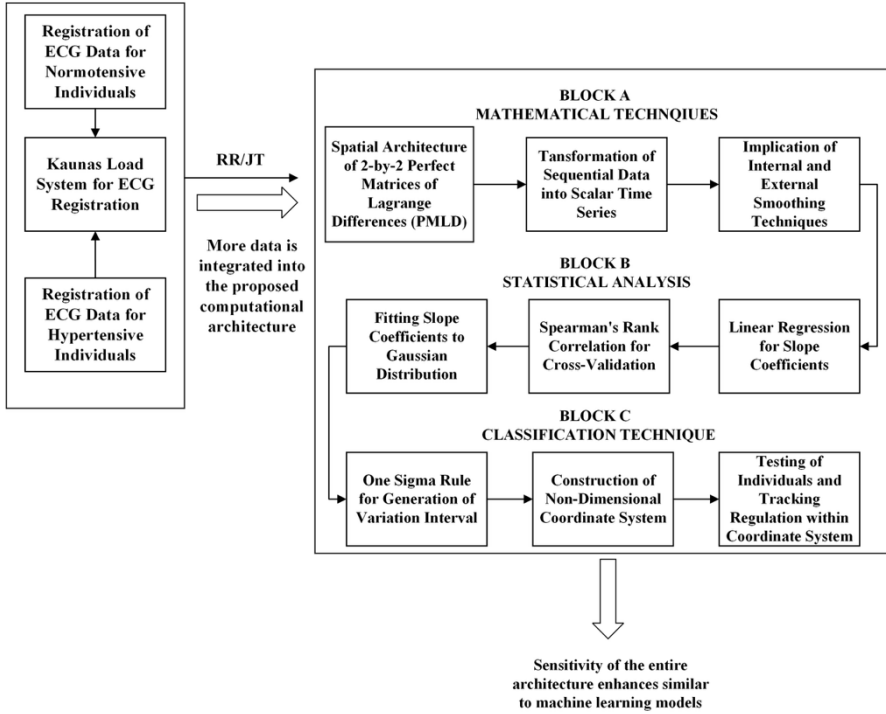


**Fig. 5.** Structure of the Computation Setup

### The Spatial Architecture of 2-by-2 Perfect Matrices of Lagrange Differences

The RR inter-beat interval and the duration of the JT wave are recorded as time series:  $x = (x_1, x_2, \dots, x_n)$  and  $y = (y_1, y_2, \dots, y_n)$ , where  $n$  is the number of recorded heartbeats observed during the stress test. The construction criteria for a square perfect matrix of Lagrange differences (PMLD) are well explained in [13, 49, 74]. The representation of the second-order PMLD reads:

$$L_{\delta,k}^{(1)} = \begin{bmatrix} x_k & x_{k+\delta} - y_{k+\delta} \\ x_{k-\delta} - y_{k-\delta} & y_k \end{bmatrix} [13, 49].$$

The two time series undergo transformation into a set of trajectory matrices, represented as  $L_{\delta,k}^{(\beta)}$ ,  $k = (1 + \delta, 2 + \delta, \dots, n - \delta)$ ;  $\beta \in \{1, 2, \dots, 18\}$ , as adopted from [13].

### Transformation of Sequential Data into the Scalar Time Series

It is important to transform the trajectory matrices  $L_{\delta,k}^{(\beta)}$  into a unified scalar time series. To achieve this, a mapping function is used:  $\mathcal{F}: \mathbb{R}^{2 \times 2} \rightarrow \mathbb{R}^1$ . In this study, the chosen mapping function  $\mathcal{F}$  is the discriminant of the matrix  $L_{\delta,k}^{(\beta)}$ :  $\mathcal{F}(L_{\delta,k}^{(\beta)}) = \text{disc}(L_{\delta,k}^{(\beta)}) = (a_{11} - a_{22})^2 + 4a_{12}a_{21}$ , where indexes denote the coordinates of elements in the matrix  $L_{\delta,k}^{(\beta)}$  [49].

### Implication of Internal and External Smoothing Techniques

Smoothing techniques are important for reducing potential noise effects in the scalar sequence  $\mathcal{F}(L_{\delta,k}^{(\beta)})$ . Therefore, if the radius of internal smoothing is denoted by  $R_i$  and the radius of external smoothing is denoted by  $R_e$ , then the smoothed sequence depicting the algebraic relationship between the two time series  $x$  and  $y$  is defined as:  $s_k(R_i, R_e, \beta) = \frac{1}{R_i(2R_e+1)} \sum_{j=k-R_e}^{k+R_e} \sum_{\delta=1}^{R_i} \mathcal{F}(L_{\delta,k}^{(\beta)})$ , where  $k = (1 + R_i + R_e), (2 + R_i + R_e), \dots, (n - R_i - R_e)$ . Building on the smoothing technique described in [13], fixed smoothing parameters  $R_i = 3$ ,  $R_e = 4$  and  $\beta = 1$  are also adopted in this study. This means that all computations are based on the following smoothing configuration  $s_k(3, 4, 1)$  [13]. Following these steps, a meaningful algebraic relationship between the RR/JT is attained, which is averaged per minute for the entire cohort. The algebraic relationship signifies the activity of heart rate during the stress test. In addition, systolic and diastolic arterial blood pressure are measured every minute indicating blood pressure regulation during physical exercise.

### Slope Coefficients Analysis of the Load and Recovery Phases

As mentioned, the stress test consists of the load phase and the recovery phase. Both phases contain crucial information about the cardiovascular behaviour during the exercise [49, 129]. While both phases provide meaningful analytical insights into the behaviour of the cardiovascular system during the stress test, special attention is focused on the load phase of the stress test in this work. Therefore, to extract useful information from the load phase, the relative changes in ABP and HR are computed and averaged per minute. To do so, first, the difference between the systolic and diastolic blood pressure is computed, dividing it by the systolic blood pressure as follows:  $(S - D)/S$ ; this ratio provides a relative change in blood pressure. Additionally, the RR inter-beat interval and the duration of the JT wave are first fitted into the second-order matrix architecture of the PMLD. The transformation of the matrix into a scalar time series is performed using discriminant analysis:  $\text{disc}(\text{RR}/\text{JT})$ . Then, a scatter plot is generated with  $(S - D)/S$  on the x-axis and  $\text{disc}(\text{RR}/\text{JT})$  on the y-axis. The scatter plot of the load phase is depicted in red, whereas that of the recovery phase is visualised in blue. The data points attained in

the phase plots are fitted through a trend line. The slope coefficients for the healthy class are labelled as  $H_{CL}$  for the load phase and  $H_{CR}$  for the recovery phase, whereas for the unhealthy cohort, they are labelled as  $U_{CL}$  and  $U_{CR}$  (see Table 2 and Table 3). The entire computational algorithm helps to visualise and comprehend the relative variations of HR and ABP regulation occurring during the load and recovery phases of the stress test. As mentioned already, special attention is focused on the load phase of the stress test.

### Spearman's Rank Correlation Coefficients

The Spearman's rank correlation coefficients are also computed during the load and recovery phases of the stress test. These coefficients serve to cross-validate the outcomes obtained in the previous steps by providing a quantitative analysis of the relative changes occurring between the HR and ABP regulation during the load and recovery phases of the stress test. The resulting correlation values are denoted as  $H_{SL}$ ,  $H_{SR}$ ,  $U_{SL}$ , and  $U_{SR}$ , representing the correlation coefficients specific to the load and recovery phases for both healthy and unhealthy cohorts (see Table 2 and Table 3). This step helps to collect the sufficient analytical information necessary for generating the classification and decision support system, which are explained in the following paragraph.

**Table 2.** Slope Coefficients and Spearman's Rank Correlation Coefficients for Healthy Individuals during Load and Recovery Phases

Candidates, $H_n$	Load phase Slope Coefficients, $H_{CL}$	Load phase Spearman's Rank Correlation coefficients, $H_{SL}$	Recovery phase Slope Coefficients, $H_{CR}$	Recovery phase Spearman's Rank Correlation coefficients, $H_{SR}$
$H_1$	-1.696	-0.804	-0.322	-0.802
$H_2$	-0.658	-0.906	-0.013	-0.049
$H_3$	-1.655	-0.933	-0.302	-0.467
$H_4$	-1.052	-0.816	-0.199	-0.839
$H_5$	-1.003	-0.890	-0.909	-0.924
$H_6$	-0.097	-0.217	-0.254	-0.815
$H_7$	-1.654	-0.891	-0.947	-0.754
$H_8$	-1.182	-0.839	-0.355	-0.802
$H_9$	-0.885	-0.952	-0.169	-0.807
$H_{10}$	-0.4209	-0.650	-0.3161	-0.400

**Table 3.** Slope Coefficients and Spearman's Rank Correlation Coefficients for Unhealthy Individuals during Load and Recovery Phases

Candidates, $U_n$	Load phase Slope Coefficients, $U_{CL}$	Load phase Spearman's Rank Correlation coefficients, $U_{SL}$	Recovery phase Slope Coefficients, $U_{CR}$	Recovery phase Spearman's Rank Correlation coefficients, $U_{SR}$
$U_1$	-2.328	-0.696	-0.616	-0.912
$U_2$	-2.229	-0.797	-0.661	-0.962
$U_3$	-2.180	-0.475	-0.433	-0.687
$U_4$	-2.254	-0.600	-0.3231	-0.400
$U_5$	-1.490	-0.970	-0.480	-0.916
$U_6$	-1.684	-0.907	-0.748	-0.976
$U_7$	-2.396	-0.865	-0.152	-0.783
$U_8$	-0.483	-0.610	-0.139	-0.826
$U_9$	-0.973	-0.495	-0.141	-0.750
$U_{10}$	-0.803	-0.874	-0.384	-0.807
$U_{11}$	-2.071	-0.945	-0.636	-0.922

#### Fitting Slope Coefficients to the Gaussian Distribution

In this statistical step, the slope coefficients  $H_{CL}$ ,  $H_{CR}$ ,  $U_{CL}$ , and  $U_{CR}$  are fitted to the Gaussian distribution. First, the Anderson–Darling test is performed to assess whether the slope coefficient data points conform to a normal distribution. Following this, the data points are fitted to a normal distribution, and the resulting parameters are encapsulated in a probability distribution function. Important parameters, such as the means ( $\mu_{HL}$ ,  $\mu_{UL}$ ) and standard deviations ( $\sigma_{HL}$ ,  $\sigma_{UL}$ ) of the healthy and unhealthy cohorts, are then retrieved from this probability distribution function. Additionally, the probability density function is computed for the entire cohort during the load and recovery phases. The distribution of points during the load phase is shown in red, and for the recovery phase, these points are shown in blue. This distribution analysis helps to understand the quantitative significance of the load phase for both healthy and unhealthy groups (see Fig. 8). The significance of the load phase is determined by a simple statistical condition:  $|\mu_{UL} - \mu_{HL}| \geq \min(\sigma_{HL}, \sigma_{UL})$ . If this condition is met, the meaningfulness of the load phase is obvious (see Table 4).

**Table 4.** Statistical Conditions for Discerning Significance in Different Phases of the Stress Test

Mean ( $\mu$ )	Std. Deviation ( $\sigma$ )	Sig. level	Difference in means	The statistical condition
$\mu_{H_L} = -1.0982$	$\sigma_{H_L} = 0.5287$	0.4634	$ \mu_{U_L} - \mu_{H_L} $ $=  -1.6636 - (-1.0982) $ $= 0.5654$	$ \mu_{U_L} - \mu_{H_L}  \geq \min(\sigma_{H_L}, \sigma_{U_L})$ Condition is satisfied
$\mu_{U_L} = -1.6636$	$\sigma_{U_L} = 0.6970$	0.1789		
$\mu_{H_R} = -0.3855$	$\sigma_{H_R} = 0.3239$	0.0190	$ \sigma_{U_R} - \sigma_{H_R} $ $=  -0.4391 - (-0.3855) $ $= 0.0536$	$ \mu_{U_R} - \mu_{H_R}  \geq \min(\sigma_{H_R}, \sigma_{U_R})$ Condition is not satisfied
$\mu_{U_R} = -0.4391$	$\sigma_{U_R} = 0.2311$	0.2339		

### Classification Technique

The following discussion presents a three-step statistical approach to generate the variation interval, a non-dimensional coordinate system, and, finally, a decision support system for testing the candidate(s) in the three-dimensional coordinate system to determine the regulation path.

#### One Sigma Rule for the Generation of the Variation Interval

As already mentioned, the significance of the load phase is checked by the condition outlined in Table 4. Thus, based on the data points obtained for the load phase in both groups, the variation interval is then formed. First, the central tendency of the normally distributed data is visualised by drawing a solid vertical line for the healthy data (depicted in green) and unhealthy data (visualised in magenta). Next, vertically dashed lines are drawn one standard deviation below and above the mean. Finally, the upper and lower limits of the variation interval are determined by following a straightforward statistical approach. The upper limit is calculated as the mean plus one standard deviation, and the lower limit is the mean minus one standard deviation. Mathematically, these are expressed as  $\mu_{H_L} + \sigma_{H_L}$  and  $\mu_{U_L} - \sigma_{U_L}$ . These rules are applied to both healthy and unhealthy cohorts. The variation interval is represented as an arrow connecting the upper and lower limits. It serves a classification purpose: test candidates falling closer to the lower bound are identified as healthy, while those near the upper limit are classified as unhealthy. The symbolic representation is shown using an asterisk sign (refer to Fig. 9c and Fig. 10c).

#### Construction of the Non-dimensional Coordinate System

A three-point, non-dimensional coordinate system is constructed (see Fig. 9d and Fig. 10d) that mirrors the visual representation of the three systems, as shown in Fig. 4. The objective is to show the path of regulation trajectory traversed by the test candidate(s) after classification. The coordinates  $(-1, 0)$ ,  $(0, 1)$ , and  $(1, 0)$  signify the Executive, Regulatory, and Supply systems, respectively.

### Testing of Individuals and Tracking the Regulation Path

If  $T$  represents the test candidate, then three sets of conditions are defined: (1)  $T \leq (\mu_{U_L} - \sigma_{U_L})$ ; (2)  $T \geq (\mu_{H_L} + \sigma_{H_L})$ ; and (3)  $(\mu_{U_L} - \sigma_{U_L}) < T < (\mu_{H_L} + \sigma_{H_L})$ . Depending on the value of  $T$ , one of these three conditions must be satisfied and should adhere to the interpolation coefficient ( $I$ ) of either  $-1$ ,  $1$  or a value calculated according to the following formula:  $2 \frac{T - (\mu_{U_L} - \sigma_{U_L})}{(\mu_{H_L} + \sigma_{H_L}) - (\mu_{U_L} - \sigma_{U_L})} - 1$ . These steps enable the classification of the candidate(s) within the coordinate system. The final step is to traverse the regulation path followed by the test candidate. This is performed by making the thickness of the path which is followed by the test candidates. Accordingly, one of three conditions must be met by the test candidate. If the candidate follows the left path, then the thickness of the left branch is calculated as  $10 - \frac{I+1}{2} \times 9$ . For the right branch, the thickness is  $\frac{I+1}{2} \times 9 + 1$ . Otherwise, the thickness is calculated as:  $2 \frac{T - (\mu_{U_L} - \sigma_{U_L})}{(\mu_{H_L} + \sigma_{H_L}) - (\mu_{U_L} - \sigma_{U_L})} \times 9$  (see Table 5).

**Table 5.** Triangular System Inclusion Criteria for the Slope Coefficient of the New Candidate

	Condition 1	Condition 2	Condition 3
If	$T \leq (\mu_{U_L} - \sigma_{U_L})$	$T \geq (\mu_{H_L} + \sigma_{H_L})$	$(\mu_{U_L} - \sigma_{U_L}) < T < (\mu_{H_L} + \sigma_{H_L})$
Then, Interpolation coefficient	$I = -1$	$I = 1$	$I = 2 \frac{T - (\mu_{U_L} - \sigma_{U_L})}{(\mu_{H_L} + \sigma_{H_L}) - (\mu_{U_L} - \sigma_{U_L})} - 1$
The thickness of the left branch in pixels	$Thickness_{Left} = 10 - \frac{I + 1}{2} \times 9$	1	$2 \frac{T - (\mu_{U_L} - \sigma_{U_L})}{(\mu_{H_L} + \sigma_{H_L}) - (\mu_{U_L} - \sigma_{U_L})} \times 9$
The thickness of the right branch in pixels	1	$Thickness_{Right} = \frac{I + 1}{2} \times 9 + 1$	

### Experimental Results for the Healthy and Unhealthy Cohort

The RR interval and the JT wave of ten healthy and eleven unhealthy individuals are separately analysed using the PMLD architecture. The resulting sequential data for each of the twenty-one candidates is translated into a scalar time series, and smoothing techniques are applied. As a result of these mathematical techniques, meaningful algebraic relationships are derived for heart rate dynamics versus time and systolic–diastolic arterial blood pressure regulation versus time. The slope coefficient

data points are also fitted to a trendline. As an example, one individual from the healthy cohort  $H_{10}$  and one from an unhealthy cohort  $U_4$  are visualised in Fig. 6 and Fig. 7. In Fig. 6a, the algebraic relationship between the RR/JT is plotted against time (minutes) on the x-axis and the discriminant (RR/JT) on the y-axis. The load phase is shown in red, whereas the recovery phase is shown in blue, and the separation of the two phases is highlighted by a vertical dashed line. Fig. 6b shows the stepwise arterial blood pressure (ABP) reading averaged per minute, with time on the x-axis and ABP in mm/Hg on the y-axis. Fig. 6c shows the relative changes in the ABP and the discriminant of RR/JT as a phase plot, with the data points connected by a trendline. The slope coefficient values during the load and recovery phases are  $-0.420$  and  $-0.3160$ , respectively, as shown in Table 2 and Fig. 6d.

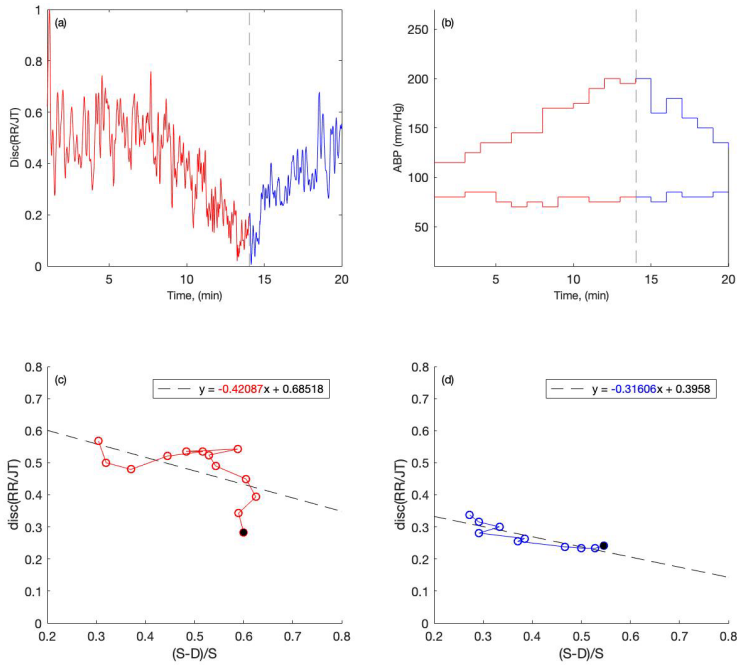


**Fig. 6.** Cardiovascular Dynamics of Healthy Individual  $H_{10}$ : (a) RR Interval and JT Wave Dynamics, (b) Arterial Blood Pressure Regulation, (c, d) ABP and Heart Rate Phase Relationship

Fig. 7 depicts the dynamics of the heart rate and blood pressure regulation for one of the unhealthy individuals,  $U_{11}$ . Fig. 7a shows the algebraic relationship of cardiovascular dynamics by taking the discriminant of RR/JT on the y-axis and time in minutes on the x-axis. Fig. 7b exhibits the relative changes occurring in the ABP during the physical exercise. The phase plot representation of the slope coefficients during both phases is shown in Fig. 7(c, d). The same mathematical approach is applied to all other candidates in the cohort, and the values are presented in Table 2 and Table 3. The smallest slope coefficient value for the healthy cohort during the load

phase is observed to be  $-0.097$ , whereas for the unhealthy cohort, it is  $-2.396$ . By inspecting the load and recovery phase plot for both healthy and unhealthy cohorts, and also from the slope coefficient values, it can be inferred that although there are observable variations in the heart rate and the blood pressure regulation during the stress test, closer inspection reveals that the load phase variability is more pronounced in terms of providing information than the recovery phase.

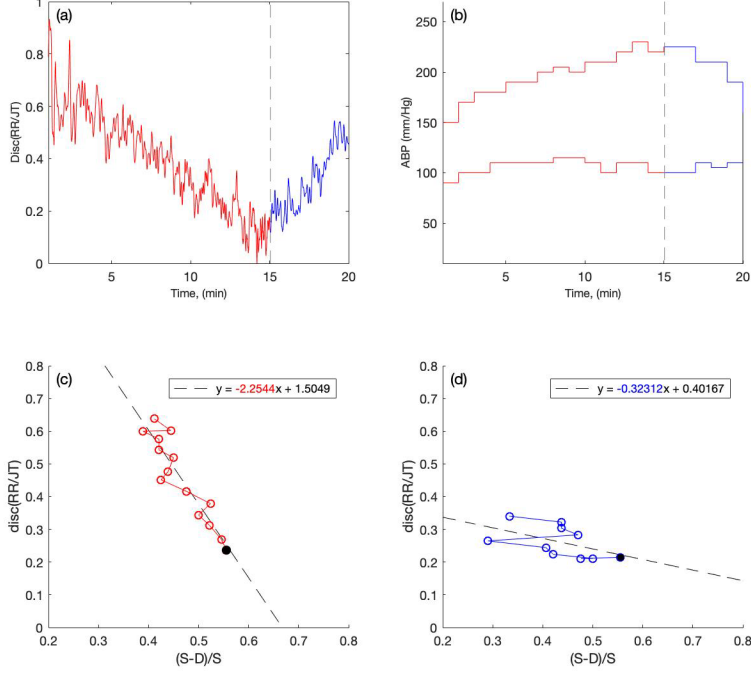


**Fig. 7.** Cardiovascular Dynamics of Unhealthy Individual  $U_4$ : (a) RR Interval and JT Wave, (b) ABP Regulation, (c, d) ABP and Heart Rate Phase Relationship

The coefficient values obtained for the load and recovery phases are fitted to a Gaussian distribution for both healthy and unhealthy individuals, as shown in Fig. 8. In Fig. 8a, the x-axis represents the distribution of data points for the entire cohort, while the y-axis shows the probability density curve. The curve represented in green indicates the data distribution for the healthy cohort, whereas magenta represents the data distribution for the unhealthy cohort. Fig. 8b shows the data distribution for the entire cohort during the recovery phase. The focus is placed solely on the distribution of data during the load phase. In Fig. 8a, the application of one sigma rule helps to generate the variation interval, which is highlighted by an arrow linking the upper and lower bounds:  $\mu_{HL} + \sigma_{HL}$  and  $\mu_{UL} - \sigma_{UL}$ . The variation interval serves the straightforward purpose of classifying new candidate(s). For instance, if an individual entering this interval falls towards the lower limit, they are identified as healthy; if an individual is situated towards the upper limit, they are classified as unhealthy.

Following the criterion for the generation of the three-point non-dimensional coordinate system, as explained in previous steps, a triangle is constructed that mirrors



the architecture of Fig. 4. The thickness of the triangle's connection is an indication (also referred to as a health biomarker) used for identifying the regulation path, which is traversed by the new incoming candidate(s). In this regard, two test candidates are fed into the entire computation routine, whose descriptions are as follows:

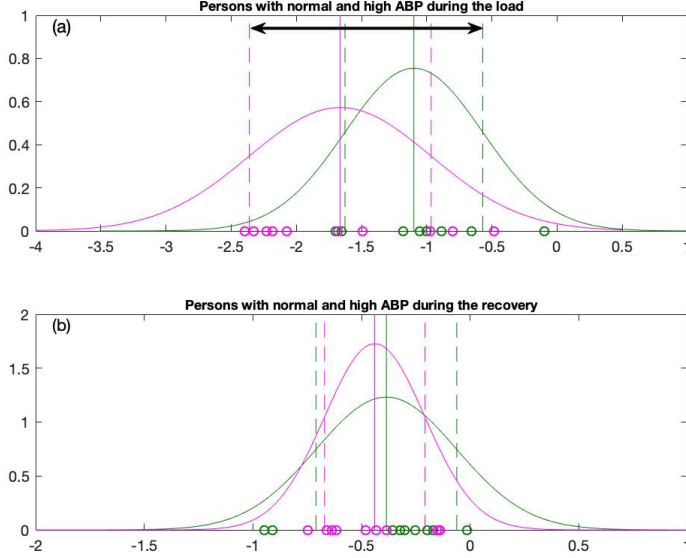


**Fig. 8.** Gaussian Distribution Curves: (a) Load Phase Slope Coefficients for Healthy (green) vs. Unhealthy (magenta) Individuals; (b) Recovery Phase Slope Coefficients for the Same Groups

### Experimental Results for Test Candidate 1

In Fig. 9, an in-depth analysis of a test candidate is presented. The RR interval and the duration of the JT wave are derived from the individual's ECG and subjected to a mathematical and computational routine. Fig. 9a represents the changes in the heart rate and ABP with respect to time. The ABP reading of the candidate classifies him as a person with normal ABP. In Fig. 9b, the slope coefficient obtained during the load phase is  $-1.988$ . If an inspection of the slope coefficient value is made and compared to the closer proximity of the values in Table 2 and Table 3, the value is close to those of the unhealthy cohort. In Fig. 9c, the classification interval places the individual into the lower bound of the interval and classifies him as belonging to the unhealthy category. Further computations are performed, and this slope coefficient value is passed through the statistical routine, where three sets of conditions are checked: (1)  $T \leq (\mu_{U_L} - \sigma_{U_L})$ ; (2)  $T \geq (\mu_{H_L} + \sigma_{H_L})$ , and  $(\mu_{U_L} - \sigma_{U_L}) < T < (\mu_{H_L} + \sigma_{H_L})$ . In this case, the third condition is fulfilled, and the interpolation coefficient value generated is  $-0.585$ . Finally, these interpolation coefficient values produce a right-side width of the triangle of three units and a left-side width of eight units—indicating that blood pressure regulation is more pronounced than heart rate changes during the load phase. This suggests that, despite a seemingly healthy ABP reading at rest, the cardiovascular system struggles under high loads. While the

individual's blood pressure appears normal under resting conditions, the application of the stress test reveals subtle relative variations through the mathematical techniques proposed in this study.

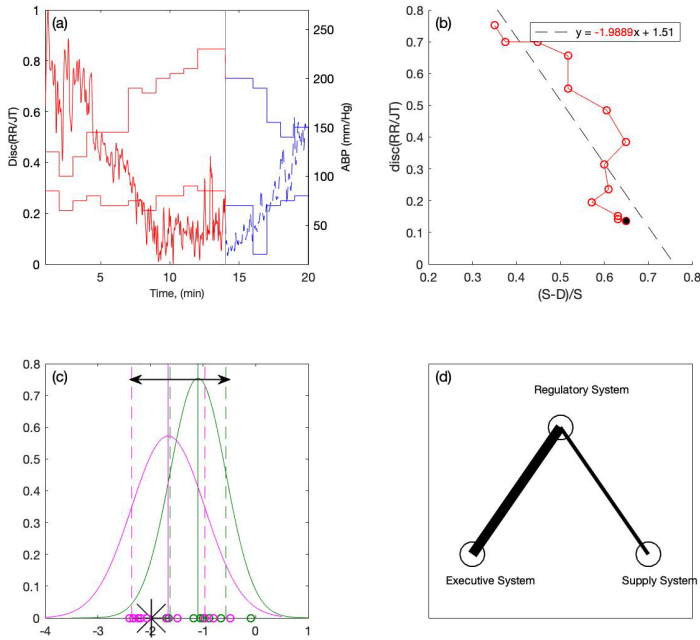


**Fig. 9.** Test Candidate 1 Analysis: (a) Heart Rate and ABP Variations, (b) Relative Changes During Load Phase, (c) Candidate's Position in Variation Interval, (d) Blood Pressure Regulation Trajectory

### Experimental Results for Test Candidate 2

In Fig. 10a, another test candidate is evaluated in terms of heart rate and blood pressure dynamics during the stress test. The ECG parameters (RR interval and JT wave) are passed through the entire computational routine, and the graphs are plotted with respect to time. Similarly, the ABP reading is plotted within the same frame (see Fig. 10b). The ABP readings classify the individual as hypertensive (130/85 mmHg). The next step is to evaluate the data points through the statistical routine. A slope coefficient value of  $-0.1456$  is obtained. The phase plane representation of the relative changes in heart rate and ABP is visualised in Fig. 10b. The variation interval classifies the person into the category of healthy individuals, as marked by the asterisk sign in Fig. 10c. Finally, the three-point coordinate system indicates that the regulation path followed by the person is expressed by the relative changes occurring in the heart rate (see Fig. 10d). Despite the initial indication of hypertensive behaviour in the blood pressure readings, this individual demonstrates a better capacity to endure load compared to the previous candidate.

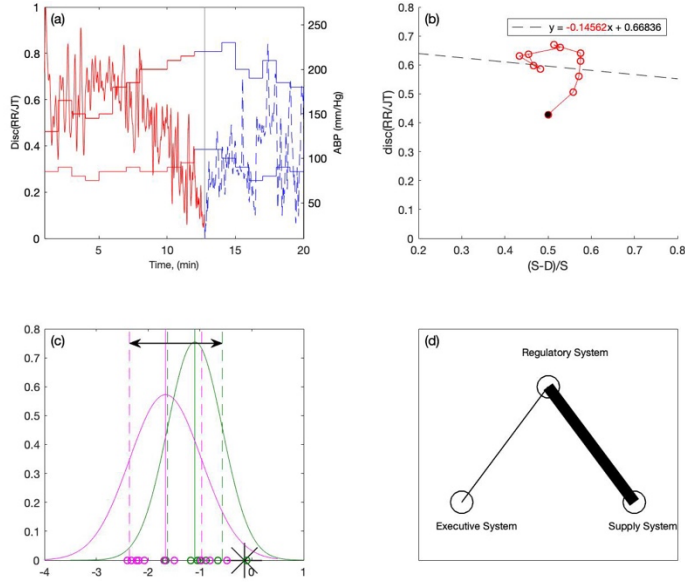


**Fig. 10.** Test Candidate 2 Analysis: (a) Heart Rate and ABP Variations, (b) Relative Changes During Load Phase, (c) Candidate's Position in Variation Interval, (d) Blood Pressure Regulation Trajectory

### Conclusive Insights from the Study

The overall findings of the study can be summarised in a few points. First, the implementation of perfect matrices of Lagrange differences helps to identify and understand the relative and subtle changes in HR and ABP regulation during the stress test. The collapse of complexity is observable during the load phase of the stress test for the entire cohort. The implementation of statistical analysis further aids in generating the classification interval and the decision support system, which resembles a machine-trained model whose performance is entirely dependent on the input. In other words, the more input that is added, the better performance yielded by the decision support system in classifying individual(s). The practical significance of understanding relative variations in heart rate and blood pressure lies in its ability to reveal an individual's cardiovascular capacity to handle loads during physical activity, which has diagnostics value. Despite the modest data size, the proposed matrix-based algorithm helps to retrieve useful information from cardiac intervals for diagnostic purposes.

### 3.2 Matrix-Based Algorithm for Complexity Collapse and Cardiovascular Self-Organisation during the Stress Test (the Load and Recovery Phases)

The concepts of “collapse of complexity” (occurring at the end of the load phase), “self-organisation of the cardiovascular system” (observed during both the load and recovery phases), and the “velocity of adaptation index” (indicating recovery after the exercise) are pivotal in comprehending the complex processes within the cardiovascular system during the physical exercise. These concepts elucidate the state

and dynamic responses of the cardiovascular system and have diagnostic value. The previous section extensively examined the load phase of the stress test to understand the complexity of cardiovascular collapse during the physical exercise. While the load phase was thoroughly analysed for the relationships between ECG parameters, it is equally important to focus on the recovery phase of the stress test. As stated in several research studies, the initial minutes of the recovery phase hold significant diagnostic value [130-133]. Other studies [129, 134] have also emphasised the importance of the recovery phase when examining the velocity of adaptation index in athletes and women during the exercise, highlighting the analysis of parameters such as the RR interval and the duration of the JT wave. The recovery phase reflects how efficiently the cardiovascular system returns to its resting state after the exercise, underscoring its importance in assessing the recovery efficiency of the cardiovascular system [135].

This section of the study aims to achieve the following five major objectives: (1) to propose a second-order PMLD matrix-based algorithm based on time-delayed patterns for analysing the RR inter-beat interval and the JT wave to evaluate the collapse of complexity and the self-organisation of the cardiovascular system during the stress test; (2) to compute the velocity of adaptation (during the entire duration of the stress test) and the newly proposed modified velocity of adaptation index (during the recovery phase of the stress test); (3) to generate the first health indicator, alpha, based on the velocity of adaptation and the newly formulated velocity of adaptation index; (4) to generate the second health indicator, beta, using a series of mathematical steps based on the mean values of wavelet coefficients approximated by a second-order polynomial; (5) to develop a decision support system for classifying individuals based on the two health indicators, alpha and beta. The proposed algorithm can be used in clinics for diagnostic purposes.

It is noteworthy that this section continues from the previous one, but it focuses on different algorithms and statistical methodologies. However, it maintains consistency in the study cohort, bioethical considerations, and stress test protocols, as outlined earlier. Therefore, all previously described experimental protocols also apply to this section.

### **Experimental Results of the Study**

The experiment of this study was conducted on four healthy subjects and four unhealthy subjects (Table 2). The various steps of the proposed algorithm are explained in detail below.

#### **Data Preprocessing, Normalisation, Difference Signal, and the Velocity of the Adaption Index**

In the data preprocessing step, the time series  $x$  and  $y$  are first processed using a signal denoising technique to filter out noise while preserving the essential features of the time series. To achieve this, the variational mode decomposition (VMD) technique is used to decompose the original signal into  $n$  predetermined intrinsic mode functions (IMFs). Then, for each decomposed signal mode, the correlation coefficient is calculated with the original time series to single out noise and the original time series based on predetermined threshold values. The retrieved signal

modes are further processed through wavelet denoising, where the denoising level maintains a balance between noise and significant signal modes. These denoising techniques are also used in [136, 137]. Additionally, the time series are normalised using a simple normalisation approach:  $x_k/x_{max}$  and  $y_k/y_{max}$ , where  $x_k$  and  $y_k$  stand for the RR inter-beat interval and the JT wave, and  $x_{max}$  and  $y_{max}$  represent the maximal durations of those intervals during the stress test ( $k = 1, 2, 3, \dots$ ). This normalisation approach is also used in [107]. The presented techniques ensure that the time series contains only useful information for further computations.

Following normalisation, the difference between the time series  $x$  and  $y$  is computed. One of the hypotheses of this work is that the resulting time series from the difference signal may provide more information about the complex dynamics of the cardiovascular system during the stress test. The resulting variations of the difference signal are comparable to the wavelet analysis of the two time series, which is executed in the subsequent parts.

Another important feature of this study is the velocity of the adaptation index, calculated as  $A_d = \frac{1}{n} \sum_{i=1}^n (J^T i / J^T_{max} - R^R i / R^R_{max}) \times 100$ . The formula for calculating the velocity of the adaptation index is presented and adopted from [135]. This provides analytical insights into the generation of one of the major health indicators, referred to as alpha. It is important to note that, in order to create the health indicator alpha, another essential parameter is necessary, referred to as the modified velocity of adaptation index, denoted as  $A_r$ . This value is calculated only during the recovery phase of the stress test. To calculate the modified velocity of the adaptation index, the time series RR inter-beat interval and the duration of the JT wave are first processed through the proposed time-delayed pattern algorithm. The resulting time-delayed data points are then fitted into a second-order delayed PMLD matrix architecture. To convert the sequence of matrices into a scalar time series, the discriminant of the matrix is used—a method also employed in [49]. Finally, the mean of this scalar time series is taken only during the recovery phase of the stress test, resulting in the modified velocity of the adaptation index. Special attention is given to the analysis of the recovery phase during the stress test for the generation of the health indicator alpha, as the initial minutes of the recovery phase are significant in providing diagnostic value, as highlighted in [130-133].

Another important health indicator, beta, is computed based on the means of wavelet coefficients over distinct time slots and the coefficients of a fitted second-order polynomial. It is important to note that the two health indicators are quantifying two different aspects of cardiovascular functionality during the stress test. The emphasis is especially focused on understanding cardiovascular complexity collapse and the self-organisation of the cardiovascular system. These two processes are vital concepts for comprehending the soundness of the cardiovascular system during the load phase (the end of the load termination point) and the recovery phase (the first few minutes of the recovery phase). Clearly, the overall adaptation of the cardiovascular system as a response to external loads can be navigated throughout the entire stress test activity (which could be traversed through the difference signal as well), but

special attention is focused on specific time stamps during the load and recovery phases.

The two health indicators, alpha and beta, are pivotal in assessing the functionality of the cardiovascular system. However, it is equally important to understand their combined effect, which is where the third health indicator, gamma, becomes essential. Gamma is derived from the interplay of alpha and beta, serving as a critical metric in designing a decision support system. Therefore, the two health indicators, alpha and beta, are used to generate the third indicator, gamma, which is then used to design a decision support system for classifying candidates for diagnostic purposes. As mentioned already, the experiment was performed on four healthy subjects  $H_1$ ,  $H_3$ ,  $H_6$ , and  $H_9$ , here referred to as  $H_A$ ,  $H_B$ ,  $H_C$ , and  $H_D$ , as shown in Table 6, and four unhealthy subjects  $U_2$ ,  $U_6$ ,  $U_9$ , and  $U_{11}$  (see Table 3), here referred to as  $U_A$ ,  $U_B$ ,  $U_C$ , and  $U_D$  (see Table 6). The results for each candidate are shown in one figure with subplots. The derivation of the health indicators, alpha and beta, is presented in Table 6 and Table 7, respectively. The cardiovascular collapse of complexity that occurs at the load termination point and the self-organisation of the cardiovascular system that occurs during the entire duration of the stress test are both observable for all the subjects with three different lenses. First, the variability of the difference signal can help to visualise these processes with respect to time during the load and recovery phases. Second, the effects induced by the time-delayed pattern algorithm also assist in observing the changes occurring in the cardiovascular system. Third, the wavelet analysis also helps to visualise those effects during the entire length of the stress test. To perform the wavelet analysis, a specific segmentation technique is used. This segmentation is performed on the difference signal, which is divided into three sections during the stress test (as explained in (54) and (55)). This division is structured to capture the data points in the following three phases of the stress test: the onset of load in the initial section, the termination of load in the midsection, and the recovery phase in the final section. This segmentation ensures a focused analysis of the important intervals of the stress test.

**Table 6.** Derivation of the Health Indicator Alpha for all Participants in the Study Group

Study Subjects	Values of $A_d$	Values of $A_r$	Calculation of parameter, $X = \frac{(A_d - A_r)}{A_d} * 100\%$	Health indicator alpha, $\alpha = \frac{X - \min}{\max - \min} * 100\%$
H <sub>A</sub>	14.34	12.81	10.66	56.17
H <sub>B</sub>	7.74	6.73	13.04	63.18
H <sub>C</sub>	9.71	7.23	25.54*	100
H <sub>D</sub>	15.83	17.14	-8.27	0.41
U <sub>A</sub>	4.72	4.38	7.20	45.97
U <sub>B</sub>	7.72	8.37	-8.41**	0
U <sub>C</sub>	9.9	8.38	15.35	69.98
U <sub>D</sub>	9.56	9.75	-1.98	18.93

**Table 7.** Derivation of the Health Indicator Beta for all Participants in the Study Group

P <sub>1</sub>	P <sub>2</sub>	P <sub>3</sub>	$y = mx^2 + nx + c$ , deriving $m = (P_1 + P_3)/2 - P_2$	Health indicator beta, $\beta = \frac{a - \min a}{\max a - \min a}$
0.0536	0.0252	0.0587	3.09*	100
0.0308	0.0063	0.0183	1.82	66.8
0.0302	0.0103	0.0346	2.21	77.02
0.0322	0.0159	0.0203	1.03	46.2
0.0174	0.0253	0.0183	-0.74**	0
0.0192	0.0215	0.0144	-0.47	7.04
0.0188	0.0206	0.0217	-0.03	18.5
0.0139	0.0056	0.0100	0.63	35.7

The experimental results for the healthy subject H<sub>A</sub> are presented in the subplots of Fig. 11. Subplots A and B of Fig. 11 show the original RR inter-beat interval and the duration of the JT wave in black. The denoised time series for the RR inter-beat interval and the JT wave are shown in red and blue, respectively. A vertical dashed line marks the load termination point. Subplot C of Fig. 11 shows the normalised time series for both the RR inter-beat interval and the JT wave, depicted in red and blue, respectively. The same visualisation pattern is also applied to the experimental subjects H<sub>B</sub>, H<sub>C</sub>, and H<sub>D</sub>, as shown in subplots A–C of Fig. 12, Fig. 13, and Fig. 14, respectively.

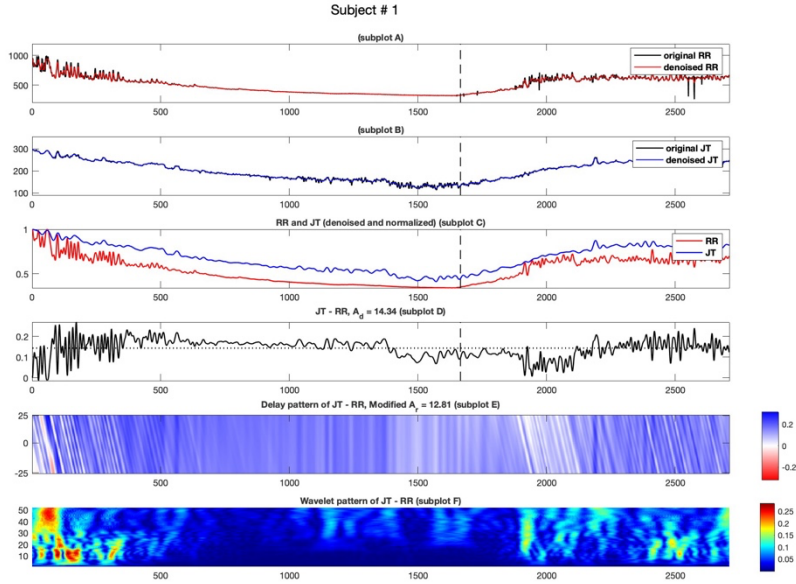


**Fig. 11.** Computational Results for Healthy Subject Denoted as H<sub>A</sub>: (Subplot A) RR Intervals, (Subplot B) JT Intervals, (Subplot C) Normalised Intervals, (Subplot D) Difference Signal and Adaptation Index, (Subplot E) Delay Pattern and Modified Index, (Subplot F) Shan Wavelet Analysis

For the healthy subject H<sub>A</sub>, as the load begins, the self-organisation of the cardiovascular system begins, which is depicted by the high variability and large amplitude of the difference signal, as seen in subplot D of Fig. 11. The high variability is evident because the cardiovascular system responds and adapts to the changes induced by the gradually increasing load. As the load continues, the variability decreases, indicating that the cardiovascular system has adapted, resulting in lower variability and a lower frequency of the difference signal. Just before the load termination point, the cardiovascular collapse of complexity is observed, where the variability of the difference signal smooths out for subjects H<sub>B</sub>, H<sub>C</sub>, and H<sub>D</sub>. During the first two minutes of the recovery phase, the self-organisation of the cardiovascular system can be observed by analysing the interplay between the normalised RR interval and the JT wave in subplot C of Fig. 11, Fig. 12, Fig. 13, and Fig. 14. In the first two minutes of the recovery phase, the amplitude of the time series for the normalised RR interval and the JT wave tends to converge for the healthy subjects H<sub>A</sub>, H<sub>B</sub>, and H<sub>D</sub>, but not for subject H<sub>C</sub>. The recovery process is longer for the subjects H<sub>A</sub>, H<sub>B</sub>, and H<sub>D</sub>, while it is shorter for H<sub>C</sub>. These observations are visually represented in subplots C and D of Fig. 11, Fig. 12, Fig. 13, and Fig. 14.



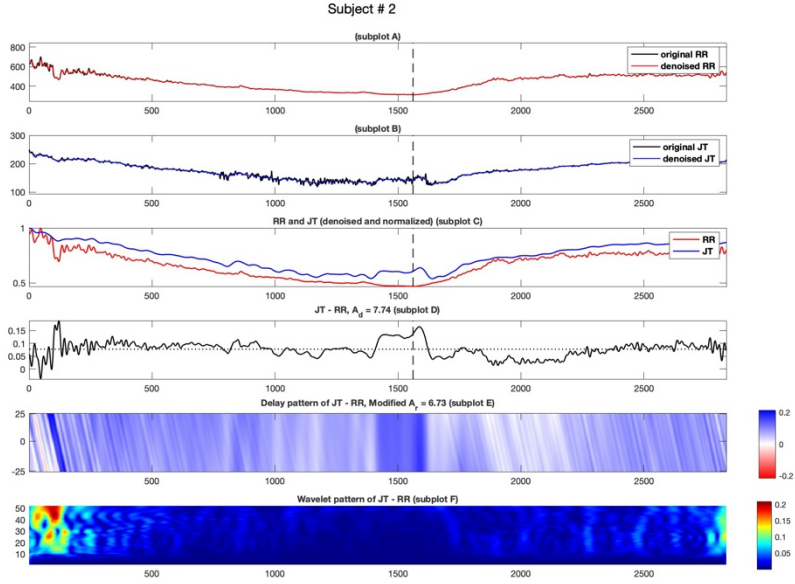


**Fig. 12.** Computational Results for Healthy Subject Denoted as  $H_B$ : (Subplot A) RR Intervals, (Subplot B) JT Intervals, (Subplot C) Normalised Intervals, (Subplot D) Difference Signal and Adaptation Index, (Subplot E) Delay Pattern and Modified Index, (Subplot F) Shan Wavelet Analysis

As we further analyse the cardiovascular system's behaviour using the proposed time-delayed pattern algorithm between the two time series (the RR inter-beat interval and the JT wave duration), another meaningful representation is observed, which is comparable to the variability seen in the difference signal (subplot C). This representation uses streaks of white, red, and blue to visualise these changes. These colours do not indicate the presence of the RR interval and the JT wave; instead, the white and red streaks reflect the same variability as is observed in the difference signal. For example, for the healthy subject  $H_A$ , as the load continues, streaks of red and white appear in the beginning, indicating the cardiovascular system's self-organisation in response to the gradually increasing physical load. This pattern is consistent among the healthy subjects  $H_B$ ,  $H_C$ , and  $H_D$  and is seen in subplot D of Fig. 12, Fig. 13, and Fig. 14. At the load termination point, the cardiovascular collapse of complexity is seen through the mix of light white and blue streaks, which are apparent for the subjects  $H_A$ ,  $H_B$ , and  $H_D$ , as seen in subplot E of Fig. 11, Fig. 12, and Fig. 14. However, for the subject  $H_C$ , a continuous hue of dark blue is observed at the load termination point, as seen in subplot E of Fig. 13. In the initial few minutes of the recovery phase, the self-organisation of the cardiovascular system is observed with light blue and white streaks visible for the candidates  $H_A$ ,  $H_B$ , and  $H_D$ , but again a dark hue of blue is seen for the healthy subject  $H_C$ . These results are also comparable to the variability of the difference signal analysed earlier.

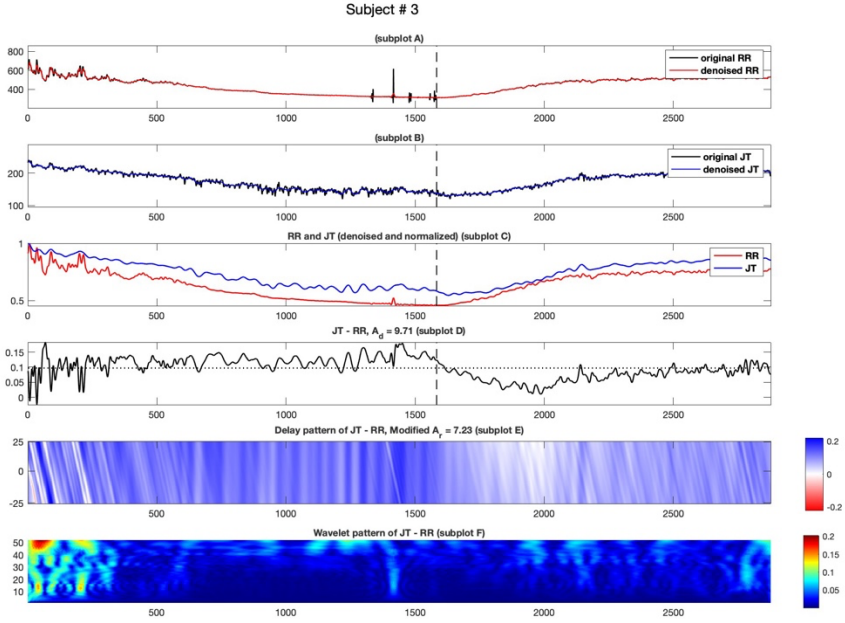


**Fig. 13.** Computational Results for Healthy Subject Denoted as  $H_C$ : (Subplot A) RR Intervals, (Subplot B) JT Intervals, (Subplot C) Normalised Intervals, (Subplot D) Difference Signal and Adaptation Index, (Subplot E) Delay Pattern and Modified Index, (Subplot F) Shan Wavelet Analysis

The velocity of the adaptation index ( $A_d$ ) is also computed for the healthy subjects throughout the entire stress test. The  $A_d$  values for these subjects are:  $H_A = 14.34$ ,  $H_B = 7.74$ ,  $H_C = 15.83$ , and  $H_D = 9.71$ . Higher  $A_d$  values indicate a more rapid and responsive adaptation of the cardiovascular system to physical activity. Among the healthy subjects,  $H_C$  has the highest responsiveness, followed by  $H_A$ ,  $H_D$ , and  $H_B$ . This can be summarised by the inequality  $H_C > H_A > H_D > H_B$ . Additionally, according to the objective of this work, the modified adaptation index  $A_r$  is also computed, yielding the following values:  $H_{\hat{A}} = 12.81$ ,  $H_{\hat{B}} = 6.73$ ,  $H_{\hat{C}} = 17.14$ , and  $H_{\hat{D}} = 7.23$ . Typically, the modified velocity of the adaptation  $A_r$  should be less than the velocity of the adaptation  $A_d$ , because  $A_d$  is measured during the entire length of the stress test, while  $A_r$  is computed only during the recovery phase. This holds true for subjects  $H_A$ ,  $H_B$ , and  $H_D$ , where  $A_d$  is greater than  $A_r$ . However, for the subject  $H_C$ ,  $A_d$  is less than  $A_r$ . All these analytical outcomes are tabulated in Table 6.

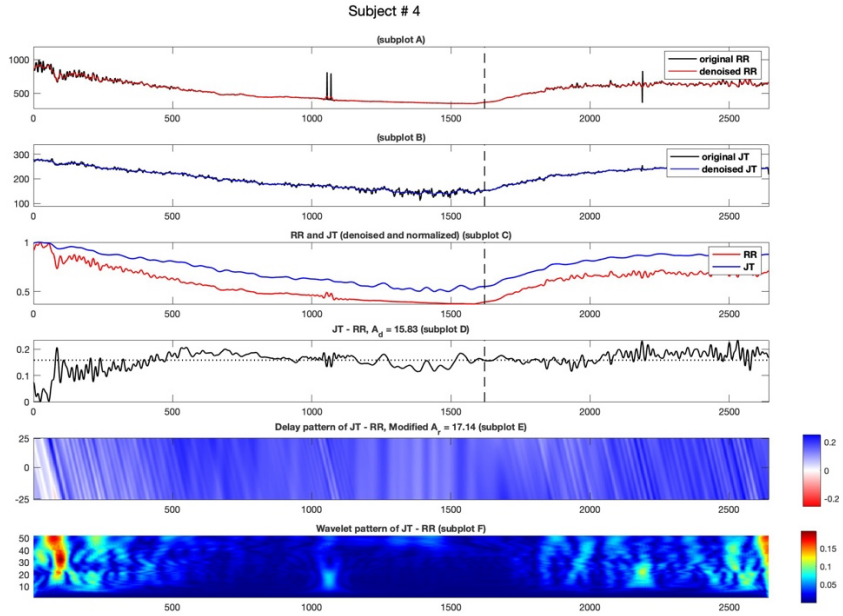


**Fig. 14.** Computational Results for Healthy Subject Denoted as  $H_D$ : (Subplot A) RR Intervals, (Subplot B) JT Intervals, (Subplot C) Normalised Intervals, (Subplot D) Difference Signal and Adaptation Index, (Subplot E) Delay Pattern and Modified Index, (Subplot F) Shan Wavelet Analysis

Another representation of the cardiovascular collapse of complexity and the self-organisation of the cardiovascular system is achieved through wavelet analysis. By examining the Shan wavelet pattern with jet colouration, variations in the time series can be observed from a frequency analysis perspective. The wavelet analysis is performed on the difference signal, which is divided into three sections corresponding to the entire length of the stress test. The first section covers the initial 900 data points, the second section also covers 900 data points, and the third section includes the remaining data points in the time series. This division is designed to capture data points at the start of the stress test, when the load begins, in the middle of the stress test, when the load is terminated, and in the final section of the stress test, when the recovery phase begins. The means of these three sections are computed and labelled as  $P_1, P_2$ , and  $P_3$ . A second-order polynomial quadratic equation is then interpolated through three points in the plane:  $(-1, P_1)$ ,  $(0, P_2)$ ,  $(1, P_3)$ . The resulting equation of the parabola is given by  $mx^2 + nx + c$ . The parameter of interest in this equation is  $m$ . As the collapse of complexity occurs at the load termination point or in the middle section, the value of the parameter  $m$  in the middle section should, therefore, be lower than in the other sections. A closer examination of the  $m$  values for the healthy subjects  $H_A, H_B, H_C$ , and  $H_D$  reveals that this hypothesis is true for all subjects (the  $m$  value is smaller in the middle section), indicating that  $m$  is an important metric for quantifying the collapse of complexity. At the beginning of the subplot F, Fig. 12, Fig. 13, and Fig. 14, streaks of light blue are visible when the load begins. The presence of these

coloured streaks is an indication of the cardiovascular system's self-organisation, and these coloured patterns are consistent for the healthy subjects  $H_A$ ,  $H_B$ ,  $H_C$ , and  $H_D$ . Also, at the beginning of the recovery phase, the self-organisation of the cardiovascular system is again observable with blue streaks for the healthy subjects  $H_A$ ,  $H_B$ , and  $H_D$ , but not for the  $H_C$  (see subplot E of Fig. 11, Fig. 12, Fig. 13, and Fig. 14). The values of  $m$  play an important role in the calculation of the health indicator beta, which is further used to generate the decision support system, as shown in Table 8.

**Table 8.** Integration of Health Indicators Alpha and Beta into the Decision Aid System Based on Gamma Values

$\alpha$	$\beta$	Evaluation of Cardiovascular Health Status: Calculation of, $\gamma = (\alpha + \beta)/2$
56.17	100	78.08
63.18	66.8	64.99
100	46.2	73.1
0.41	77.02	38.71
45.97	0	22.98
0	7.04	3.52
69.98	18.5	44.24
18.93	35.7	27.31

The complete computational process is also performed on four of the unhealthy subjects chosen from Table 2:  $U_2$ ,  $U_6$ ,  $U_9$ , and  $U_{11}$ , and hence referred to as  $U_A$ ,  $U_B$ ,  $U_C$ , and  $U_D$ . In subplot A of Fig. 15, the experimental results for the unhealthy subject  $U_A$  are depicted. The subplots (A–C) show the time series for the original RR inter-beat interval (in black); the time series for the denoised RR inter-beat interval (in red); the original and denoised time series for the duration of the JT wave (in black and blue); and the time series for the normalised RR inter-beat interval and the duration of the JT wave, respectively. Subplot D of Fig. 15 shows the time series for the difference signal (between the RR inter-beat interval and the duration of the JT wave). As the load begins, large-amplitude and high-frequency variations are observed, which are a representation of the self-organisation of the cardiovascular system in response to gradually increasing load. In subplot C of Fig. 15, at the load termination point, it is observed that the normalised RR inter-beat interval tries to converge with the normalised JT wave, which is not the case for any of the healthy subjects. It can be said that the collapse of complexity in the unhealthy subject is occurring in a different manner compared to the healthy subjects. As the recovery begins in the initial few minutes, the normalised RR inter-beat interval tries to converge to the JT wave. These effects can also be observed in, and comparable to, the time series variations of the difference signal in subplot D of Fig. 15. However, the value of  $A_d > A_r$  for the unhealthy subject  $U_A$ , as seen in Table 6. The time-delayed pattern algorithm also aids in visualising subtle changes, such as the collapse of complexity and the self-organisation of the cardiovascular system, through the streaks of red and white at the

beginning of the load phase, before load termination, and at the start of the recovery phase, as shown in subplot E of Fig. 15. Additionally, wavelet analysis offers another representation of these phenomena, as depicted in subplot F of Fig. 15. The two indicators, alpha and beta, are also computed and tabulated in Table 6 and Table 7.

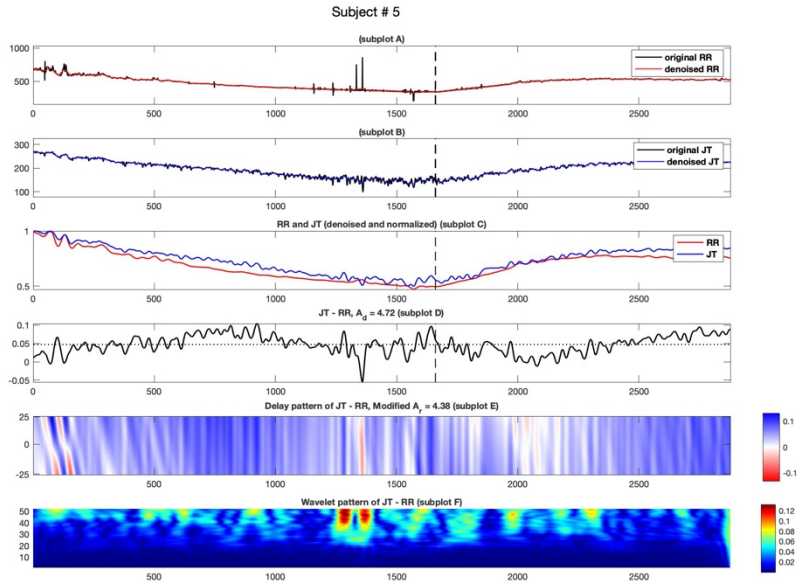


**Fig. 15.** Computational Results for Unhealthy Subject Denoted as  $U_A$ : (Subplot A) RR Intervals, (Subplot B) JT Intervals, (Subplot C) Normalised Intervals, (Subplot D) Difference Signal and Adaptation Index, (Subplot E) Delay Pattern and Modified Index, (Subplot F) Shan Wavelet Analysis

For the unhealthy subject  $U_B$ , subplots A–C in Fig. 16 depict the original, denoised and normalised RR inter-beat interval and the duration of the JT wave. In subplot D of Fig. 16, it is observed that as the load begins, the time series generated by the difference signal exhibits low amplitude and less variability. This indicates that the cardiovascular response to the gradually increasing load is not as adaptive or responsive as it was for healthy subjects  $H_A - H_D$ . Consequently, the time-delayed pattern algorithm produces fewer red and white streaks at the beginning of the load, and the wavelet analysis does not show prominent jet colouration at the start of the load phase. The self-organisation of the cardiovascular system at the beginning of the load phase shows different results compared to the unhealthy subject  $U_A$ . At the load termination point, the time series for the normalised RR inter-beat interval also converges with the JT wave, similar to the observations made for  $U_A$ . During the initial few minutes of the recovery phase, the self-organisation of the cardiovascular system is seen as the time series for the normalised RR inter-beat interval drifts away from the JT wave—behaviour again similar to that of  $U_A$ . The presence of dark jet colouration in the wavelet analysis at the load termination point is also a unique behaviour particular to the unhealthy subject  $U_B$ . All these results are seen in subplots

D–F of Fig. 16. Also, these unique behaviours tend to generate lower values of  $A_r$  as compared to  $A_d$  ( $A_d = 7.72$ ;  $A_r = 8.37$ ) and are tabulated in Table 6. The health indicators are computed in a similar manner as stated before and also tabulated in Table 6 and Table 7, respectively.

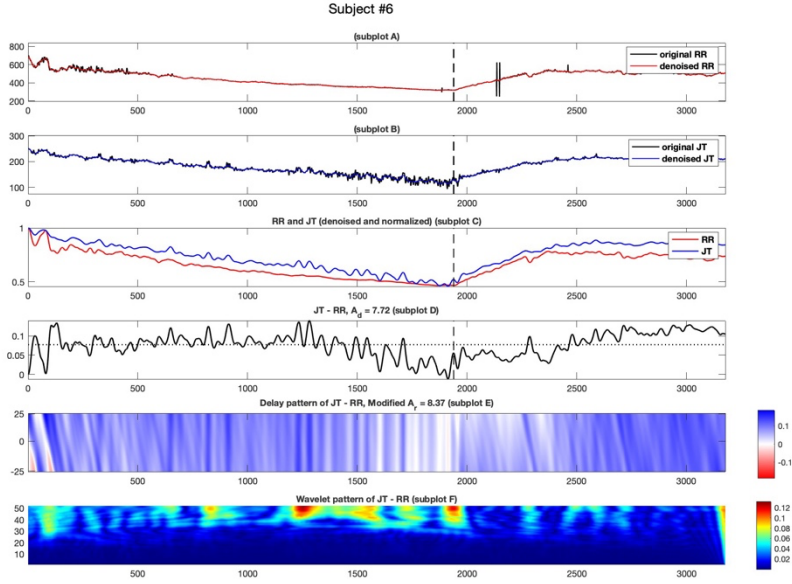


**Fig. 16.** Computational Results for Unhealthy Subject Denoted as  $U_B$ : (Subplot A) RR Intervals, (Subplot B) JT Intervals, (Subplot C) Normalised Intervals, (Subplot D) Difference Signal and Adaptation Index, (Subplot E) Delay Pattern and Modified Index, (Subplot F) Shan Wavelet Analysis

The experimental results for the unhealthy subjects  $U_C$  and  $U_D$  are shown in Fig. 17 and Fig. 18. Subplot D of Fig. 17 and Fig. 18 shows the time series for the difference signal between the RR inter-beat interval and the JT wave. At the beginning of the load phase, low-frequency and minimal variability can be observed for both candidates,  $U_C$  and  $U_D$ . For the same reason, the time-delayed pattern also generates slight streaks of red and white, as seen in subplot D of Fig. 17 and Fig. 18. This means that the self-organisation of the cardiovascular system for  $U_C$  and  $U_D$  is the least responsive and adaptive to the gradual increase in external load. At the load termination point, the normalised RR inter-beat interval and the duration of the JT wave remain apart, as seen in subplot D of Fig. 17 and Fig. 18. The collapse of complexity is rather smooth for both these candidates, unlike  $U_A$  and  $U_B$ . As recovery begins, in the initial few minutes, the time series for the normalised RR inter-beat interval and the duration of the JT wave diverge, as seen in subplot D of Fig. 17 and Fig. 18. This is again a behaviour observed particularly in the unhealthy cohort. For the same reasons, the time-delayed pattern technique produces white streaks, and the wavelet analysis produces dark jet colouration, as seen in the subplots E–F of Fig. 17 and Fig. 18. For the unhealthy subject  $U_C$ , the resulting value of  $A_d$  is greater than  $A_r$ ,



whereas, for  $U_D$ , the value of  $A_d$  is less than  $A_r$ , as seen in Table 6. The indicators alpha and beta are thus shown in Table 7.

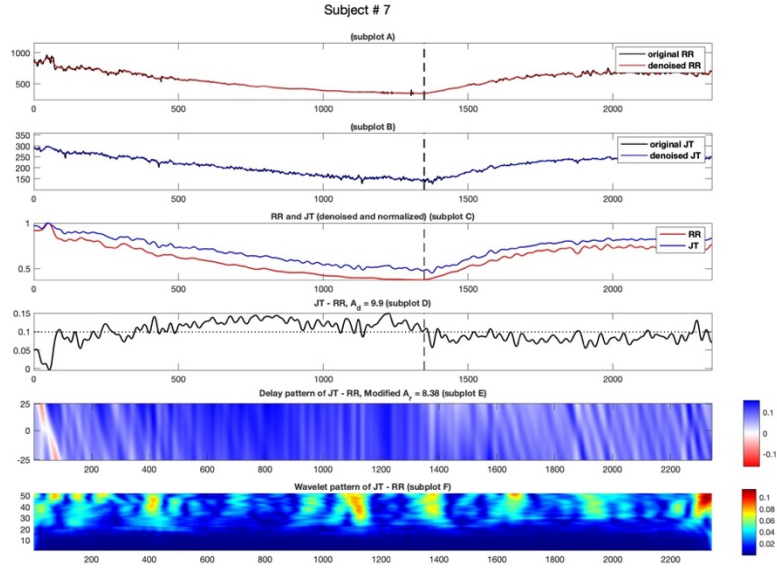


**Fig. 17.** Computational Results for Unhealthy Subject Denoted as  $U_C$ : (Subplot A) RR Intervals, (Subplot B) JT Intervals, (Subplot C) Normalised Intervals, (Subplot D) Difference Signal and Adaptation Index, (Subplot E) Delay Pattern and Modified Index, (Subplot F) Shan Wavelet Analysis

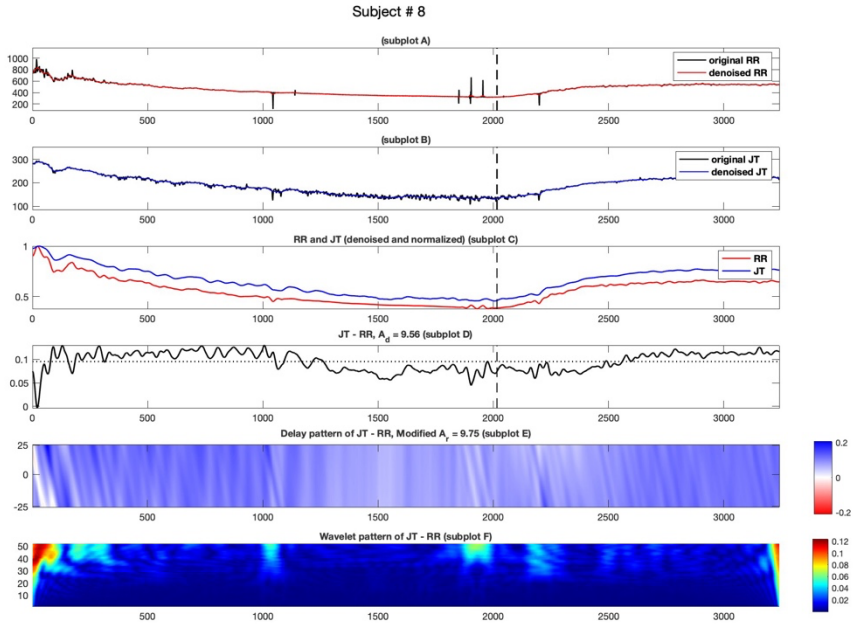


**Fig. 18.** Computational Results for Unhealthy Subject Denoted as  $U_D$ : (Subplot A) RR Intervals, (Subplot B) JT Intervals, (Subplot C) Normalised Intervals, (Subplot D) Difference Signal and Adaptation Index, (Subplot E) Delay Pattern and Modified Index, (Subplot F) Shan Wavelet Analysis

The health biomarker gamma is computed using the values of the health indicators alpha and beta, as presented in Table 13. This biomarker represents the combined effect of various aspects of the cardiovascular system, which are quantified through the alpha and beta parameters. In essence, gamma is a composite indicator derived from both alpha and beta, providing a holistic measure of cardiovascular health. By employing the semi-gauge indication tool, along with the calculated values of gamma, individuals' cardiovascular health can be categorised into three distinct statuses: healthy, moderate, and unhealthy. These classifications are based on the analysis of ECG parameters, which are processed using the computational techniques outlined in this study. For illustration, the classification of healthy and unhealthy subjects is depicted in Fig. 19 and Fig. 20. The semi-gauge indication tool, designed as described in the previous section, visually alerts individuals to their cardiovascular health status using colour codes. Specifically, a green indicator suggests that the cardiovascular system is responding well to physical load, a yellow indicator serves as a warning of potential cardiovascular concerns, and a red indicator signifies that immediate clinical attention is required.

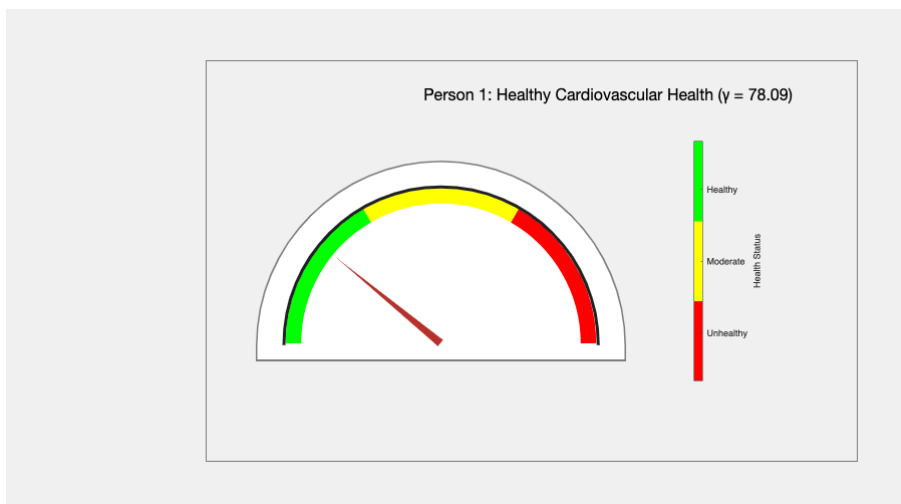


**Fig. 19.** Overall Health Status of Healthy Person ( $H_A$ ) Using Semi-Gauge Indication Tool



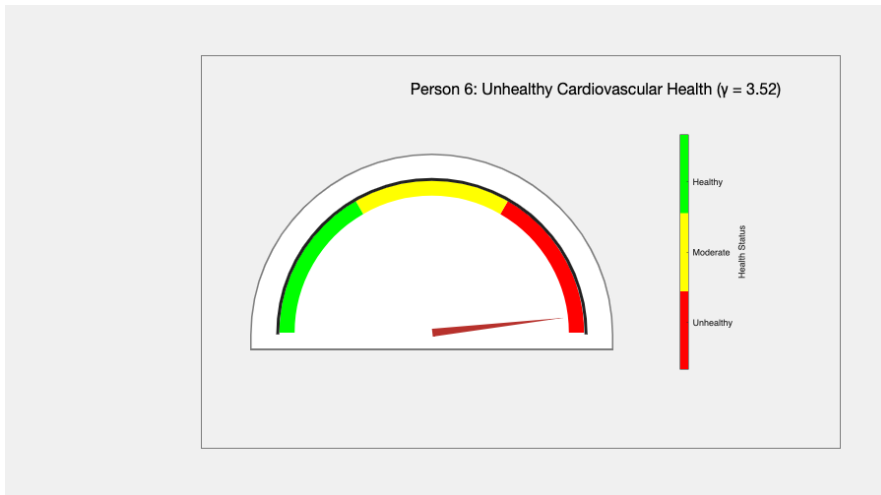


**Fig. 20.** Overall Health Status of Unhealthy Person ( $U_A$ ) Using Semi-Gauge Indication Tool

To analyse the interplay between the RR inter-beat interval and the duration of the JT wave during the stress test, particularly during the load and recovery phases, multiple techniques were proposed. The main techniques included the time-delayed pattern algorithm, the analysis of the difference signal between the two time series, and wavelet-pattern analysis. It is important to note that the collapse of complexity occurs at the load termination point for each individual, indicating either a quick adaptation to the external load, which is a healthy indication of an individual's cardiovascular response, or a slow adaptation, which suggests a less favourable cardiovascular response during the physical activity.

Similarly, the self-organisation of the cardiovascular system occurs throughout the entire length of the stress test for all individuals. However, for a better cardiovascular response to the exercise, this self-organisation should be more pronounced, indicating a healthy cardiovascular system and vice versa. Various classification techniques and state-of-the-art methods have been applied over time to analyse ECG signals (either resting ECG or during the physical exercise) for subjects with certain heart diseases. However, it is noticed that little attention has been paid to analysing the subtle changes occurring during the recovery phase of the cardiovascular system.

This study raises questions about whether these subtle variations are observable and, if so, whether it is possible to detect any unique patterns in both the healthy and unhealthy groups. These questions are addressed using state-of-the-art approaches, including the time-delayed pattern algorithm fitted into a second-order delayed PMLD matrix framework. Additionally, techniques such as wavelet analysis and the generation of health biomarkers also contribute to the findings of this study.

With the proposed technique, it was possible to identify subtle variations at different stages of the stress test and, at the same time, observe unique patterns for healthy and unhealthy subjects. The healthy group exhibited a distinctive pattern at

the beginning of the load phase (self-organisation of the cardiovascular system) and at the load termination point (collapse of complexity). The cardiovascular system's adaptation to the gradually increasing load was better in healthy subjects, as observed with the help of colour indication techniques used to visualise the outcomes produced by the time-delayed pattern algorithms and frequency analysis.

Similarly, during the initial two minutes of the recovery phase, it was observed that the RR interbeat interval tended to converge with the JT wave, a unique behaviour specific to the healthy subjects in the study. These behaviours tend to produce a greater value for the velocity of the adaptation compared to the modified velocity of the adaptation, which was consistent for all healthy subjects in the study.

For the unhealthy group, the initial adaptation of the cardiovascular system to external load varied among subjects. For half of the unhealthy subjects, the adaptation was slower, while for the others, it was similar to that of the healthy subjects. This means that the self-organisation of the cardiovascular system at the beginning of the load phase in the unhealthy group exhibited both slow and quick adaptations to the external loads.

At the load termination point, the RR inter-beat interval in half of the unhealthy subjects tended to converge with the JT wave, while in the other half, the behaviour of the two time series was similar to that observed in the healthy cohort. Similar observations were made during the initial two minutes of the recovery phase. Due to these variations, the calculated value of the velocity of adaptation was in some cases lower than the modified velocity of the adaptation, and in other cases, the opposite was true.

It is crucial to acknowledge the limitations of this study. The primary limitation is the small cohort size. Larger experimental sizes are generally encouraged to generate better and more reliable outcomes. Additionally, the absence of a female cohort is another aspect to consider for understanding cardiovascular responses not only in healthy and unhealthy groups but also among male and female participants.

Despite these limitations, the analytical capabilities of the proposed time-delayed pattern technique are noteworthy. The outcomes of the study have demonstrated that the proposed algorithm is sufficiently capable of analysing and evaluating the ECG parameters, providing reliable results. Therefore, it can be confidently stated that, although the study's small data size is a limitation, the analytical power of the proposed techniques has mitigated this constraint. Nonetheless, a key objective for future research is to increase the sample size and further assess the analytical power of the proposed matrix-based algorithm. It is also important to emphasise the uniqueness of this proposed work. This uniqueness is evident in the ability of the proposed algorithm to function effectively with a small dataset, making it incomparable to other state-of-the-art mathematical algorithmic methods.

### **Conclusive Insights from the Study**

The study analyses the relative changes between the RR inter-beat interval and the duration of the JT wave during the stress test, focusing on the following: the self-organisation of the cardiovascular system (which occurs throughout the stress test),

the collapse of complexity (which occurs at the end of the load phase of the stress test). The algorithms utilised include the second-order time-delayed PMLD matrix algorithm, Shan wavelet analysis, and a modified velocity of adaptation, which helped to generate two of the major health indicators (alpha and beta) and formulate the health biomarker gamma for new subject classification. The results show that healthy subjects display specific patterns in their ECG signals at the start of the load phase, at the point when the load ends, and in the early recovery phase. Unhealthy subjects also show distinct patterns during these same stages, but their behaviour differs from that of the healthy group. These differences in ECG patterns enable the separation of the two groups, thereby supporting the classification of subjects as either healthy or unhealthy.

### **3.3 Comparative Analysis of Matrix-Based Algorithms for ECG Parameter Analysis**

Research on perfect matrices of Lagrange differences (PMLD) has confirmed their potential for analysing ECG parameters and supporting the early detection of cardiac disease, as demonstrated in studies [13, 49, 53]. This section of the study aims to achieve the following objectives: (1) to utilise the existing matrix architecture PMLD (referred to as the Primary Matrix Framework, PMF) and compare its analytical and computational effectiveness with two other matrix architectures (referred to as Secondary Matrix Frameworks, SMF1 and SMF2); (2) to analyse all the matrix frameworks by systematically substituting ECG parameters into each matrix and select the most effective one; (3) to highlight the importance of the expansion of the local matrix architecture into the global matrix assembly; (4) to transform the matrix assembly into a scalar sequence using both the matrix norm and the matrix discriminant and identify the best scalar transformation technique for analysing ECG parameters. Before detailing the experimental results, the subsequent discussion outlines the bioethical permit, demographic characteristics of the study cohort, dataset overview, and software description.

#### **Bioethical Statement**

The study adhered to ethical standards in accordance with the Declaration of Helsinki and received prior approval from the Regional Biomedical Research Ethics Committee of the Lithuanian University of Health Sciences (ID No. BE-2-4, 17 March 2016). Biomedical investigation authorisation was granted by the LSMU Bioethics Committee, and participants provided written informed consent (see Annex C).

#### **Demographic Characteristics of the Study Cohort**

The study comprises fifteen individuals, including both males and females. The demographic characteristics of the entire cohort include the mean and standard deviation of age ( $65.84 \pm 1.4$  years), weight ( $79.4 \pm 0.9$  kg), and height ( $1.75 \pm 0.12$  m). The individuals are classified into the following two categories: healthy candidates and unhealthy candidates. The participants in the healthy classification are represented as  $H_{AF_n}$  and have no recorded history of atrial fibrillation, where H represents the healthy cohort, subscript AF represents the atrial fibrillation study, and

$n$  is the number of the candidate. The participants in the unhealthy classification are denoted as  $U_{AF_n}$ , with a recorded medical history of atrial fibrillation. It should be mentioned that none of the candidates were on any medication for arrhythmia.

### Dataset Overview and Software Description

The ECG data includes the time and amplitude information of the following: duration of the P wave (DP), measured in milliseconds (ms); amplitude of the P wave (AP), measured in millivolts (mV), QRS complex segment, measured in milliseconds (ms); inter-beat interval (RR Wave), measured in milliseconds (ms); JT Wave, measured in milliseconds (ms); and time, measured in milliseconds (ms). The total duration of the experiment is not more than seven minutes. The retrieved information is stored in a .txt format text file, and the computations are performed utilising original algorithms developed in the MATLAB environment.

### Description of the Methods and the Experimental Results

As described earlier, the notion of the matrix-based approach for analysing cardiac intervals originated from the studies undertaken by Ziaukas et al. and other researchers [13, 49, 53]. Following the inspiration from [13, 49, 53], the aim here is to propose two new matrix architectures and to adopt the PMF. These matrix architectures are:

- Perfect matrices of Lagrange differences, referred to as the Primary Matrix Framework (PMF)
- Secondary Matrix Framework 1 (SMF1)
- Secondary Matrix Framework 2 (SMF2)

#### Primary Matrix Framework (PMF)

This matrix architecture is founded on six specific criteria, as outlined in [13]. There are only eighteen matrices that fulfil all the above-mentioned six conditions [13]. In the following discussion, special attention is focused on the matrix number one among those eighteen matrices [13]. Without any loss of generality, considering the time series  $(x_n: n = 0, 1, 2, 3 \dots)$ ,  $(y_n: n = 0, 1, 2, 3 \dots)$ , and  $(z_n: n = 0, 1, 2, 3 \dots)$ , which correspond to the *JT* wave, the *QRS* complex, and the *RR* interval, where  $n$  represents the time moment and the parameter delta  $\delta$  represents the time lag, then the nine elements of the third-order PMF are:

$$\begin{bmatrix} x_n & y_{n+\delta} - x_{n+\delta} & z_{n+\delta} - x_{n+\delta} \\ y_{n-\delta} - x_{n-\delta} & y_n & z_{n+\delta} - y_{n+\delta} \\ z_{n-\delta} - x_{n-\delta} & z_{n-\delta} - y_{n-\delta} & z_n \end{bmatrix}.$$

Similarly, the nine elements of SMF1 are:

$$\begin{bmatrix} 2x_n & x_{n+1} - y_{n+1} & x_{n+1} - z_{n+1} \\ y_{n-1} - x_{n-1} & 2y_n & y_{n+1} - z_{n+1} \\ z_{n-1} - x_{n-1} & z_{n-1} - y_{n-1} & 2z_n \end{bmatrix},$$

and for SMF2 it is:

$$\begin{bmatrix} x_n + z_n & x_{n+1} - y_{n+1} & z_{n+1} - x_{n+1} \\ x_{n-1} - y_{n-1} & 2y_n & y_{n+1} - z_{n+1} \\ z_{n-1} - x_{n-1} & y_{n-1} - z_{n-1} & z_n + x_n \end{bmatrix}.$$

### Adjustable Configuration of the Matrix Architecture

The adjustability in matrix architecture refers to the degree of freedom to organise the matrix elements in different configurations while following the six criteria formulated in [13]. These constraints ensure that the order of elements in the matrix follows a consistent pattern, preserving the local matrix structure. This degree of freedom is possible for the SMF1 and PMF matrices because of their lexicographical balance, but it is not true for SMF2. Out of the four adjustable configurations, the one presented in (32) will be utilised for further analysis.

### Converting Matrix Sequences to Scalar Time Series

The process of determining the algebraic relationship between the ECG parameters relies on two key steps [13]. Initially, each scalar time series, which represents an ECG parameter, is converted into a series of matrices. Following this, these matrix sequences are transformed back into scalar time series via a mapping function  $\mathcal{F}: \mathbb{R}^{(m \times n)} \rightarrow \mathbb{R}^{(1 \times n)}$ , where  $m$  is the order of the matrix and  $n$  is the length of the original sequences. Different mapping functions  $\mathcal{F}$  can be applied for this transformation. For example, the norm of the matrix is used in [13], while the matrix discriminant serves as a basis for converting matrix sequences into scalar time series in [49]. Here, both the norm of the matrix as well as the discriminant of the matrix will be utilised for transforming the matrix into a scalar sequence.

### The Large Discriminant and the Norm of the Matrix

The elements of the SMF1 and SMF2 for the third-order matrix can be represented as:

$$MA_{a^{(n)}} = \begin{bmatrix} a_{11}^{(n)} & a_{12}^{(n)} & a_{13}^{(n)} \\ a_{21}^{(n)} & a_{22}^{(n)} & a_{23}^{(n)} \\ a_{31}^{(n)} & a_{32}^{(n)} & a_{33}^{(n)} \end{bmatrix}.$$

Then, the large discriminant of the matrix is expressed as:  $dsk_1(MA_a^{(n)}) = \rho_{12} * \rho_{13}$  where:

$$\rho_{12} = [a - \sqrt{a^2 - 3 \cdot b}]^2 \cdot [a + 2\sqrt{a^2 - 3 \cdot b}] - 27c \text{ and}$$

$$\rho_{13} = [a + \sqrt{a^2 - 3 \cdot b}]^2 \cdot [a - 2\sqrt{a^2 - 3 \cdot b}] - 27c.$$

Also,

$$a = \text{Inv}_1(MA_a^{(n)}) = a_{11}^{(n)} + a_{22}^{(n)} + a_{33}^{(n)},$$

$$b = \text{Inv}_2(MA_a^{(n)}) = a_{22}^{(n)} \cdot a_{33}^{(n)} + a_{11}^{(n)} + a_{22}^{(n)} + a_{11}^{(n)} \cdot a_{33}^{(n)} - a_{13}^{(n)} \cdot a_{31}^{(n)} - a_{21}^{(n)} \cdot a_{12}^{(n)} - a_{32}^{(n)} \cdot a_{23}^{(n)}, \text{ and}$$

$$c = \text{Inv}_3(MA_n) = \det(MA_n) [107, 138].$$

In [13], the norm of the matrix is used as the mapping function to transform the PMF into a scalar time series. The same mapping function is also adopted in this work.

### The Comparison between the Matrix Norm and the Matrix Discriminant and the Selection of the Best Matrix Architecture

The three ECG parameters (the JT wave, the duration of the QRS complex, and the RR inter-beat interval), represented by the time series ( $x_n: n = 0, 1, 2, 3 \dots$ ), ( $y_n: n = 0, 1, 2, 3 \dots$ ), and ( $z_n: n = 0, 1, 2, 3 \dots$ ), are pre-processed by applying a threshold range to ensure that each input value remains within physiologically plausible limits. For this purpose, the minimum and maximum values for each of the time series are chosen as follows:  $x_{(\min)} = 100 \text{ ms}$ ;  $x_{(\max)} = 400 \text{ ms}$ ;  $y_{(\min)} = 80 \text{ ms}$ ;  $y_{(\max)} = 110 \text{ ms}$ ;  $z_{(\min)} = 600 \text{ ms}$ ; and  $z_{(\max)} = 1200 \text{ ms}$ , respectively. Any values falling below the lower bounds or exceeding the upper bounds are adjusted to the respective minimum or maximum values. The adjusted values of the time series  $x_n$ ,  $y_n$ , and  $z_n$  are then normalised to a range between 0 and 1. For instance, the time series  $x_n$  is normalised as  $x_{\text{normalised}} = (x - 100)/(400 - 100)$ . Similarly, the time series  $y_n$  and  $z_n$  are processed through the same normalisation technique, respectively. The same normalisation techniques are also used in [107].

The pre-processed and normalised time series  $x_n$ ,  $y_n$ , and  $z_n$  are fitted to the third-order matrix architectures that represent the PMF, SMF1, and SMF2, respectively. To transform the third-order matrix into a scalar series via the mapping function  $\mathcal{F}: \mathbb{R}^{3 \times 3} \rightarrow \mathbb{R}^{1 \times 3}$ , twofold mapping techniques are employed. The large discriminant of the matrix is used as the mapping function for SMF1 and SMF2 architectures, while the norm is used as the mapping function for the PMF architecture, respectively. Internal and external smoothing techniques are applied with the smoothing radius adjusted to the values optimised in [13]. Finally, the statistical metric, such as the variance of the norm as well as the variance of the large discriminant, is calculated for each produced time sequence from the three original time series  $x_n$ ,  $y_n$ , and  $z_n$ . The resulting values are depicted in Table 9 and Table 10, respectively.

**Table 9.** Variance Metrics for Healthy Candidates in PMF, SMF1, and SMF2

List of Healthy candidates, $H_{AFn}$	PMF	SMF1		SMF2	
	Variance of the Norm	Variance of the Large discriminant	Variance of the Norm	Variance of the Large discriminant	Variance of the Norm
$H_1$	0.0012	0.0640	0.0016	0.042	0.0010
$H_2$	0.0030	0.0633	0.0047	0.0313	0.0038
$H_3$	0.0023	182.4470	0.0027	16.167	0.0020
$H_4$	0.0014	44.6925	0.0014	1.6402	0.0014
$H_5$	0.0040	608.0258	0.0076	94.7592	0.0052
$H_6$	0.0025	12.4591	0.0026	2.9064	0.0008
$H_7$	0.0031	1618.7723	0.0042	1490.7099	0.0216
$H_8$	0.0018	62.0865	0.0042	65.921	0.0165

**Table 10.** Variance Metrics for Unhealthy Candidates in PMF, SMF1, and SMF2

List of unhealthy candidates, $U_{AFn}$	PMF	SMF1		SMF2	
	Variance of the Norm	Variance of the Large discriminant	Variance of the Norm	Variance of the Large discriminant	Variance of the Norm
$U_1$	0.0006	1144.7393	0.0012	21.2530	0.0008
$U_2$	0.0004	1358.7248	0.0006	21.9133	0.0005
$U_3$	0.0082	15.2796	0.0171	2.5576	0.0177
$U_4$	0.0064	339.2649	0.0066	1566.6759	0.0111
$U_5$	0.0030	4.8991	0.0023	0.9349	0.0030
$U_6$	0.0014	84.2605	0.0013	3.0256	0.0022

Table 9 and Table 10 represent the variance values that are generated from the scalar time series for the entire cohort, using both the large discriminant and the norm of the matrix, respectively. The tabulated values clearly indicate that the variance of the norm provides valuable insights necessary for classification purposes. In contrast, the large discriminant displays numeric values that lack meaningfulness for further computations. For example, in the healthy cohort, the variance of the large discriminant has a minimum and maximum range between 0.042 and 1618.7723, while in the unhealthy group, it ranges from 0.0006 to 1358.7248. In contrast, the variance of the norm displays more meaningful results, which are necessary for classification purposes. For instance, the minimum and maximum range of the norm values lies between 0.0010 and 0.0216 (for the healthy cohort) and 0.0004 and 0.0177 (for the unhealthy cohort).

Two key perspectives are presented for interpreting the study's outcomes based on meaningful analytical insights. First, when comparing the PMF, SMF1, and SMF2, it is evident that SMF2 does not adhere to the criteria outlined for a perfect matrix. As a result, it is not considered a suitable matrix architecture for ECG analysis in this study. Furthermore, while SMF1 meets all the necessary conditions to qualify as a perfect matrix, the presence of a scalar multiplier on the main diagonal is discouraged when performing ECG parameter analysis [13]. Consequently, SMF1 is also excluded from consideration as the best matrix architecture for the ECG analysis application. Therefore, the PMF stands out as the most suitable matrix architecture and will be used for the analysis in the subsequent analysis.

Second, since transforming the matrix assembly into a scalar time series is also essential, both the matrix norm and the large discriminant were evaluated to determine which is more suitable. All three matrix architectures—PMF, SMF1, and SMF2—were considered in this assessment. The analytical results show that the matrix norm yields more reliable outcomes across all matrix structures when scalar transformation is required, compared to the large discriminant.

Therefore, a computationally reliable foundation is established for employing the PMF and matrix norm as the primary methods for detecting atrial fibrillation episodes in the subsequent analysis.

### **Conclusive Insights from the Study**

A comparative analysis was conducted among the three matrix architectures by fitting the three ECG parameters into them. The PMF matrix structure proved to be effective in analysing ECG parameters and identifying relationships among them. The PMF outperformed the other two matrix frameworks (SMF1 and SMF2), as SMF2 does not adhere to the perfect matrix rules, while SMF1, despite compliance, includes a scalar multiplier in the main diagonal, which is not encouraged for ECG signal analysis.

Additionally, when both matrix norm and discriminant analysis were performed to determine the best method for scalar transformation, the matrix norm provided more reliable analytical outcomes.

### **3.4 Matrix-Based Algorithm for the Detection of Atrial Fibrillation (PMF Expandability from Second- to Fifth-Order)**

This section continues from the previous one but focuses on the expansion analysis of the PMF for generating the categorisation interval as a diagnostic aid system. However, the ethical protocol, study subjects, and demographic information of the study candidates remain consistent with those presented in the previous section.

The objectives of this study are as follows: (1) to perform the expandability analysis of the matrix from the second-order to the fifth-order PMF by incorporating the following ECG parameters: the duration of the JT wave, the QRS complex, the RR inter-beat interval, the amplitude of the P wave, and the duration of the P wave. (2) To analyse the performance of each PMF order. It is hypothesised that increasing the matrix order enhances both sensitivity and variability due to the fact that more information is provided to the decision-making algorithm. Sensitivity in this study is defined as a quantitative measure of the overall matrix assembly in providing better classification. Variability, on the other hand, is a qualitative measure of the data distribution points for the categorisation threshold. Better variation leads to more effective categorisation of the individuals. (3) To generate a diagnostic aid system for testing candidates and validating the proposed algorithm.

### **Structural Configuration of the Study**

The structural layout of this algorithm is visually presented in Fig. 21. The entire framework of the study is classified into three main blocks. Each of these blocks is thoroughly explained and discussed below.



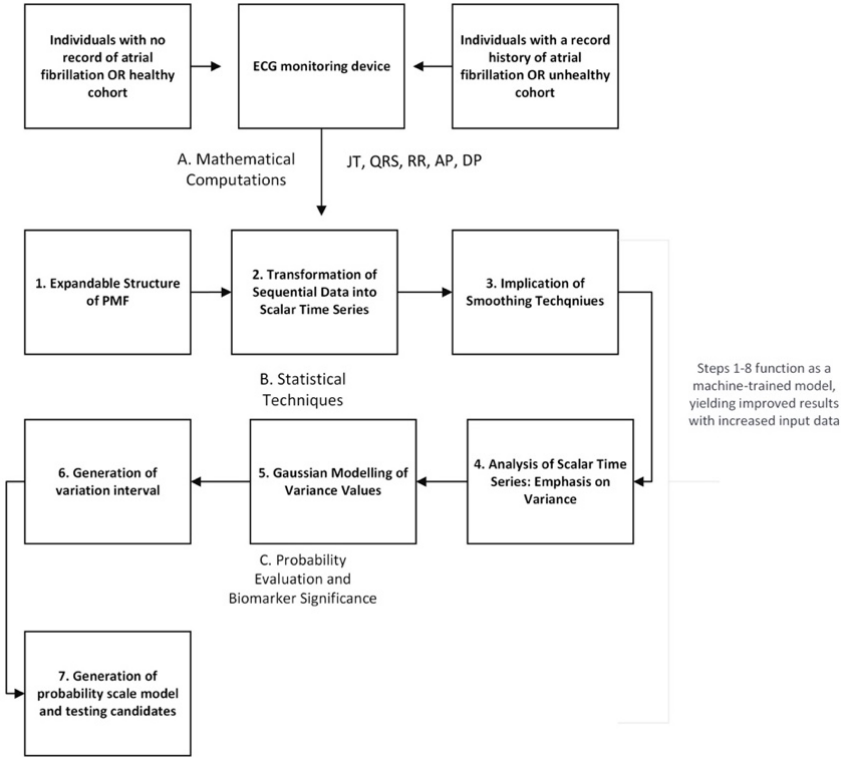


**Fig. 21.** Structure of the Computational Setup: (A) Mathematical Computations, (B) Statistical Techniques, (C) Probabilistic Evaluation and Biomarker Significance

### Block A (Mathematical Computations)

#### Expandable Structure of PMF from Second- to Fifth-Order Matrices

The five ECG parameters (the JT wave, the duration of the QRS complex, the RR interval, the AP wave, and the DP wave) are represented by time series ( $x_n: n = 0, 1, 2, 3 \dots$ ), ( $y_n: n = 0, 1, 2, 3 \dots$ ), ( $z_n: n = 0, 1, 2, 3 \dots$ ), ( $u_n: n = 0, 1, 2, 3 \dots$ ), and ( $v_n: n = 0, 1, 2, 3 \dots$ ). These time series are fitted into the matrix architecture of the PMF and are expanded from the second- to the fifth-order matrix. The second-order PMF reads:

$$\begin{bmatrix} x_n & y_{n+\delta} - x_{n+\delta} \\ y_{n-\delta} - x_{n-\delta} & y_n \end{bmatrix}.$$

The third-order PMF reads:

$$\begin{bmatrix} x_n & y_{n+\delta} - x_{n+\delta} & z_{n+\delta} - x_{n+\delta} \\ y_{n-\delta} - x_{n-\delta} & y_n & z_{n+\delta} - y_{n+\delta} \\ z_{n-\delta} - x_{n-\delta} & z_{n-\delta} - y_{n-\delta} & z_n \end{bmatrix}.$$

Likewise, the fourth-order PMF follows:

$$\begin{bmatrix} x_n & y_{n+\delta} - x_{n+\delta} & z_{n+\delta} - x_{n+\delta} & u_{n+\delta} - x_{n+\delta} \\ y_{n-\delta} - x_{n-\delta} & y_n & z_{n+\delta} - y_{n+\delta} & u_{n+\delta} - y_{n+\delta} \\ z_{n-\delta} - x_{n-\delta} & z_{n-\delta} - y_{n-\delta} & z_n & u_{n+\delta} - z_{n+\delta} \\ u_{n-\delta} - x_{n-\delta} & u_{n-\delta} - y_{n-\delta} & u_{n-\delta} - z_{n-\delta} & u_n \end{bmatrix}.$$

Similarly, the fifth-order PMF reads:

$$\begin{bmatrix} x_n & y_{n+\delta} - x_{n+\delta} & z_{n+\delta} - x_{n+\delta} & u_{n+\delta} - x_{n+\delta} & v_{n+\delta} - x_{n+\delta} \\ y_{n-\delta} - x_{n-\delta} & y_n & z_{n+\delta} - y_{n+\delta} & u_{n+\delta} - y_{n+\delta} & v_{n+\delta} - y_{n+\delta} \\ z_{n-\delta} - x_{n-\delta} & z_{n-\delta} - y_{n-\delta} & z_n & u_{n+\delta} - z_{n+\delta} & v_{n+\delta} - z_{n+\delta} \\ u_{n-\delta} - x_{n-\delta} & u_{n-\delta} - y_{n-\delta} & u_{n-\delta} - z_{n-\delta} & u_n & v_{n+\delta} - u_{n+\delta} \\ v_{n-\delta} - x_{n-\delta} & v_{n-\delta} - y_{n-\delta} & v_{n-\delta} - z_{n-\delta} & v_{n-\delta} - u_{n-\delta} & v_n \end{bmatrix}.$$

The ECG parameters are mapped into each matrix order, with the matrix norm providing the scalar time series. For each participant, the variance of this scalar series is calculated, representing the healthy and unhealthy groups. The resulting variance values are listed in Table 11 and Table 12.

**Table 11.** Variance Values of Scalar Time Series Generated by Second- to Fifth-Order PMF for Healthy Individuals

2 <sup>nd</sup> -order PMF variance values, $\sigma_{HAFn}^2$		3 <sup>rd</sup> -order PMF variance values, $\sigma_{HAFn}^2$	4 <sup>th</sup> -order PMF variance values, $\sigma_{HAFn}^2$	5 <sup>th</sup> -order PMF variance values, $\sigma_{HAFn}^2$
JT, QRS	JT, RR	JT, QRS, RR	JT, QRS, RR, DP	JT, QRS, RR, AP, DP
0.0018	0.0004	0.0012	0.0069	0.0096
0.0015	0.0002	0.0029	0.0029	0.0074
0.0013	0.0009	0.0023	0.0030	0.0150
0.0007	0.0005	0.0014	0.0019	0.0022
0.0030	0.0011	0.0040	0.0020	0.0056
0.0018	0.0005	0.0025	0.0033	0.0033
0.0013	0.0005	0.0031	0.0021	0.0109
0.0007	0.0018	0.0018	0.0019	0.0038

**Table 12.** Variance Values of Scalar Time Series Generated by Second- to Fifth-Order PMF for Unhealthy Individuals

2 <sup>nd</sup> -order PMF variance values, $\sigma_{UAFn}^2$		3 <sup>rd</sup> -order PMF variance values, $\sigma_{UAFn}^2$	4 <sup>th</sup> -order PMF variance values, $\sigma_{UAFn}^2$	5 <sup>th</sup> -order PMF variance values, $\sigma_{UAFn}^2$
JT, QRS	JT, RR	JT, QRS, RR	JT, QRS, RR, DP	JT, QRS, RR, AP, DP
0.0005	0.0001	0.0006	0.0031	0.0034
0.0002	0.0001	0.0004	0.0004	0.0004
0.0073	0.0023	0.0082	0.0229	0.0133
0.0049	0.0012	0.0064	0.0039	0.0065
0.0014	0.0003	0.0030	0.0100	0.0117
0.0007	0.0004	0.0014	0.0036	0.0039

Table 11 shows the results for the variance values of the PMF architecture for the healthy individuals from the second- to fifth-order matrices. A general tendency in the variance values can be seen for the healthy cohort. Both sensitivity and variability are calculated from these variance values. As previously stated, the sensitivity of the matrix relates to its ability to produce greater variance values as the size of the matrix increases. For instance, the candidates from the healthy group, such as  $H_2$ ,  $H_4$ ,  $H_6$ , and  $H_8$ , have higher sensitivity generated by the higher-order matrices. Other individuals from the healthy group, such as  $H_1$ ,  $H_3$ ,  $H_5$ , and  $H_7$ , have also shown an increase in the variance values, except for the fourth-order PMF. For instance, the individual  $H_7$  has shown an increase in the variance values in the second-, third-, and fifth-order matrices, but a lower variance value in the fourth-order as compared to the third-order PMF. For the unhealthy group (in Table 12), it can be observed that the candidates  $U_1$ ,  $U_3$ ,  $U_6$ , and  $U_8$  have shown an increase in sensitivity as the matrix order increases. The candidate  $U_2$  has shown a very consistent sensitivity as the order of the matrix increases.

Variability is defined as a qualitative metric that represents the degree of data dispersion (variance values), approximated by the Gaussian distribution curve, which is important for the classification of individuals [49, 119]. Fig. 22 displays the variability of the data spread for the healthy group for the third- and fifth-orders of the PMF. It can be seen that there are a few cases in the unhealthy group showing variability in their data, but when the healthy and unhealthy groups are compared, the healthy group shows a larger degree of variability.

### **Block B (Statistical Analysis)**

A three-step statistical analysis is performed to generate the distributions that are later employed in the decision support system. Each of these steps is explained in detail below.

#### **Gaussian Modelling of the Variance Values**

Building on the previously outlined statistical procedures, a similar approach is applied to (1) fit variance values to the Gaussian distribution, (2) conduct a normality test using the Anderson–Darling (AD) test, and (3) establish the variation interval. However, the mathematical formula used to generate the probability distribution chart, and the decision-making techniques involves a distinct mathematical approach. The variance ( $\sigma^2$ ) values from Table 11 and Table 12 for both healthy and unhealthy groups are fitted to the Gaussian distribution. First, the Anderson–Darling (AD) test is performed as the goodness-of-fit metric to assess the degree to which the variance values obtained follow a normal distribution. The probability density object is fitted to the data using the normal Gaussian distribution. The basic statistical parameters such as mean ( $\mu_h, \mu_u$ ) and standard deviation ( $\sigma_h, \sigma_u$ ) are extracted from the probability density function, and then the probability density functions are plotted in Fig. 22. For the healthy cohort, the distribution data and the bell curve are represented in blue, whereas for the unhealthy cohort, red is used. The  $x$ -axis represents the distribution of the data (variance values), and the  $y$ -axis represents the probability density curve. This step aims to establish the distributions that can provide sufficient

statistical information to generate the variation interval for the classification of the test candidates. This step is performed for both the third- and fifth-order PMF, as seen in Fig. 22.

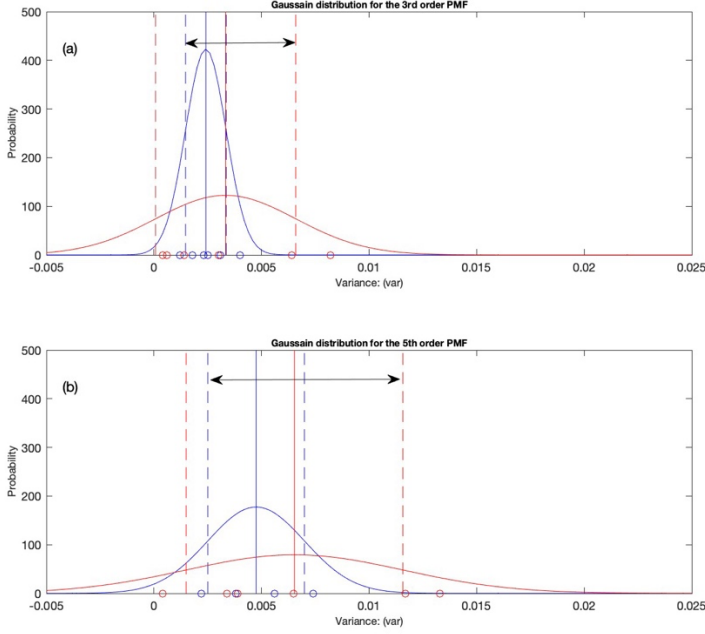


**Fig. 22.** Gaussian Distribution: (a) 3<sup>rd</sup>-Order PMF Distribution, (b) 5<sup>th</sup>-Order PMF Distribution; Black Horizontal Arrows Denote Variation Intervals

### Generation of the Variation Interval for Classification Purposes

The mean ( $\mu_h, \mu_u$ ) and standard deviation ( $\sigma_h, \sigma_u$ ) values are adopted from the previous step to generate the variation interval. The central tendency of normally distributed data is visualised by drawing a solid vertical line for the mean data. Additionally, the vertical dashed lines are plotted one standard deviation below and above the mean. It is essential to define the two boundaries of the variation interval, which is determined using a simple mathematical operation: the left and the right boundaries of the variation interval are defined as  $(\mu_h - \sigma_u)$  and  $(\mu_u + \sigma_h)$ , respectively. The connectivity of the two boundaries is signified by a double-headed arrow, as seen in Fig. 22. The region between the arrows serves as the variation interval used to classify new candidate(s) according to the conditions defined in Table 13. To enhance the classification accuracy of the test candidates, a machine-trained model is generated. This includes developing a self-trained model to evaluate the algorithm classification accuracy and establishing a decision support system for testing the candidates. The requirements in Table 13 must be followed by the test candidate so that the individual may be classified as either a healthy or unhealthy subject. For classification, one of the three conditions must be adhered to, as tabulated in Table 13. If we represent a new incoming candidate as  $Z$ , and the interpolation

coefficient is represented as  $L$ , then the corresponding three sets of conditions are described as follows:

**Condition 1 ( $L = 0$ ):** Condition 1 shows that the probability indicator  $L$  will be zero if the value of the variance for the incoming candidate  $Z$  is less than or equal to the lower boundary  $(\mu_h^{(3)} - \sigma_h^{(3)})$ , which is established for the healthy individuals. This condition allows for the classification of incoming candidates with a low probability of belonging to the unhealthy group.

**Condition 2 ( $L = 1$ ):** Condition 2 sets the probability indicator  $L$  to one if the value of the variance for the test candidate  $Z$  is greater than or equal to the upper boundary  $(\mu_u^{(3)} + \sigma_u^{(3)})$  for the unhealthy individuals. This condition signifies a high probability that the candidate belongs to the unhealthy group.

**Condition 3 ( $0 \leq L \leq 1$ ):** If the value of the variance for the incoming candidate  $Z$  falls within the range between the upper boundary established for unhealthy individuals and the lower boundary established for healthy individuals, the probability indicator is calculated using a linear interpolation formula, which reads:  $L = \frac{Z - (\mu_u^{(3)} + \sigma_u^{(3)})}{(\mu_h^{(3)} - \sigma_h^{(3)}) - (\mu_u^{(3)} + \sigma_u^{(3)})}$ . The condition reflects a probability between 0 and 1, indicating the candidate's likelihood of belonging to either the healthy or the unhealthy group based on the degree to which their variance value deviates from the established boundaries. These conditions are applied for both the third- and fifth-order PMF, as shown in Table 13.

**Table 13.** Classification Criteria for Decision Support System Development

For the 3 <sup>rd</sup> -order PMF			
If	Condition 1	Condition 2	Condition 3
	$Z \leq (\mu_h^{(3)} - \sigma_h^{(3)})$	$Z \geq (\mu_u^{(3)} + \sigma_u^{(3)})$	$(\mu_u^{(3)} + \sigma_u^{(3)}) \leq Z \leq (\mu_h^{(3)} - \sigma_h^{(3)})$
Then, the probability indicator is:	$L = 0$	$L = 1$	$L = \frac{Z - (\mu_u^{(3)} + \sigma_u^{(3)})}{(\mu_h^{(3)} - \sigma_h^{(3)}) - (\mu_u^{(3)} + \sigma_u^{(3)})}$
The candidate is classified as:	Healthy	Unhealthy	In between the healthy and unhealthy group based upon the variance values
For the 5 <sup>th</sup> -order PMF			
If	$Z \leq (\mu_h^{(5)} - \sigma_h^{(5)})$	$Z \geq (\mu_u^{(5)} + \sigma_u^{(5)})$	$(\mu_u^{(5)} + \sigma_u^{(5)}) \leq Z \leq (\mu_h^{(5)} - \sigma_h^{(5)})$

Then, the probability indicator is:	$L = 0$	$L = 1$	$L = \frac{Z - (\mu_u^{(5)} + \sigma_u^{(5)})}{(\mu_h^{(5)} - \sigma_h^{(5)}) - (\mu_u^{(5)} + \sigma_u^{(5)})}$
The candidate is classified as:	Healthy	Unhealthy	In between the healthy and unhealthy group based upon the variance values

### Block C (Probability Evaluation and Biomarker Significance)

#### Generation of Probability Scale Marker and Testing Candidates

Based on the conditions outlined in Table 13, a probability indication marker is generated, and the range of the probability scale lies between 0 and 1. An intersection point is also generated according to the probability placement of the test candidate and is represented by the dashed line. The  $x$ -axis represents the variance point distributions, whereas the  $y$ -axis shows the probability distribution points. The likelihood of the individual falling into the probability graph can be seen in subplot (b) of Fig. 22.

Two candidates are tested to evaluate the accuracy of the proposed matrix architecture. The static ECG of these two candidates is recorded, and the parameters such as the duration of the JT wave, the QRS complex, the RR interval, the AP wave, and the DP wave represent the time series  $(x_n: n = 0, 1, 2, 3 \dots)$ ,  $(y_n: n = 0, 1, 2, 3 \dots)$ ,  $(z_n: n = 0, 1, 2, 3 \dots)$ ,  $(u_n: n = 0, 1, 2, 3 \dots)$ , and  $(v_n: n = 0, 1, 2, 3 \dots)$  respectively. There is existing knowledge regarding the cardiovascular status of the individuals, specifically their history of atrial fibrillation. For instance, the first candidate has no recorded history of atrial fibrillation, whereas the second candidate has a documented history of atrial fibrillation. The purpose of testing the static ECG of these candidates is to evaluate the accuracy of the proposed matrix architecture of the third- and fifth-order PMF and to assess the overall classification accuracy of the algorithm. A semi-gauge indication tool has also been developed, which assesses an individual's health status using three colours. For example, when the gauge indicator's needle points to green, it indicates that the person's cardiovascular health is generally good. If the needle moves towards yellow, it suggests that the individual's cardiovascular health is in a warning zone. If it points to red, it indicates that the person's cardiovascular health needs medical attention.

First, the time series are pre-processed using the techniques described in the Methods. The pre-processed parameters are then fitted into the third- and fifth-order PMLD matrix layouts. The matrix architectures are converted into scalar time series using the norm as the mapping function. The variance of the norm is then computed for each of the test candidates.

For the first candidate, the variance value places the individual at the left end of the distribution for the third-order PMF, as shown in Panel A of Fig. 23. An asterisk sign is an indication of the individual's location inside the classification interval. The

variance value is passed through the interpolation rules as indicated in Table 13, and Condition 1 is satisfied for this particular individual, which is an indication of the individual belonging to the healthy group. Furthermore, the probability distribution chart shows a likelihood of less than 0.1 for the individual to be unhealthy, indicating their placement in the healthy group, as seen in Panel B of Fig. 23. Finally, the semi-gauge indication tool in Panel F of Fig. 23 gives a reading in the green zone, indicating that the test candidate is healthy (from the perspective of cardiovascular health) and is in the safe zone.

The same algorithm and computational techniques are used for the classification of the individual using the fifth-order PMF matrix design. The resultant variance value places the individual in the healthy category, as illustrated in Panel D of Fig. 23. The decision support system, adhering to the rules established in Table 3, also shows that the individual has no likelihood of being classified as unhealthy. Finally, the semi-gauge indicator tool places the individual in the green zone, as shown in Panel F of Fig. 23.

Both the third- and the fifth-order PMF matrix configurations classify the individual as a healthy one. Although it was already known that the individual has no history of atrial fibrillation, the proposed algorithm also classifies the individual as healthy. Moreover, as the matrix size is increased from the third- to the fifth-order, the sensitivity of the algorithm is seen to increase further.

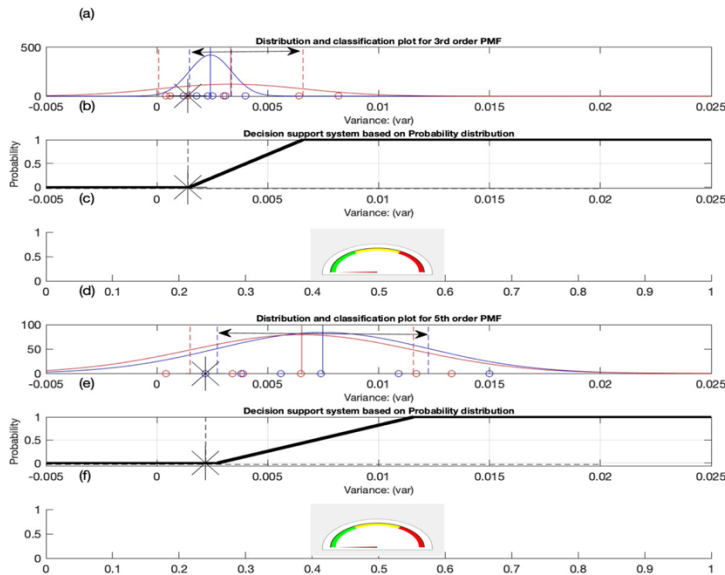


**Fig. 23.** Test Candidate 1 Classification: 3<sup>rd</sup>- and 5<sup>th</sup>-Order PMF Architecture

The ECG parameters of another test candidate are assessed employing the third- and the fifth-order PMF architecture classification criteria. When the ECG parameters are analysed using the third-order PMF matrix, the individual falls within the classification interval for the unhealthy candidates, as illustrated in Panels A through C of Fig. 24. The decision support system also demonstrates a high likelihood of the

individual being unhealthy, which is supported by the semi-gauge indicator tool that points to the red zone. In addition, the individual's ECG parameters are evaluated using the fifth-order PMF architecture, and the algorithm classifies the person as unhealthy (Fig. 24, Panels D–F).

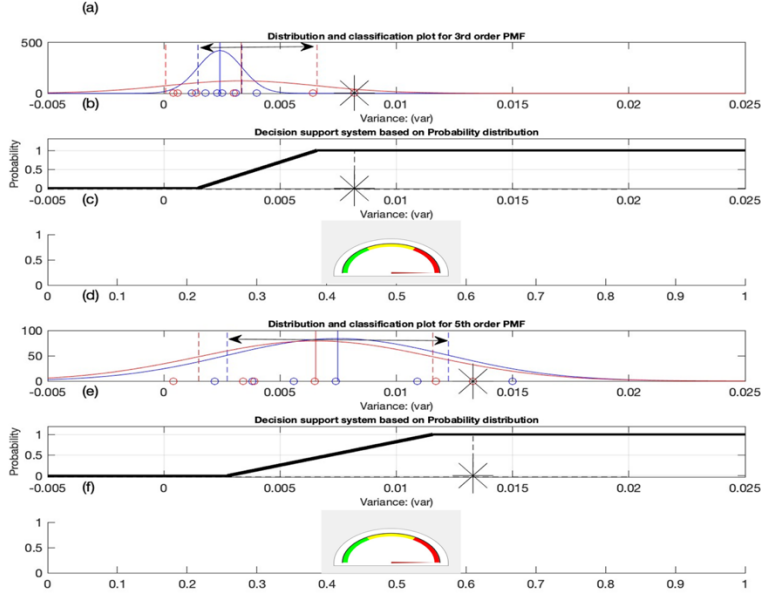


**Fig. 24.** Test Candidate 2 Classification: 3<sup>rd</sup>- and 5<sup>th</sup>-Order PMF Architecture

### Conclusive Insights from the Study

The PMF architecture is expandable by increasing the size of the matrix, allowing for additional ECG parameters to be incorporated in higher-order matrices, such as second-, third-, fourth-, and fifth-order PMF. This increase in matrix size enhances both the sensitivity and the variability of the classification algorithm. Both sensitivity and variability are associated with the generation of the classification interval and the decision support system, which functions as a machine-trained model whose output is directly linked to the input. The more input that is added into the proposed algorithm, the more accurate and robust results are produced. The robustness of the algorithm is assessed by testing the candidates. The clinical significance of the study can be observed in the diagnosis of atrial fibrillation episodes.

### 3.5 Matrix-Based Algorithm for HRV Analysis in Psychological Synchronisation during Meditation

Heart rate variability (HRV) measures the changes in time intervals between successive heartbeats, representing the activity of regulatory systems that respond to environmental and psychological conditions [139]. HRV is typically derived from the series of RR inter-beat intervals, which represent the time between consecutive R-wave peaks in an ECG signal. This variability in the sequence of RR inter-beat intervals serves as a robust metric for analysing changes in autonomic nervous system (ANS) dynamics, making HRV a well-validated method for detecting real-time ANS



changes in ambulatory settings. It enables the simultaneous monitoring of multiple individuals with synchronised timing, making it an ideal approach to investigate the real-time, complex dynamics of group interactions and psychological processes. To analyse the HRV signal, various algorithms are adopted, including chaotic analysis [140], frequency-based analysis [141], and non-linear time series analysis [142]. Non-linear analysis techniques can help to understand and visualise the subtle processes occurring in the ANS and the cardiovascular system [143]. For instance, the Hankel matrix-based approach is used to analyse non-linear time series and identify algebraic relationships between these series [79, 80, 86].

The objectives of this section can be stated as follows: (1) to analyse the HRV signal using a matrix-based approach called the Hankel matrix to detect complexity matching between two groups during the meditation protocol. (2) It is hypothesised that the Hankel matrix approach can help to detect and visualise the synchronisation activities occurring during meditation between the two groups, one known as the Healers group and the other as the Healee. (3) Additionally, another technique, permutation entropy (PE), is also adopted to determine if the complexity-matching phenomenon can also be observed through this approach. (4) Furthermore, the phase plane visualisation technique and statistical operations are also employed to cross-validate the outcomes of the H-rank algorithm, which are used to analyse the complex phenomena occurring during meditation. This work represents a state-of-the-art approach with significant applications in clinical nursing practice, where the detecting complexity-matching processes can otherwise be challenging. Moreover, this study provides the first known computational proof for quantifying and visualising complexity-matching phenomena occurring during meditation.

### **Bioethical Statement**

This research adhered strictly to the ethical standards for experimentation outlined in the Declaration of Helsinki, following approval from the Regional Biomedical Research Ethics Committee of the Lithuanian University of Health Sciences (ID No. BE-2-4, 15 March 2016). The permit required for conducting the biomedical investigation was granted. All participants provided written informed consent prior to their involvement in the experiment. The soft copy of the ethical permit is included in Annex C.

### **Demographic Characteristics of the Study Cohort**

Nine female volunteer meditators took part in a 7-day meditation retreat led by Dr. Joe Dispenza in the United States in September 2019. Throughout the retreat, the study participants immersed themselves in guided meditation sessions that included sitting, standing, lying, walking, and healing-focused postures. The eight Healers had minimal interaction with their designated Healee before the healing protocol and were unaware of the Healee's specific medical diagnosis. It can be stated that these sessions were purely guided, without implementing any control mechanisms that could potentially influence the Healers or the Healee. Before the retreat, participants were required to complete an online compliance form providing details such as their name, gender, date of birth, pre-existing health conditions, current meditation condition, and consent. This process facilitated the identification of the subjects with pre-existing

health conditions, including one participant designated as a Healee who had a non-cardiac lung fibrosis post-pneumonia; the remaining eight participants, termed as Healers, reported no current or prior health issues. The average age of all the study participants ranged from 33 to 67 years, with a mean age of 48 years.

### **Dataset Overview and Software Description**

All nine participants in the study underwent continuous 75-minute ambulatory HRV recordings using high-resolution HRV recorders. The HRV recorders calculated the RR inter-beat intervals from the electrocardiogram with a sampling rate of 1000 Hz and stored the RR intervals in their memory. Subsequently, the HRV data were transferred to a workstation and processed to remove artefacts. This processing involved both automated methods and manual intervention by an expert technician. For example, automated algorithms were used to exclude RR intervals that deviated by more or less than 30% from the mean of the previous four intervals. HRV recordings were segmented into consecutive five-minute intervals, and segments with more than 10% missing or excluded RR intervals were discarded from further analysis. Manual review by the technician ensured additional data accuracy where needed. Local timestamps within the HRV recordings facilitated synchronised data analysis across all nine participants.

### **Description of the Methods and the Experimental Results**

The experiment is referred to as the meditation healing protocol, which lasted for 75 minutes. The experimental procedure included various guided meditation postures: sitting, standing, lying, walking, and healing-focused positions. These postures were divided into nine phases, and the corresponding RR intervals were recorded, as detailed in the accompanying Table 14.

The protocol began with the first phase, where the eight Healers gathered. In the second phase, the Healers stood with their eyes closed for fifteen minutes. During the third phase, the Healers opened their eyes and walked around the conference room for eleven minutes. This was followed by a brief return to standing meditation with eyes closed, constituting phase four. In phase five, the Healers opened their eyes and formed circles of eight. In phase six, the Healee entered the conference room and took her position in the healing circle. Phase seven involved all Healers sitting around the Healee and engaging in a heart-centred meditation. Phase eight commenced with the Healers rubbing their hands together and extending them towards the Healee, intending to direct their elevated individual energy to the Healee and synchronise it with the collective energy of all Healers. Finally, in phase nine, the Healers placed their hands over their own hearts, marking the conclusion of the healing meditation protocol. These explanations are tabulated in Table 14.

**Table 14.** Healing Meditation Phases: Timing and Descriptions

Phase #	Local Time in Hours and Minutes		Time in Seconds		Description of Healing Meditation Phases
	Start	End	Start	End	
1	17:00	17:06	0	360	Assembly of Healers
2	17:06	17:21	360	1260	First Standing Meditation
3	17:21	17:32	1260	1920	Guided Walking Meditation
4	17:32	17:35	1920	2100	Continued Standing Meditation
5	17:36	17:39	2160	2340	Creation of Healing Circles
6	17:39	17:51	2340	3060	Entry of Healees into Healing Circles
7	17:51	18:01	3060	3660	Healers and Healees Establish Connection
8	18:01	18:07	3660	4020	Healers Transmit Energy to the Healee
9	18:07	18:15	4020	4500	Conclusion of the Healing Meditation by Healers

### The H-rank Matrix-Based Algorithm for the Analysis of the HRV of the Healers and the Healee

Consider a Hankel matrix  $P_k$  defined as: 
$$\begin{bmatrix} l_0 & l_1 & \cdots & l_{k-1} \\ l_1 & l_2 & \cdots & l_k \\ \vdots & \vdots & \ddots & \vdots \\ l_{k-1} & l_k & \cdots & l_{2k-2} \end{bmatrix}$$
. In this matrix,

each diagonal  $p+q = s$  has identical entries, i.e.  $b_{p,s-q} = w_s$  for some sequence  $w_s$ .

Given a scalar time series,  $(y_n)_{n=1}^{\infty}$ , the  $n^{th}$  order Hankel matrix is defined as:  $H_n =$

$$\begin{bmatrix} y_1 & y_2 & \cdots & y_n \\ y_2 & y_3 & \cdots & y_{n+1} \\ \vdots & \vdots & \ddots & \vdots \\ y_n & y_{n+1} & \cdots & y_{2n-1} \end{bmatrix}$$
. One of the objectives of this study is to adopt the Hankel

matrix-based algorithm for analysing the HRV of two groups, aiming to assess the synchronisation that occurred over different phases of the meditation between the two groups (eight Healers and one Healee). A Hankel matrix is generated from the time series data, consisting of HRV captured from the ECG of the Healers and the Healee during the meditation activity. This matrix is constructed so that each row is a shifted version of the previous row, ensuring maximum overlap between observation windows. This rank-wise processing of the matrix elements is called H-rank. In this analysis, the Hankel matrix algorithm utilises a window size of 150-by-150, corresponding to 300 observed data points, with the matrices ranging from a minimum of 1 to a maximum of 150. Singular value decomposition (SVD) is then applied to this Hankel matrix in order to decompose the matrix into three constituent matrices. The singular values on the diagonal of the Hankel matrix indicate the significance of different components within the time series data, with higher singular values. By

identifying the singular values greater than a specified threshold epsilon ( $\epsilon$ ), the rank or complexity of the data at different points in time can be determined. To refine the analysis and make the trends in HRV data more apparent, a smoothing moving average technique is also applied to the reconstructed time series derived from the H-rank. This technique helps to smooth out short-term fluctuations and highlight the trends and patterns in the data by averaging each value in the H-rank vector with its neighbouring values within a specified window size, which is 3 in this study. The HRV of the eight Healers and one Healee is plotted in blue and red in Fig. 25. The x-axis represents the time in seconds frame, whereas the y-axis shows the temporal information of the HRV. The vertical segmentation shows the nine phases of the meditation exercise.

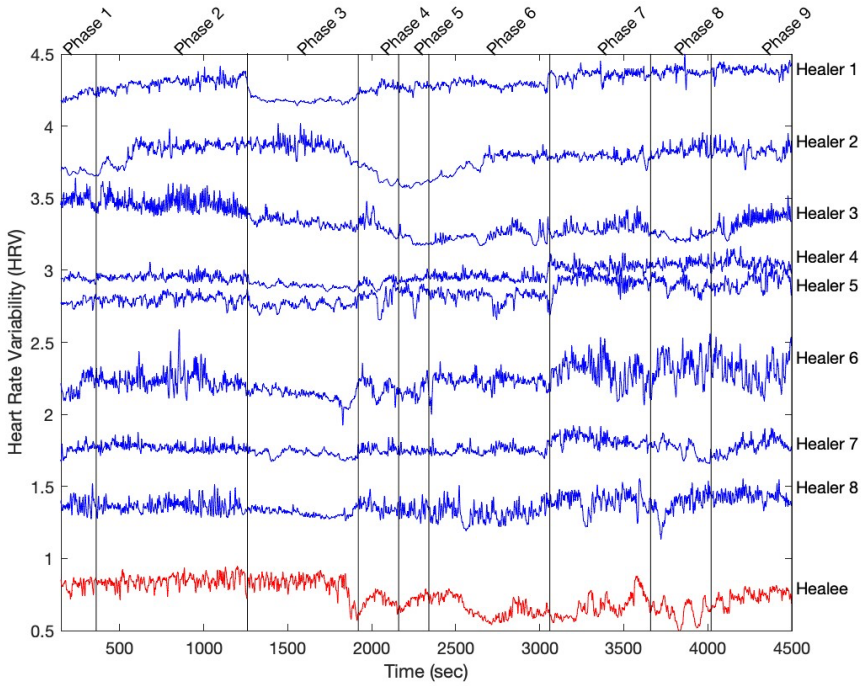


**Fig. 25.** HRV Monitoring for Eight Healers and One Healee: Blue Plots represent Healers' RR Intervals, Red Plot represents Healee's RR Intervals; Time Series Analysed Throughout the Experiment

These HRV recordings are then processed through the proposed matrix-based algorithm to obtain the H-ranks, which are subsequently plotted as time series, as shown in Fig. 26. The x-axis shows time in seconds, and the y-axis shows the amplitude of the H-rank plotted as a time series. The H-ranks of the Healers are plotted in blue, while their cumulative H-rank is plotted in black. The H-rank of the Healee is plotted in red.

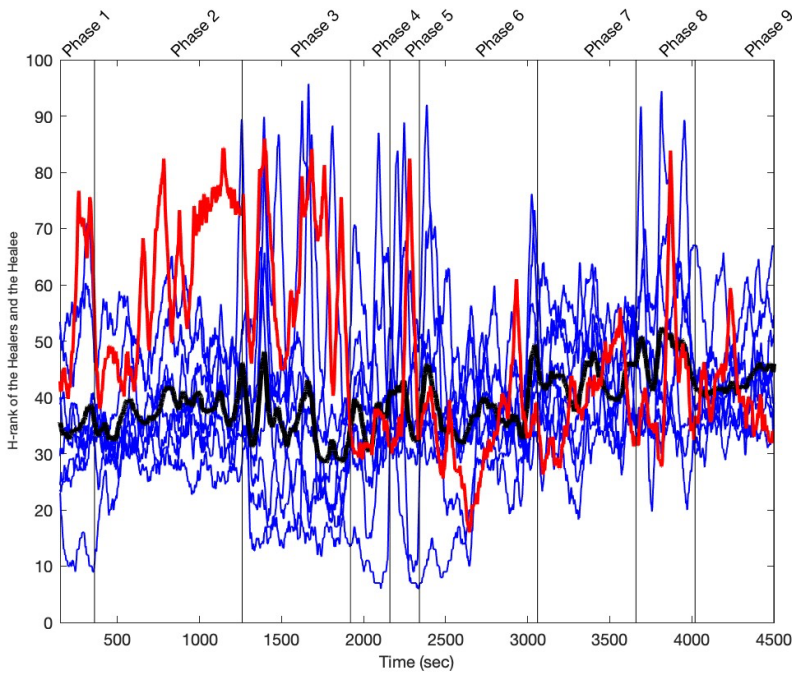


**Fig. 26.** H-Ranks Graph Throughout the Experiment: (a) H-Ranks of Eight Healers (Blue), (b) Mean H-Rank of Healers (Black), (c) H-rank of Healee (Red)

For better visualisation, special attention is focused on the average H-rank of the Healers (the plot in black) and the H-rank of the Healee (the plot in red), as shown in Fig. 27. During the first three phases of the meditation exercise, the reconstructed H-ranks of the Healers and the Healee exhibit distinctive patterns in their time series. As the fourth phase commences, part of the reconstructed average H-rank begins to align more closely with the reconstructed time series from the H-rank of the Healee, and this trend continues through phases four, five, and six. By phase seven, it becomes evident that the reconstructed time series for the average H-rank of the Healers is nearing full synchronisation with that of the H-rank of the Healee, marking the establishment of a connection between the Healers and the Healee. In phase eight, the convergence of both H-rank time series is achieved, indicating the synchronisation—a process referred to here as complexity matching in this study. Finally, in phase nine, which serves as the conclusion of the meditation exercise, complete synchronisation between the reconstructed H-rank time series for both groups is observed, as depicted in Fig. 27.

The coherence between the two reconstructed time series observed during specific phases of the meditation protocol signifies the synchronisation between the two groups during the meditation activity. This proves the effectiveness of the proposed algorithm in retrieving a sufficient number of algebraic components from the HRV, which are needed to reconstruct the H-ranks of both Healers and the Healee.

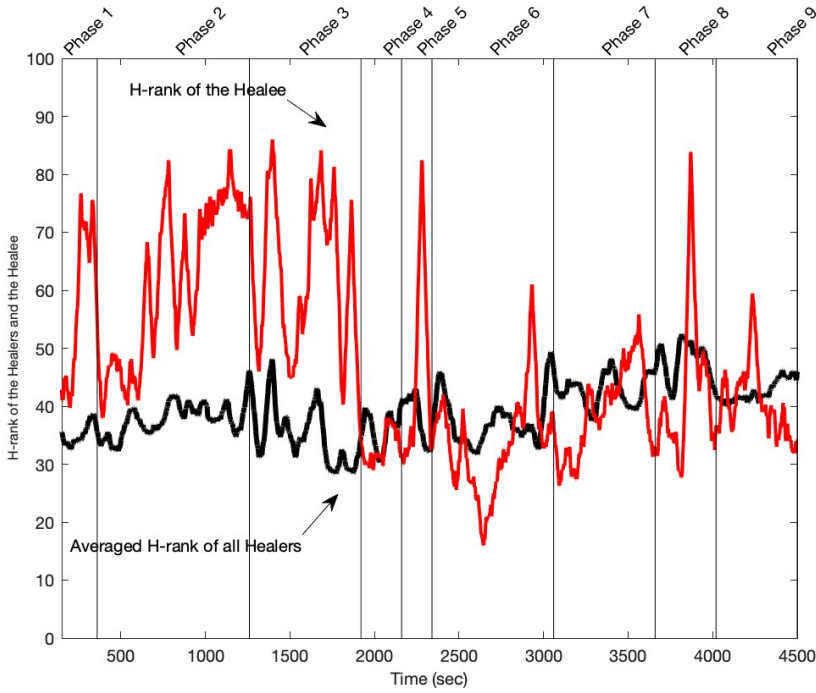


**Fig. 27.** H-Ranks Graph for Participants: (a) Mean H-Ranks of Eight Healers (Black), (b) Healee's H-Ranks (Red)

An effective visualisation technique is employed to illustrate synchronisation patterns across the distinct phases of the meditation experiment. A two-dimensional state space visualisation is used to plot the embedded attractors for the averaged H-rank values of the Healers and the Healee. By examining the geometric area covered by the data points in the trajectory matrix within the state space, one can visualise the H-rank time series in the embedded attractors. To determine the area covered by the data points, the maximum time lag value is set to one hundred, i.e. ( $\tau = 1, 2, 3, \dots$ ), where  $\tau_{max} = 100$ . The embedded attractors are generated using the values from the H-ranks and the SVD of the Healers and the Healee. This approach reveals phase-wise changes in the data points for both the Healers and the Healee, providing insights into their synchronisation dynamics during the meditation. As illustrated in Fig. 28, the two-dimensional embedded attractors for the Healers and the Healee are plotted. The black attractors represent the phase state of the average H-ranks of the Healers, while the red attractor represents the phase state of the Healee. In the first three phases of the meditation exercise, the attractors are positioned within their respective vicinities. As the meditation progresses through the fourth, fifth, and sixth phases, the red attractor gradually moves closer to the black attractor. In the final three phases, the seventh, eighth, and ninth, the two attractors are fully merged. These phases correspond to the period when the synchronisation between the reconstructed H-ranks of both the Healers and the Healee is observed, and this is also observed through the convergence of the attractors (see Fig. 28).

To understand the complex dynamics between the Healers and the Healee during the meditation activity, an analogy to the doctor-patient relationship can be used. Much like a doctor's reassuring feedback, which can provide a patient with a sense of calm, the interaction between the healer and the Healee during the meditation establishes a synchronising connection, too. This shared connection fosters coherence in the HRV, as demonstrated in the alignment of the reconstructed H-ranks over the different phases of the meditation activity. Research also indicates that such reassurance from a doctor can reduce patient anxiety and enhance overall well-being [144, 145]. In parallel, during the meditation, as the Healers' and the Healee's HRVs start to synchronise, this shared physiological rhythm may mirror the psychological comfort patients often experience when receiving empathic, positive feedback from healthcare providers [146] [147, 148]. This synchronisation phenomenon is referred to as complexity matching in this study.

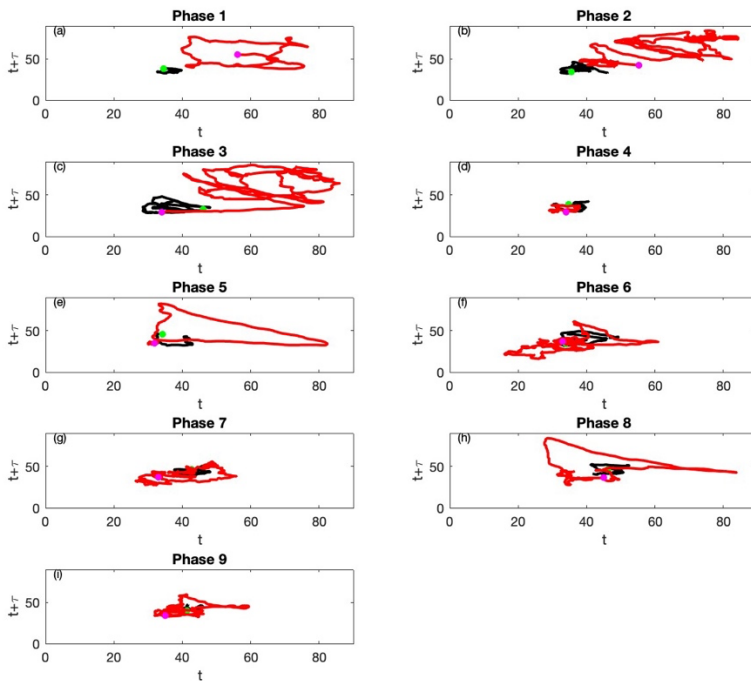


**Fig. 28.** Embedded Attractors and Phase Plane Representation: Nine Trajectories for 4,500 Seconds (75 minutes); Red for Healee (Starting at the Magenta Circle), Black for Healers (Starting at the Green Circle)

Another objective of the study is to perform statistical computations on the HRV data to corroborate the findings of the matrix-based H-rank algorithm. To achieve this, a box plot representation is utilised to determine key metrics, including the mean ( $\mu$ ) of the HRV for the eight Healers and the Healee, the standard deviation ( $\sigma$ ) of the two groups, and the 25<sup>th</sup> and 75<sup>th</sup> percentiles, as presented in Table 15. These metrics are calculated for each of the nine phases of the meditation exercises, and the corresponding box plots are depicted for each phase in Fig. 29. The black box plots

represent the statistical data for the average HRV of the eight Healers, and the red box plots represent the statistical data for the Healee. Two hypotheses are formulated to determine the synchronisation between the groups. To test the following two hypotheses, a framework is established for comparing the means of the averaged H-rank of the Healers and the Healee across different phases of the meditation exercise: Null Hypothesis (H1): The means of the averaged H-rank of the Healers and the Healee are equal. Alternate Hypothesis (H2): The means of the averaged H-rank of the Healers and the Healee are not equal. The condition used to test these hypotheses involves comparing the lower limit of the Healee's mean ( $\mu_B - \sigma_B$ ), where the 25<sup>th</sup> percentile is the ( $\mu_B$ ) and the upper limit of the Healers' mean ( $\mu_A - \sigma_A$ ), with the 75<sup>th</sup> percentile ( $\mu_A$ ) across different phases. It is observed that during the first four phases of the meditation exercises, the statistical condition does not hold true, leading to the rejection of the null hypothesis (H1). However, from phases five to nine, the proposed statistical condition holds true, leading to the acceptance of the alternate hypothesis (H2), as tabulated in Table 16 and also illustrated in Fig. 29.

**Table 15.** Statistical Metrics of HRV Data Across Nine Phases of Meditation

Phases	Mean ( $\mu$ )		Standard deviation ( $\sigma$ )		Upper limit ( $u_A$ )	Lower limit ( $u_B$ )
	Healers A	Healee B	Healers A	Healee B	75 <sup>th</sup> Percentile of the Healers (A)	25 <sup>th</sup> Percentile of the Healee (B)
1 <sup>st</sup>	35.82	57.18	1.97	11.82	37.77	44.85
2 <sup>nd</sup>	37.71	61.45	2.62	13.26	39.55	48
3 <sup>rd</sup>	35.12	62.44	4.99	12.78	38.21	51.28
4 <sup>th</sup>	36.01	33.03	2.96	2.70	38.54	31
5 <sup>th</sup>	38.19	46.49	3.90	16.45	41.33	32.71
6 <sup>th</sup>	37.56	33.50	4.14	8.52	39.21	27.28
7 <sup>th</sup>	42.75	9.11	2.62	7.45	44.87	32.57
8 <sup>th</sup>	47.75	43.01	3.19	12.82	50.26	34.42
9 <sup>th</sup>	42.54	40.71	1.80	6.11	44.51	36

**Table 16.** Statistical Conditions Across Meditation Phases

Phases	( $u_B - \sigma_B$ )	( $u_A + \sigma_A$ )	Statistical condition ( $u_B - \sigma_B$ ) > $u_B$ & ( $u_A + \sigma_A$ ) < $u_A$	Outcome
1 <sup>st</sup>	37.79	45.36	$37.79 > 44.85$ & $45.36 < 37.77$	Condition is not satisfied
2 <sup>nd</sup>	40.33	48.19	$40.33 > 48$ & $48.19 < 39.55$	Condition is not satisfied
3 <sup>rd</sup>	40.11	49.66	$40.11 > 51.28$ & $49.66 < 38.21$	Condition is not satisfied
4 <sup>th</sup>	38.97	30.33	$38.97 > 38.54$ & $30.33 < 31$	Condition is not satisfied



5 <sup>th</sup>	42.08	30.04	$42.08 > 32.71 \text{ \& } 30.04 < 41.33$	Condition is Satisfied
6 <sup>th</sup>	41.70	24.98	$41.70 > 27.28 \text{ \& } 24.98 < 39.21$	Condition is Satisfied
7 <sup>th</sup>	45.36	31.66	$45.36 > 32.57 \text{ \& } 31.66 < 44.87$	Condition is Satisfied
8 <sup>th</sup>	50.94	30.20	$50.94 > 34.42 \text{ \& } 30.20 < 50.26$	Condition is Satisfied
9 <sup>th</sup>	44.34	34.60	$44.34 > 36 \text{ \& } 34.60 < 44.51$	Condition is Satisfied

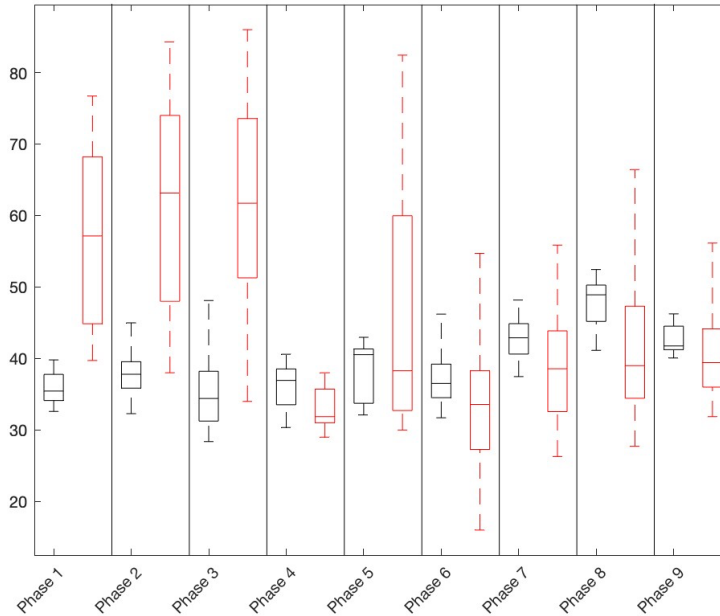


**Fig. 29.** Statistical Analysis of H-Rank: Box Plots for Nine Experiment Phases. The Red Box Plots Represent the Healee and the Black Box Plots Represents the Healers

The Hankel matrix-based algorithm, phase space representation of H-ranks, and statistical measures collectively demonstrate the synchronisation between the two groups, which began to occur in phases four, five, and six, culminating in complete synchronisation from phases seven to nine. This study also emphasises employing another technique to analyse HRV data and visualise synchronisation. The objective is to determine whether other methods can also reveal synchronisation. For this purpose, permutation entropy (PE) is utilised to evaluate the HRV data for the two groups. PE has been extensively used in research studies for assessing time-series complexity due to its sensitivity to subtle changes in signal patterns [149].

In Fig. 30, the HRVs of the Healers (plotted in blue) and the Healee (plotted in red) are shown. Additionally, the average HRV of the eight Healers is plotted in black. The x-axis represents the time stamp in seconds, while the y-axis indicates the

amplitude of the HRVs computed using the PE algorithm. It is evident that the PE approach did not demonstrate synchronisation between the two groups, unlike the Hankel matrix-based approach. This finding suggests that analysing complex time series, such as HRV, requires an advanced computational algorithm to handle the signal's complexities. For instance, the Hankel matrix-based approach revealed synchronisation between the two groups during the meditation exercise, which only occurred in the last few phases of the healing protocol. These findings are also corroborated by state space analysis and statistical routines. Although PE is an effective algorithm technique for analysing real-time complex time series, in this study, it failed to provide the desired outcomes.

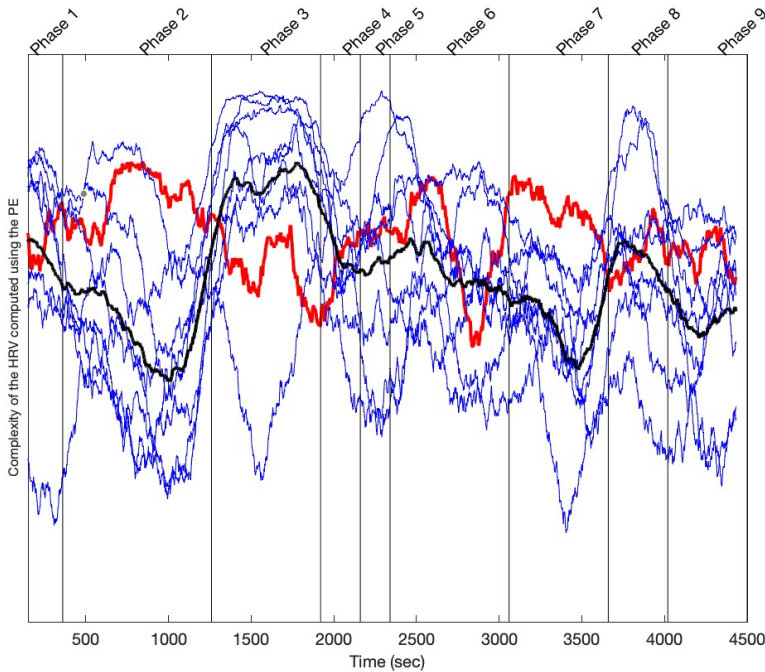


**Fig. 30** HRV Complexity via Permutation Entropy (PE)

### **Conclusive Insights from the Study**

The Hankel matrix-based algorithm was employed to analyse the HRV signal to understand the complexity matching between the Healers and the Healee during the guided meditation protocol. This computational approach provided validation of the complex interactions occurring within the group, highlighting how synchronised physiological states develop through shared meditation practices occurring during specific phases of the protocol. Detecting these synchronisation processes is challenging, especially in complex activities such as meditation. Additionally, the state space visualisation technique was adopted to illustrate the synchronisation phenomenon between the two groups. Statistical techniques were also utilised to corroborate the findings. However, the permutation entropy method did not yield sufficient outcomes for analysing the complexity matching between the two groups.

This study is significant, as it contributes to clinical diagnostics by detecting synchronisation phenomena that are otherwise difficult to observe.

## 4. LIMITATIONS AND FUTURE RESEARCH

This study, while providing significant insights, is not without its limitations. The primary limitation lies in the modest size of the dataset used. Although the analysis incorporated diverse ECG datasets, such as those recorded during resting conditions and physical activity, the relatively small sample size is one of the limitations. Additionally, some datasets included only male or female participants, which limits the ability to draw conclusions about gender-specific cardiovascular dynamics.

Future research should prioritise addressing these limitations by expanding the dataset to include a larger and more balanced population sample comprising both male and female participants. This would enhance the statistical robustness of the findings and allow for more nuanced insights into gender-specific variations in cardiovascular responses.

Moreover, exploring the efficacy of other algorithms for ECG analysis presents a promising avenue for future work. By applying and comparing alternative matrix-based and statistical algorithms, future studies could evaluate their relative performance in detecting atrial fibrillation episodes, complexity synchronisation, and other phenomena observed in this study. This could further refine the understanding of cardiovascular dynamics during stress and recovery phases and in synchronisation contexts such as meditation exercises.

Incorporating these improvements would provide a stronger foundation for advancing cardiovascular diagnostics and the broader application of mathematical and statistical tools in time-series analysis.

## 5. CONCLUSIONS

1. Subtle cardiovascular variations can be observed between individuals with normal and high arterial blood pressure during the stress test, especially during the load phase of the exercise. The second-order PMLD matrix architecture facilitates understanding of these subtle processes, known as the collapse of complexity, and allows for their quantification and visualisation. The PMLD matrix-based architecture has proven effective in analysing the algebraic interrelationships between ECG parameters, such as the RR inter-beat interval and the duration of the JT wave, thereby fulfilling the objective of early detection of cardiovascular processes like the collapse of complexity.
2. The algebraic relationships between the ECG parameters during the stress test provide valuable insights into the significant phenomena, including the collapse of complexity, self-organisation of the cardiovascular system, and the velocity of adaptation. These findings are derived from analysing the behaviour of ECG parameters, such as the RR inter-beat interval and the duration of JT wave, during both the load and recovery phases, thereby supporting the objective of understanding cardiovascular behaviour during the physical activity. The second-order time-delayed perfect matrices of the Lagrange differences algorithm, in corroboration with the statistical techniques, help to extract, analyse, and visualise these complex processes.
3. The comparison among the three matrices—PMF, SMF1, and SMF2—demonstrated that the PMF outperforms the other matrix-based algorithms. This is due to its adherence to the criteria for being the most optimal matrix for ECG analysis, as well as its flexibility in terms of size, allowing for further extension in ECG analysis.
4. The applicability and expandability of the PMF have been demonstrated to be effective, enabling the analysis, evaluation, and detection of atrial fibrillation episodes through extensive mathematical and statistical analysis of five ECG parameters (RR, JT, QRS, AP, and DP).
5. The Hankel matrix-based algorithm has proven to be a useful tool for detecting the complexity synchronisation occurring between the two groups during the healing meditation exercise. Psychological synchronisation is observed to occur during certain stages of the exercise, which is both observable and quantifiable using specific statistical techniques and state-space visualisation.

## 6. SANTRAUKA

### **Tyrimo objektas**

Tyrimo objektas – matricinių algoritmų, skirtų EKG parametrų analizuoti ir jų algebriniams ryšiams tirti, kūrimas bei taikymas trumpalaikiams širdies ir kraujagyslių sistemos svyravimams aptikti

### **Tyrimo tikslas**

Tyrimo tikslas – pasiūlyti ir patvirtinti matriciniais metodais pagrįstus EKG laiko eilučių analizės algoritmus bei sukurti mašininio mokymosi modelį, naudojant intelektualius indikatorius, reikalingus ankstyvai įvairių širdies ir kraujagyslių ligų diagnostikai.

### **Pateikta gynybai**

Ši disertacija pristato matricinius algoritmus, skirtus EKG parametrų algebriniams ryšiams analizuoti ir vertinti. Šiam tikslui yra pasiūlyti šie algoritmai:

1. Lagrange skirtumų tobulosios matricos: nors šios matricos jau buvo anksčiau analizuotos antrojo laipsnio matriciai, naudojant tik du EKG parametrus, dabar jų taikymas išplėstas į aukštesnio laipsnio matricias. Tai leidžia pagerinti EKG analizę.
2. Dvi kitos matricinės architektūros, kurios taip pat analizuojamos EKG analizei. Jų veikimas vertinamas pagal tai, kaip jos atitinka PMLD matricių kriterijus, siekiant užtikrinti, kad šios matricos gali būti laikomos optimaliomis. Kai šios matricinės architektūros patvirtinamos kaip atitinkančios PMLD taisykles, jos toliau vertinamos pagal jų išplečiamumą, įskaitant galimybę padidinti matricos dydį, prisitaikyti prie skirtingų laisvės laipsnių ir palaikyti didesnes dimensijas.
3. Antrojo laipsnio laiko uždelstas PMLD matricinis algoritmas: šis matricinis algoritmas siūlo unikalią PMLD matricinės architektūros reprezentaciją, specialiai pritaikytą EKG analizei.
4. Hankelio matricinis algoritmas: šioje disertacijoje šis matricinis algoritmas pritaikomas sudėtingumo derinimo reiškiniui identifikuoti.

### **Tikslai**

1. Ištirti algebrinius tarpusavio ryšius tarp EKG parametrų (RR, JT), siekiant ankstyvosios širdies ir kraujagyslių procesų detekcijos (žinomos kaip sudėtingumo žlugimas, kuris įvyksta apkrovos fazės pabaigoje atliekant streso testą), taikant antrojo laipsnio PMLD matricinį algoritmą kartu su kitais statistinės analizės metodais.
2. Išnagrinėti algebrinius tarpusavio ryšius tarp EKG parametrų (RR, JT), siekiant ankstyvosios širdies ir kraujagyslių procesų detekcijos (širdies ir kraujagyslių sistemos saviorganizacijos, vykstančios viso streso testo metu, ir

sudėtingumo žlugimo, kuris įvyksta apkrovos fazės pabaigoje atliekant streso testą), naudojant antrojo laipsnio laiko uždelstą PMLD matricinį algoritmą ir statistinės analizės metodų seką.

3. Įvertinti siūlomų PMLD matricinių algoritmų veikimą, palyginant juos su dviem kitais matriciniais algoritmais (SMF1 ir SMF2), atliekant statinę EKG analizę prieširdžių virpėjimo epizodams aptikti, nagrinėjant algebrinius tarpusavio ryšius tarp trijų EKG parametrų (RR, JT, QRS).
4. Ištirti PMLD analizės išplečiamo struktūrą prieširdžių virpėjimo epizodams aptikti, analizuojant algebrinius tarpusavio ryšius tarp penkių EKG parametrų (RR, JT, QRS, AP, DP), naudojant PMLD algoritmą ir kitas statistines skaičiavimo technikas.
5. Analizuoti RR tarpširdinių intervalų dinamiką, taikant Hankelio matricinį metodą, siekiant aptikti sudėtingumo derinimo reiškinį vedamos meditacijos metu.

### **Programinė įranga**

Visų algoritmų kūrimui ir skaičiavimams šiame darbe buvo pasirinkta MATLAB programinė įranga.

### **Darbo rezultatų aprobavimas**

Ši disertacija paremta keturiomis mokslinėmis publikacijomis ir vienu išsamiau skaičiavimo darbu, atliktu su ŠSD duomenimis. Keturi straipsniai buvo paskelbti aukšto poveikio veiksnio (Q1 ir Q2) žurnaluose, kurie yra indeksuojami „Web of Science“ (WoS) duomenų bazėje. Darbo rezultatai taip pat buvo pristatyti dviejose konferencijose.

### **Disertacijos apimtis ir struktūra**

Ši daktaro disertacija susideda iš įvadinės dalies, keturių pagrindinių skyrių, kiekvieno skyriaus išvadų, bendros disertacijos išvados, darbo apribojimų ir ateities tyrimų perspektyvų, bibliografijos bei publikacijų sąrašo.

Disertacija apima 142 puslapius, kuriuose pateikiamos 30 iliustracijų ir 16 lentelių. Joje cituojami 149 šaltiniai.

## 6.1 Įvadas

Širdies ir kraujagyslių ligos visame pasaulyje yra pagrindinė mirtingumo ir sergamumo priežastis [15], pabrėžiant būtinybę anksti nustatyti ir veiksmingai stebėti šias ligas. Sudėtingas širdies ir kraujagyslių sistemos funkcionalumas itin apsunkina šių ligų diagnozę, ypač tuo atveju, kai norima išvelgti trumpalaikius svyravimus, atsirandančius fizinės veiklos, mankštos ar net ramybės būsenos metu. Įprasti analizės metodai dažnai praleidžia šiuos subtilius skirtumus, kas dar labiau pabrėžia tradicinių diagnostikos metodų apribojimus. EKG įrašymo metu fiksuojami svarbūs EKG parametrai, tokie kaip P bangos trukmė, QRS komplekso trukmė, P bangos amplitudė, T banga ir RR intervalas. Kiekvienas EKG parametras atitinka konkrečius širdies ciklo įvykius. Šioje disertacijoje ši svarba pabrėžiama daugiausia dėmesio skiriant EKG parametrų tarpusavio ryšių analizei naudojant pažangius matricinius metodus. Nagrinėjant ramybės būsenoje bei fizinio aktyvumo metu užfiksuotus EKG įrašus, šiuo darbu siekiama pateikti gilesnes įžvalgas apie širdies ir kraujagyslių funkciją bei sveikatą, galiausiai atveriant kelią sumaniai automatinei diagnostikai.



## 6.2 Sudėtingos laiko eilučių analizės matematinių metodų tyrinėjimas ir išplėtimas

### Konfigūruojama PMLD struktūra patobulintai EKG analizei

Kaip buvo aptarta ankstesniame skyriuje, Lagranžo skirtumų tobulosios matricos (PMLD) sėkmingai buvo taikomos EKG signalų analizėje [13, 53]. Ypač pastebimas ir dar nepakankamai išnagrinėtas PMLD aspektas yra jos matricos konfigūracijos lankstumas, kuris suteikia unikalų laisvės laipsnį, leidžiantį keisti matricių elementus, nekeičiant matricos didžiausios absoliučios tikrinės reikšmės [13]. Ši savybė yra ypač reikšminga analizuojant sudėtingus fiziologinius signalus, nes skirtingos konfigūracijos gali atskleisti skirtingus pagrindinės dinamikos bruožus. Pavyzdžiui, panagrinėkime antros eilės kvadratinę matricą, gautą iš dviejų sinchroniškai įrašytų laiko eilučių ( $x_n: n = 0,1,2,3 \dots$ ) ir ( $y_n: n = 0,1,2,3 \dots$ ). Atsižvelgiant į šešis iš anksto nustatytus kriterijus, apibrėžiančius tobulą Lagranžo matricą [13], yra keturios skirtingos konfigūracijos, kuriomis šie elementai gali būti išdėstyti. Kiekviena konfigūracija atspindi skirtingą matricos struktūrinį išdėstymą, suteikia unikalų požiūrį interpretuojant duomenis

$$A_1 = \begin{bmatrix} x_n & x_{n+1} - y_{n+1} \\ x_{n-1} - y_{n-1} & y_n \end{bmatrix}; \quad (57)$$

$$A_2 = \begin{bmatrix} x_n & y_{n+1} - x_{n+1} \\ y_{n-1} - x_{n-1} & y_n \end{bmatrix}; \quad (58)$$

$$A_3 = \begin{bmatrix} x_n & x_{n+1} - y_{n+1} \\ y_{n-1} - x_{n-1} & y_n \end{bmatrix}; \quad (59)$$

$$A_4 = \begin{bmatrix} x_n & y_{n+1} - x_{n+1} \\ x_{n-1} - y_{n-1} & y_n \end{bmatrix}; \quad (60)$$

Nors šios konfigūracijos gali atrodyti tik nežymiai besiskiriančios, jų įtaka analizei gali būti labai reikšminga. Konkretios matricos struktūros pasirinkimas gali lemti signalo dinamikos interpretacijos skirtumus, taigi ir analizės rezultatus. Pavyzdžiui, tam tikros konfigūracijos pasirinkimas gali padidinti analizės jautrumą. Šis konfigūracijos lankstumas taip pat atveria naujas galimybes pritaikyti PMLD metodiką konkreitiems tyrimams. Atsižvelgdami į tyrimo tikslus, mokslininkai gali pasirinkti konfigūraciją, kuri geriausiai atitinka jų analitinius poreikius. Tai gali apimti kelis konfigūracijos variantus, siekiant nustatyti, kuris iš jų duoda informatyviausius rezultatus, arba naujų kriterijų kūrimą optimaliai konfigūracijai parinkti, atsižvelgiant į analizuojamų laiko eilučių savybes.

### PMLD jautrumo ir kintamumo gerinimas naudojant aukštesnės laipsnio matricos išplėtimą

Kvadratinės matricos eilė yra esminis veiksnys norint tobulinti EKG duomenų analizę, ypač siekiant pagerinti rezultatų jautrumą ir kintamumą. Didinant matricos eilę, praturtinama analitinė sistema, leidžianti identifikuoti sudėtingesnius ryšius ir subtilias duomenų savybes. Šis procesas gali būti suprantamas kaip mašininio

mokymosi algoritmas su papildomais sluoksniais arba požymiais, kuris leidžia siūlomam modeliui apdoroti ir interpretuoti sudėtingesnius dėsningumus. Svarbu pažymėti, kad terminas „mašininio mokymo modelis“ čia reiškia konkrečius siūlomus skaičiavimo metodus, kurie imituoja tradicinius mašininio mokymosi modelius tikslumo atžvilgiu. Tai atsiskleidžia jų gebėjime generuoti efektyvesnius rezultatus, kai į algoritmą įtraukiami papildomi duomenys. Tačiau svarbu pabrėžti, kad šie modeliai skiriasi nuo įprastinių mašininio mokymosi metodų, tokių kaip prižiūravimo mokymosi metodai (pvz., sprendimų medžiai, atraminių vektorių klasifikatoriai ir neuroniniai tinklai) bei neprižiūravimo mokymosi metodai (pvz., klasterizavimo algoritmai, tokie kaip k-vidurkių ir dimensijų mažinimo metodai, tokie kaip pagrindinių komponenčių analizė). Kvadratinės matricos eilės padidėjimas lemia didesnę jautrumą, o tai reiškia, kad matrica gali efektyviau aptikti subtilius EKG signalų pokyčius [106]. Be to, aukštesnės eilės matricos prisideda prie didesnio analizės kintamumo. Kintamumas čia reiškia duomenų taškų sklaidą pagal Gauso pasiskirstymą (šios problemos bus aptariamose vėliau disertacijoje). Šis platesnis kintamumas yra svarbus norint atskirti skirtingas klases ir pagerinti tiriamųjų klasifikavimo tikslumą. Atsižvelgdamos į platesnį duomenų pasiskirstymą, aukštesnės eilės matricos padeda geriau atpažinti ir apibūdinti įvairias fiziologines būsenas, o tai yra esminis veiksnys siekiant tiksliai diagnozuoti.

#### **Lyginamoji analizė: PMLD ir SMF1 bei SMF2**

Navickas ir kt. [107], pristatė dvi matricos architektūras, skirtas ryšiams tarp sudėtingų laiko eilučių nagrinėti. Pavyzdžiui, jei turimos trys laiko eilutės ( $x_n: n = 0,1,2,3 \dots$ ), ( $y_n: n = 0,1,2,3 \dots$ ), ir ( $z_n: n = 0,1,2,3 \dots$ ), jos gali būti integruotos į PMLD sistemą taip:

$$\begin{bmatrix} 2x_n & x_{n+1} - y_{n+1} & x_{n+1} - z_{n+1} \\ y_{n-1} - x_{n-1} & 2y_n & y_{n+1} - z_{n+1} \\ z_{n-1} - x_{n-1} & z_{n-1} - y_{n-1} & 2z_n \end{bmatrix}; \quad (61)$$

Atkreipkite dėmesį, kad visi šeši PMLD reikalavimai taip pat taikomi (34). Navickas ir kt. [107] taip pat pasiūlė kitą matricos architektūrą sudėtingų laiko eilučių analizei. Ji žymima SMF2 ir yra tokia:

$$\begin{bmatrix} x_n + z_n & x_{n+1} - y_{n+1} & z_{n+1} - x_{n+1} \\ x_{n-1} - y_{n-1} & 2y_n & y_{n+1} - z_{n+1} \\ z_{n-1} - x_{n-1} & y_{n-1} - z_{n-1} & z_n + x_n \end{bmatrix} \quad (62)$$

Pagrindinis skirtumas tarp SMF1 (61) ir SMF2 (62) yra pagrindinės įstrižinės elementuose. Skirtingai nei SMF1, leksikografinė pusiausvyra (62) neišlaikoma. Be to, SMF1 matricos eilė gali būti padidinta į aukštesnę, tačiau padauginus nulinės eilės išvestinius elementus iš skaliaro, didesnio už vienetą, iš tikrųjų sumažėja jos gebėjimas aptikti tuos subtilius analizuojamų signalų pokyčius, kurie minimi [13]. Kita vertus, SMF2 architektūros negalima išplėsti iki aukštesnių eilių, nes ji neatitinka būtinų matricos išplečiamumo sąlygų, kaip paaiškinta [13]. Jei matricos išplėtimas nėra būtinas, pavyzdžiui, kai analizei naudojami tik du širdies intervalai, tuomet siūlomos matricos architektūros yra tinkamos šiai užduočiai. Kaip pabrėžta [75], nė vienas algoritmas nėra visapusiškai pranašesnis, pasirinkimas priklauso nuo

konkrečių analitinių poreikių. Todėl geriausias būdas yra įvertinti visas matricos architektūras ir pasirinkti tą, kuri veikia geriausiai.

### **Antros eilės laiko uždelsto modelio matricos daugiamačiams laiko eilučių analizei**

Norėdami apskaičiuoti laiko delsos šablonus tarp laiko eilučių  $(x)$  ir  $(y)$ , apibrėžiame indeksų rinkinį  $I = \{k - R, k - R + 1, \dots, k + R\}$ , čia  $R$  – vidurkinimo spindulys. Laiko eilutė  $(y)$  yra paslenkama į dešinę  $\delta$  laiko žingsnių atžvilgiu  $(x)$ . Vidutinis skirtumas tarp atitinkamų laiko eilučių  $(x)$  ir  $(y)$  elementų indeksų rinkinyje  $I$ , apskaičiuojamas taip:

$$D(k, \delta, R) = \frac{1}{2R+1} \sum_{j \in I} \alpha_j \cdot (x_j - y_{j+\delta}); \quad (63)$$

čia  $\alpha_j$  yra svoriniai koeficientai, kurių skirstinys yra Gauso su vidurkiu  $j = k$ , o  $k$  yra dabartinis laiko momentas. Koeficientų  $\alpha_j$  Gauso tankio funkcijos pavidalas:

$$f(t) = \frac{1}{\beta} e^{-\frac{1}{2} \left( \frac{t-k}{\sigma} \right)^2}; \quad (64)$$

čia  $\beta$  normuoja koeficientus taip, kad  $\sum_{j \in I} \alpha_j = 1$ , o  $\sigma$  kontroliuoja Gauso skirstinio sklaidą. Didėjant  $\sigma$ , koeficientų  $\alpha_j$  skirstinys artėja prie tolygaus pasiskirstymo aibėje  $I$ . Mažėjant  $\sigma$  iki nulio,  $\alpha_j$  telkiasi apie vidurkio tašką  $k$ . Pateiktiems skaičiavimams naudojami  $R = 2$  ir  $\sigma = 20$ . Šie parametrai standartizuoja vidurkinimo spindulį ir Gauso pasiskirstymo sklaidą, jie taikomi vėlesniuose analizės etapuose. Ši metodika sudaro tvirtą pagrindą kiekybiškai įvertinti laikines sąsajas ir priklausomybes tarp laiko eilučių  $(x)$  ir  $(y)$  naudojant svertinį vidurkį, užtikrinant jautrumą vietiniams pokyčiams ir sistemingiems laiko eilučių duomenų pokyčiams laikui bėgant. Siūlomas algoritmas skaičiuoja laiko vėlavimo dėsningumus tarp dviejų laiko eilučių  $(x)$  ir  $(y)$ , ir naudojamas RR intervalo bei JT bangos trukmės algebriniams ryšiams analizuoti streso testo metu. Šis algoritmas pereina per kiekvieną laiko momentą  $k$  ir apskaičiuoja vidutinius skirtumus tarp  $(x)$  segmentų ir atitinkamų laiko vėlavimu perkeltų  $(y)$ , naudojant nurodytą spindulį  $R$  ir skirtingus laiko vėlavimus. Šiems skirtumams taikomi Gauso tipo pasiskirstymo su vidurkiu  $k$  svoriai, pabrėžiant laiko suderinamumą tarp dviejų laiko eilučių. Gauti laiko delsos dėsningumų rezultatai saugomi iš anksto apibrėžtoje matricos architektūroje. Šis skaičiavimo metodas padeda analizuoti EKG parametrus, siekiant suprasti sudėtingus ryšius tarp RR ir JT intervalų bei jų adaptacijas širdies ir kraujagyslių sistemoje streso testo metu.

### **Klasifikacijos ir sveikatos biologinių žymenų variacijos intervalų generavimo statistiniai metodai**

Šiame darbe šios statistinės analizės tikslas yra dvejopas. Pirma, tikslas yra sukurti dviejų klasių skirstinius sveikiems (H) ir sergantiems (U), asmenims, remiantis tais pasiskirstymais. Analizuojant patobulintas laiko eilutes (kurios apdorojamos naudojant matricos algoritmą), įvairūs statistiniai metodai gali pasiūlyti vertingų įžvalgų. Pagrindinis šios analizės aspektas yra pagrindinių patobulintų laiko eilučių tendencijų ir sklaidos apibendrinimas. Aprašomoji statistika, tokia kaip vidurkis ( $\mu$ ), dispersija ( $\sigma^2$ ) arba standartinis nuokrypis ( $\sigma$ ) paprastai suteikia tam tikros įžvalgos. Pateiktų patobulintų laiko eilučių vidurkis yra toks:

$$\mu = \frac{1}{N} \sum_{i=1}^N z_i; \quad (65)$$

čia  $N$  reiškia bendrą stebėjimų skaičių laiko eilutėje, o  $z_i$  reiškia kiekvieną vertę patobulintoje laiko eilutėje. Panašiai dispersija, kuri matuoja duomenų sklaidą, apskaičiuojama taip:

$$\sigma^2 = \frac{1}{N} \sum_{i=1}^N (z_i - \mu)^2; \quad (66)$$

čia  $\mu$  yra laiko eilutės vidurkis, apskaičiuotas pagal (66) o  $z_i$  reiškia kiekvieną vertę patobulintoje laiko eilutėje. Šie du pagrindiniai statistiniai rodikliai – pagrindinė duomenų tendencija ir jų sklaida – yra labai svarbūs norint suprasti patobulintų laiko eilučių elgesį. Jie suteikia įžvalgų apie tai, kaip duomenų taškai paskirstomi ir kaip jie skiriasi klasėje. Tai ypač naudinga analizuojant dvi skirtingas grupes, nes sveikų ir sergančių asmenų klasės gali turėti panašius modelius savo atitinkamose grupėse, tačiau jos turi reikšmingų skirtumų, lyginant viena su kita. Jei siekiama ieškoti normaliai paskirstytų duomenų taškų, galioja empirinė taisyklė (dažnai vadinama 68-95-99.7 taisykle). Ši taisyklė teigia, kad normaliam pasiskirstymui: apytiksliai 68% duomenų taškų patenka į vieną standartinį nuokrypį ( $\sigma$ ) aplink vidurkį ( $\mu$ ); maždaug 95% patenka į du standartinius nuokrypius ir 99.7% patenka į tris standartinius nuokrypius. Matematiškai šios taisyklės vienos sigmos dalis gali būti išreikšta taip:

$$P(\mu - \sigma \leq X \leq \mu + \sigma) \approx 0.6827; \quad (67)$$

čia  $X$  yra atsitiktinis dydis, atitinkantis normalųjį skirstinį,  $\mu$  yra skirstinio vidurkis,  $\sigma$  yra atitinkamai standartinis nuokrypis. Remiantis tuo, Gauso skirstinys (arba normalusis skirstinys) gali suteikti daugiau įžvalgų apie dviejų klasių duomenų pasiskirstymą. Gauso skirstinys yra nuolatinis tikimybių skirstinys, kuriam būdinga varpo formos kreivė, simetriška vidurkio atžvilgiu. Jis matematiškai išreiškiamas kaip:

$$f(x) = \frac{1}{\sigma\sqrt{2\pi}} e^{-\frac{(x-\mu)^2}{2\sigma^2}}; \quad (68)$$

vėlgi čia  $\mu$  yra vidurkis,  $\sigma$  yra standartinis nuokrypis ir  $x$  yra atsitiktinis dydis. Kitas svarbus statistinis matas yra Andersono ir Darlingo (AD) testas. Andersono ir Darlingo (AD) testas yra statistinis metodas, naudojamas įvertinti, ar tam tikras duomenų rinkinys atitinka normalųjį pasiskirstymą. Tai yra Kolmogorovo ir Smirnovio testo modifikacija, specialiai sukurta siekiant suteikti daugiau svorio skirstinio uodegoms. AD testas padeda nustatyti, ar transformuoti komponentai atitinka normalųjį pasiskirstymą, taip patvirtinant modelio prielaidas. Matematiškai AD testas skamba taip [117, 118]:

$$A^2 = -N - \frac{1}{N} \sum_{i=1}^N \left( (2i-1) [\ln F(Y_i) + \ln(1 - F(Y_{N+1-i}))] \right); \quad (69)$$

čia  $N$  yra imties dydis,  $F$  yra orientacinio skirstinio kaupiamoji pasiskirstymo funkcija (CDF), o  $Y_i$  yra sutvarkyti duomenų taškai.

Naudojant paprastą statistiką funkcijų patobulintose laiko eilutėse, gaunami kiekvienos laiko eilutės duomenų taškai, kurie vėliau naudojami kuriant dviejų klasių skirstinius. Šie pasiskirstymai palengvina variacijos intervalo generavimą naudojant vienos sigmos taisyklę, kuri sudaro siūlomos klasifikavimo technikos pagrindą. Nustačius klasifikavimo modelį, tiriamojo (vadinamo (R)) EKG galima įvertinti pagal šią klasifikaciją. Pirmiausia tiriamojo EKG apdorojama naudojant matricos algoritmą,

tada sukuriami patobulinta laiko eilutė. Panašūs statistiniai metodai taikomi norint išgauti šios laiko eilutės ( $R$ ) duomenų tašką (dispersijos reikšmę). Tada ( $R$ ) vertė įvertinama pagal tris skirtingas sąlygas, atitinkamai apskaičiuojant interpoliacijos koeficientą ( $I$ ). Pirmoji sąlyga apibrėžia sveikų žmonių klasę atitinkančio rodiklio lygtį, nustatydama atskaitos tašką klasifikacijai pagal kitas sveikatos būklės kategorijas.

Sąlyga Nr. 1: sveikųjų klasės rodiklio lygtis yra tokia:

$$R \leq (\mu_h - \sigma_h) \quad (I = 0); \quad (70)$$

Sąlyga Nr. 2: rašoma sergančiųjų klasės rodiklio lygtis:

$$R \geq (\mu_u + \sigma_u) \quad (I = 1); \quad (71)$$

Sąlyga Nr. 3: Nuskaitoma tarpinės klasės rodiklio lygtis:

$$(\mu_h - \sigma_h) \leq R \leq (\mu_u + \sigma_u), \text{ kai } I = \frac{R - (\mu_h - \sigma_h)}{(\mu_u + \sigma_u) - (\mu_h - \sigma_h)}; \quad (72)$$

Šios sąlygos taikomos klasifikuojant ( $R$ ) į sveiką arba sergančiojo kategoriją. Pavyzdžiui, diagnozuojant prieširdžių virpėjimo (PV) epizodus, tiriamojo EKG pirmiausia apdorojama naudojant matricos algoritmą, o vėliau apdorojama per visą statistinę tvarką, kad būtų klasifikuojama sveikas ar sergantis. Panašiai, jei tikslas yra išanalizuoti širdies ir kraujagyslių sistemos saviorganizaciją fizinio aktyvumo metu dviem klasėms, pradinis žingsnis apima EKG parametrų apskaičiavimą naudojant matricos algoritmą. Tada gaunamos nurodytos skaliarinės laiko eilutės. Po šio žingsnio apskaičiuojami pagrindiniai parametrai, tokie kaip prisitaikymo greitis (žymima  $A$ ) ir modifikuotas prisitaikymo greitis (žymimas  $B$ ) ir kiti rodikliai. Parametrai  $A$  ir  $B$  naudojami apskaičiuojant pirmąjį sveikatos rodiklį, vadinamą alfa ( $\alpha$ ). Pirmiausia apskaičiuojamas skirtumas tarp  $A$  ir  $B$ :

$$X = \frac{A-B}{A} \times 100\%; \quad (73)$$

Tada sveikatos rodiklis alfa ( $\alpha$ ) išvedamas normalizuojant ( $X$ ) visoje klasėje:

$$\alpha = \frac{X - \min(X)}{\max(X) - \min(X)}; \quad (74)$$

Panašiai kitas sveikatos rodiklis beta ( $\beta$ ) gali būti apskaičiuotas analizuojant parametro signalo kintamumą skirtingose fizinio krūvio fazėse, naudojant Šano bangelių analizę. Priklausomai nuo tyrimo tikslų, signalas gali būti padalytas į tris segmentus (pvz.  $C_1, C_2, C_3$ ), tuomet apskaičiuojamos tų segmentų vidutinės reikšmės ( $\mu_{C_1}, \mu_{C_2}, \mu_{C_3}$ ). Šiame kontekste disertacijos autorius pasiūlė padalyti signalą į tris segmentus ir kiekviename iš jų jį interpoliuoti kvadratine lygtimi  $y = ax^2 + bx + c$ . Tam svarbu nustatyti nuokrypį tarp vidurinio segmento vidurkio  $\mu_{C_2}$  ir kraštinių segmentų vidurkių  $\mu_{C_1}$  bei  $\mu_{C_3}$ . Šis segmentų nuokrypis žymimas kaip  $d$  ir išreiškiamas taip:

$$d = \frac{\mu_{C_1} + \mu_{C_3}}{2} - \mu_{C_2}; \quad (75)$$

čia  $\mu_{C_1}, \mu_{C_2}, \mu_{C_3}$  atitinkamai reiškia pirmojo, antrojo ir trečiojo segmentų vidurkį. Kitas sveikatos rodiklis  $\beta$  gali būti apibrėžtas kaip:

$$\beta = \frac{d - \min(d)}{\min(d) - \max(d)}; \quad (76)$$

Galima pastebėti, kad atliekant testavimą nepalankiausiomis sąlygomis sveikatos rodikliai alfa ir beta apibrėžia du skirtingus širdies ir kraujagyslių sistemos funkcionalumo aspektus. Šie du skirtingi aspektai atsiranda apkrovos ir atsigavimo fazėse, dėl to svarbu išsiaiškinti bendrą atsaką, arba kitais žodžiais tariant, bendrą abiejų aspektų poveikį. Taigi, bendrą asmens širdies ir kraujagyslių sistemos sveikatos būklę parodo parametras gama ( $\gamma$ ) kuris apskaičiuojamas kaip:

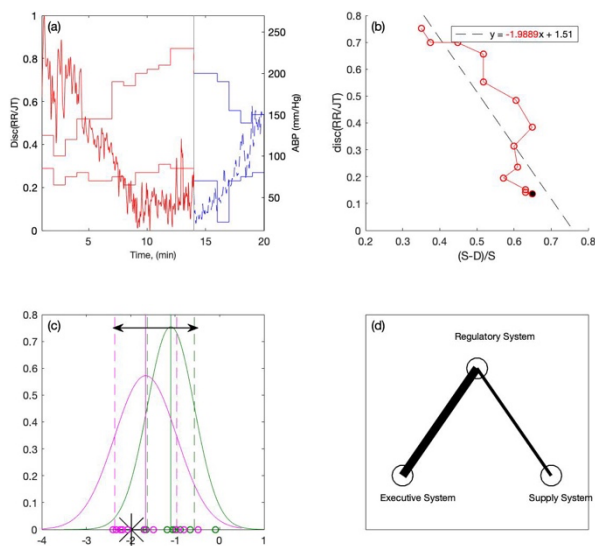
$$\gamma = \frac{\alpha + \beta}{2}; \quad (77)$$

Kitas naudingas statistinis įrankis, kurį galima panaudoti analizuojant dviejų klasių HRV duomenis, yra stačiakampė diagrama. Ši diagrama gali grafiškai pavaizduoti duomenų pasiskirstymą pagal penkių skaitinių charakteristikų suvestinę: mažiausia reikšmė, pirmasis kvartilis ( $Q_1$ ), mediana, trečiasis kvartilis ( $Q_3$ ) ir didžiausia reikšmė. Tarpkvartilinis intervalas (IQR), apibrėžtas kaip ( $Q_3 - Q_1$ ), apima 50% duomenų sklaidą abipus medianos, o duomenų taškai, esantys už  $Q_1 - 1,5 \times \text{IQR}$  arba  $Q_3 + 1,5 \times \text{IQR}$ , laikomi potencialiais nuokrypiais. Šis metodas yra ypač veiksmingas norint suprasti skirtingų subjektų EKG intervalų kintamumą ir asimetriją. Tolesnėje dalyje pateikiamas visapusiškas ir detalus paaiškinimas apie matricų pagrindu veikiančių algoritmų ir statistinių metodų taikymą įvairioms diagnostikos priemonėms. Šios priemonės gali apimti širdies ir kraujagyslių sistemos savaiminį susitvarkymą veikiant išorinei apkrovai, kompleksiško sugriuvimą atliekant fizinius pratimus, ankstyvą prieširdžių virpėjimo epizodų nustatymą ir ŠRV (širdies ritmo variabilumo) analizę kompleksiško atitikčiai ištirti. Kiekviena iš šių taikymo sričių yra svarbi dėl savo didelės klinikinės svarbos. Todėl, siekiant užtikrinti tikslius ir prasmingus rezultatus, jie analizuojami naudojant jau sukurtus ir naujus moderniausius algoritmus.

### 6.3 Širdies signalų analizės algoritmai ir taikymas

#### **PMLD matrica pagrįstas širdies ir kraujagyslių sistemos kompleksiško sugriuvimo algoritmas streso testų metu (apkrovos fazė)**

Tobulos Lagranžo skirtumų (PMLD) matricos buvo panaudotos EKG parametrų analizei šiuose tyrimuose [13, 73, 119]. Šiame darbe PMLD taip pat pritaikytas analizuoti širdies susitraukimų dažnio (HR) ir arterinio kraujospūdžio (AKS) sąveikai atliekant fizinę veiklą, vadinamą streso testu. Ši analizė padeda suprasti sudėtingumo žlugimą, kuris įvyksta apkrovos fazės pabaigoje, ir atskleidžia subtilius pokyčius, atsirandančius širdies ir kraujagyslių sistemoje reaguojant į fizinę krūvį. Analizė pagrįsta išankstinėmis žiniomis apie tiriamuosius, kai EKG duomenys renkami iš dviejų grupių: turinčių normalų arterinį kraujospūdį (vadinamoje sveikųjų grupėje) ir tų, kurių kraujospūdis padidėjęs (vadinamoje nesveikųjų grupėje). Taip pat naudojami įvairūs statistiniai metodai, skirti EKG signalų kitimo diapazonui nustatyti, padedantys generuoti klasifikavimo metodus. Be to, buvo sukurta sprendimų palaikymo sistema, skirta naujiems dalykams išbandyti ir klasifikuoti remiantis šiomis išvadomis. RR intervalas tarp plakimo ir JT bangos trukmė įrašomi kaip laiko eilutės:  $x = (x_1, x_2, \dots, x_n)$  ir  $y = (y_1, y_2, \dots, y_n)$ ; čia  $n$  yra užregistruotų širdies dūžių skaičius atliekant testavimą streso sąlygomis. Lagranžo skirtumo (PMLD) kvadratinės tobulos matricos konstravimo kriterijai yra jau išsamiai paaiškinti [13, 49, 74]. Antrosios eilės PMLD vaizdas yra toks:  $L_{\delta,k}^{(1)} = \begin{bmatrix} x_k & x_{k+\delta} - y_{k+\delta} \\ x_{k-\delta} - y_{k-\delta} & y_k \end{bmatrix}$  [13, 49]. Nuosekliųjų duomenų transformavimas į skaliarines laiko eilutes atliekamas naudojant kartografavimo funkciją  $L_{\delta,k}^{(\beta)}: \mathcal{F}(L_{\delta,k}^{(\beta)}) = \text{disc}(L_{\delta,k}^{(\beta)}) = (a_{11} - a_{22})^2 + 4a_{12}a_{21}$ , čia indeksai žymi elementų koordinates matricoje  $L_{\delta,k}^{(\beta)}$  [49]. Taip pat taikoma vidinė ir išorinė išlyginimo technika, kuri perimta iš  $s_k(3,4,1)$  [13]. Atlikus minėtus veiksmus, pasiekiamas reikšmingas algebrinis ryšys tarp RR/JT, kuris apskaičiuojamas per minutę visai kohortai. Algebrinis ryšys nusako HR aktyvumą testavimo fizinio krūvio metu. Taip pat kartą per minutę matuojamas sistolinis ir diastolinis AKS, o tai reiškia kraujospūdžio reguliavimą fizinio krūvio metu. RR intervalas tarp plakimo ir JT bangos trukmė pirmiausia įtraukiami į PMLD antros eilės matricos architektūrą. Matricos transformacija į skaliarinę laiko eilutę atliekama naudojant diskriminantinę analizę:  $\text{disc}(\text{RR}/\text{JT})$ . Tada sugeneruojamas sklaidos grafikas su  $(S - D)/S$  x – ašyje ir  $\text{disc}(\text{RR}/\text{JT})$  y – ašyje. Krūvio fazės sklaidos grafikas pavaizduotas raudonai, o atkūrimo fazės – mėlynai. Fazių diagramose gauti duomenų taškai pirmiausia pritaikomi pasitelkiant trendo liniją, o tada tie duomenų taškai įtraukiami į Gauso skirstinį. Vienosios sigmos taisyklės implikacija padeda sugeneruoti kitimo intervalą, o kandidatai yra testuojami pagal tą intervalą (pagal tam tikrą sąlygų rinkinį). Vienas iš individo pavyzdžių parodytas 31 pav.



**31 pav.** Kandidato atlikto testo analizė

RR intervalas ir JT bangos trukmė nustatomi iš asmens EKG ir apdorojami atliekant matematinės ir skaitinių metodų procedūras. 31 pav., a, pavaizduoti ŠR ir ABP pokyčiai laiko atžvilgiu. Kandidato ABP rodmenys priskiria jį normaliam ABP turinčiam asmeniui. 31 pav., b, apkrovos fazės metu gaunamas nuolydžio koeficientas:  $(-1,988)$ . 31 pav., c, klasifikavimo intervalas priskiria individą į apatinę intervalo ribą ir priskiria jį sergančiųjų asmenų kategorijai. Atliekami tolesni skaičiavimai ir ši nuolydžio koeficiento reikšmė apdorojama per statistinę rutiną ir patikrinamos trys sąlygos: (1)  $T \leq (\mu_{U_L} - \sigma_{U_L})$ ; (2)  $T \geq (\mu_{H_L} + \sigma_{H_L})$  ir  $(\mu_{U_L} - \sigma_{U_L}) < T < (\mu_{H_L} + \sigma_{H_L})$ . Šiuo atveju įvykdoma trečioji sąlyga ir generuojama interpoliacijos koeficiento reikšmė:  $(-0,585)$ . Galiausiai dėl šios interpoliacijos koeficiento reikšmės dešinėsios trikampio pusės plotis yra trys vienetai, o kairiosios trikampio pusės – aštuoni vienetai; dėl to kraujospūdžio reguliavimas yra ryškesnis, palyginti su širdies susitraukimų dažnio pokyčiais apkrovos metu. O tai rodo, kad, nepaisant iš pažiūros sveiko ABP rodmenų ramybės metu (prieš testavimą nepalankiausiomis sąlygomis), širdies ir kraujagyslių sistema kovoja su dideliais krūviais. Nors ramybės sąlygomis asmens kraujospūdis atrodo normalus, testų taikymas krūvio sąlygomis atskleidžia subtilius santykinius skirtumus naudojant šiame tyrime siūlomus matematinius metodus.



### **Matrica pagrįstas algoritmas, skirtas sudėtingumo griūčiai ir širdies ir kraujagyslių sistemos saviorganizacijai streso testo metu (apkrovos ir atsigavimo fazės)**

Tokie procesai, kaip „sudėtingumo griūtis“ (atsiranda apkrovos fazės pabaigoje), „širdies ir kraujagyslių sistemos savaiminis susitvarkymas“ (stebimas tiek krūvio, tiek atsigavimo fazėse) ir „adaptacijos greičio indeksas“ (nurodantis atsigavimą po treniruotės), yra labai svarbūs norint suprasti sudėtingus širdies ir kraujagyslių sistemos procesus fizinio krūvio metu. Šios sąvokos paaiškina širdies ir kraujagyslių sistemos būklę bei dinamines reakcijas ir turi diagnostinę vertę. Ankstesnėje dalyje buvo išsamiai išnagrinėta testavimo krūvio sąlygomis fazė. Šiame tyrime nuodugniai išanalizuoti tiek apkrovos, tiek atsigavimo etapai testavimo krūvio sąlygomis. Tolesni tyrimai [129, 134] taip pat pabrėžė atsigavimo fazės svarbą, todėl pabrėžiama jos svarba vertinant širdies ir kraujagyslių sistemos atsigavimo efektyvumą [135]. [136]. Šioje tyrimo dalyje siekiama šių pagrindinių tikslų: pasiūlyti antros eilės PMLD matrica pagrįstą algoritmą, grįstą laiko uždelstais modeliais analizuojant RR intervalą tarp plakimo ir JT bangą, siekiant įvertinti sudėtingumo žlugimą ir širdies bei kraujagyslių sistemos saviorganizaciją testavimo nepalankiausiomis sąlygomis metu bei sukurti du sveikatos rodiklius.

Iš pradžių išankstinio duomenų apdorojimo etape laiko eilutės  $x_k$  ir  $y_k$  (kur  $x_k$  ir  $y_k$  reiškia RR intervalą tarp plakimo ir JT bangą) pirmiausia apdorojamos signalui slopinti naudojant variacinio režimo skaidymo (VMD) metodą. Tada abi laiko eilutės normalizuojamos naudojant paprastus normalizavimo metodus  $x_k/x_{max}$  ir  $y_k/y_{max}$ , čia  $x_{max}$  ir  $y_{max}$  reiškia maksimalią tų intervalų trukmę atliekant testavimą krūvio sąlygomis;  $k = 1, 2, 3, \dots$  [107]. Tada apskaičiuojamas skirtumas tarp laiko eilučių  $x$  ir  $y$ . Tai viena iš šio darbo hipotezių, kad iš skirtumo signalo gautos laiko eilutės suteiktų daugiau informacijos apie sudėtingą širdies ir kraujagyslių sistemos dinamiką atliekant testavimą krūvio sąlygomis. Kitas svarbus šio tyrimo bruožas yra adaptacijos indekso greitis, apskaičiuotas tokiu būdu:  $A_d = \frac{1}{n} \sum_{i=1}^n (J^{Ti}/J^{T_{max}} - RR_i/RR_{max}) \times 100$ . Adaptacijos greičio indekso skaičiavimo formulė perimta iš [135]. Tai suteikia analitinių įžvalgų kuriant vieną iš pagrindinių sveikatos rodiklių, vadinamą alfa. Svarbu pažymėti, kad norint sukurti sveikatos rodiklį alfa, būtinas kitas svarbus parametras, pavadintas modifikuotu adaptacijos indekso greičiu. Jis apskaičiuojamas tik testavimo krūvio sąlygomis atkūrimo fazėje, pažymėtoje  $A_r$ . Norint apskaičiuoti modifikuotą adaptacijos indekso greitį, laiko eilutės RR intervalas ir JT bangos trukmė pirmiausia apdorojami naudojant siūlomą laiko uždelsono modelio algoritmą. Tada gauti laiko uždelsono duomenų taškai įtraukiami į antros eilės uždelstos PMLD matricos architektūrą. Norint paversti matricų seką į skaliarinę laiko eilutę, naudojamas matricos diskriminantas [49]. Galiausiai šios skaliarinės laiko eilutės vidurkis imamas tik testavimo krūvio sąlygomis atkūrimo fazėje, todėl adaptacijos indekso greitis yra pakeistas. Ypatingas dėmesys skiriamas atsigavimo fazės analizei atliekant testavimą krūvio sąlygomis, kad būtų sukurtas sveikatos rodiklis alfa.

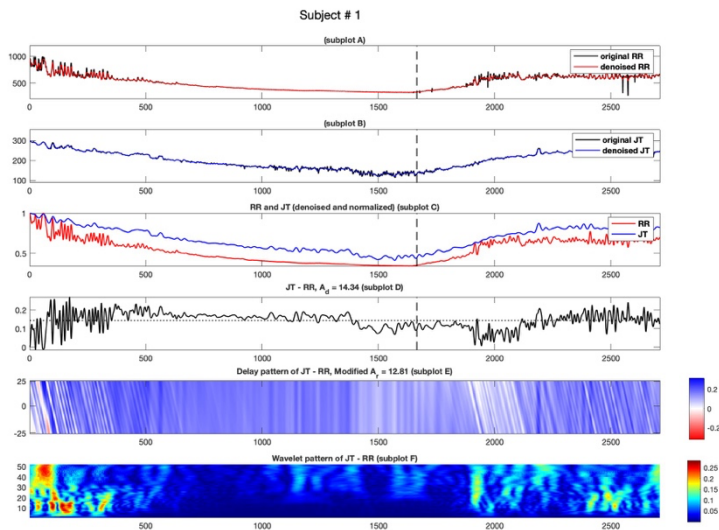
Kitas svarbus sveikatos rodiklis, beta, apskaičiuojamas pagal bangelių koeficientų vidurkį skirtingais laiko intervalais ir pritaikyto antros eilės polinomo koeficientus.

Svarbu pažymėti, kad šie du sveikatos rodikliai kiekybiškai įvertina skirtingus širdies ir kraujagyslių sistemos funkcionalumo aspektus testavimo nepalankiomis sąlygomis metu.

Ypatingas dėmesys skiriamas širdies ir kraujagyslių sistemos sudėtingumo kolapso ir savaiminio organizavimosi supratimui. Šie du procesai yra gyvybiškai svarbūs norint įvertinti širdies ir kraujagyslių sistemos patikimumą tiek apkrovos fazės pabaigoje, tiek atsigavimo fazės pradžioje (per kelias pirmąsias minutes).

Nors bendras širdies ir kraujagyslių sistemos prisitaikymas prie išorinių apkrovų gali būti vertinamas per visą testavimo trukmę (taip pat per skirtumo signalą), ypatingas dėmesys skiriamas konkrečioms laiko žymoms apkrovos ir atsigavimo fazėse.

Du sveikatos rodikliai – alfa ir beta – atlieka esminį vaidmenį vertinant širdies ir kraujagyslių sistemos funkcionalumą. Tačiau taip pat svarbu suprasti jų tarpusavio sąveiką, kuri leidžia sukurti trečiąjį rodiklį – gama. Gama apskaičiuojama remiantis alfa ir beta sąveika ir yra labai svarbi metrika sprendimų palaikymo sistemos kūrimui. Todėl alfa ir beta naudojami trečiajam rodikliui gama generuoti, kuris pritaikomas diagnostikos tikslais kandidatų klasifikavimo sprendimų palaikymo sistemai. Vienas tokių kandidatų iš sveikųjų kohortos pateiktas 32 pav.



**32 pav.** Sveiko subjekto skaičiavimo rezultatai žymimi kaip  $H_A$

Sveikam asmeniui, pavaizduotam 32 pav, prasidėjus apkrovai, prasideda širdies ir kraujagyslių sistemos savaiminis organizavimasis, kuris atsispindi dideliu skirtumo signalo kintamumu ir didele amplitude, kaip matyti 32 pav dalyje D. dalyje. Kintamumas yra akivaizdus, nes širdies ir kraujagyslių sistema reaguoja ir prisitaiko prie palaipsniui didėjančio krūvio sukeltamų pokyčių. Tęsiantis apkrovai, kintamumas mažėja, o tai rodo, kad širdies ir kraujagyslių sistema prisitaikė, todėl skirtumo signalo kintamumas ir dažnis tampa mažesni. Prieš pat apkrovos pabaigos tašką stebimas širdies ir kraujagyslių sistemos sudėtingumo kolapsas – skirtumo

signalų kintamumas išsilygina. Per pirmąsias dvi atsigavimo fazės minutes, analizuojant normalizuoto RR intervalo ir JT bangos sąveiką (žr. pav. C), galima stebėti širdies ir kraujagyslių sistemos savireguliaciją. Per tas pačias pirmąsias dvi atkūrimo fazės minutes normalizuoto RR intervalo ir JT bangos laiko eilučių amplitudės linkusios suartėti, todėl tiriamojo atsigavimo procesas pailgėja. Šiam tiriamajam, tęsiantis krūviui, pradžioje atsiranda raudonos ir baltos spalvos dryžiai, rodantys širdies ir kraujagyslių sistemos saviorganizaciją reaguojant į palaipsniui didėjančią fizinę krūvį. Apkrovos pabaigos taške širdies ir kraujagyslių sistemos sudėtingumas atsiskleidžia per šviesiai baltų ir mėlynų dryžių mišinį. Pirmosiomis keliomis atsigavimo fazės minutėmis pastebimas sistemos savaiminis atsigavimas – tai iliustruoja šviesiai mėlyni ir balti dryžiai. Šiuos rezultatus taip pat galima palyginti su anksčiau analizuotu skirtumo signalo kintamumu. Be to, apskaičiuojamas adaptacijos indekso greitis ( $A_d$ ) 14,34 ir didesnės  $A_d$  reikšmės rodo greitesnį ir jautresnį širdies ir kraujagyslių sistemos prisitaikymą prie fizinio aktyvumo. Be to, pagal šio darbo tikslą taip pat apskaičiuojamas modifikuotas adaptacijos indeksas  $A_r$  ir gaunamos šios reikšmės 12,81.

Dar vienas širdies ir kraujagyslių sistemos sudėtingumo žlugimo ir savaiminio organizavimosi vaizdas išryškėja atliekant bangelių analizę. Nagrinėjant Šano bangelės modelį su srove, galima stebėti laiko eilučių pokyčius dažnio analizės požiūriu. Bangelių analizė atliekama skirtumo signalui, kuris padalinamas į tris dalis, atspindinčias visą testavimo nepalankiausiomis sąlygomis trukmę. Pirmoji dalis apima pradinį 900 duomenų taškų, antroji – dar 900 taškų, o trečioji – likusius laiko eilutės duomenis. Toks padalijimas leidžia analizuoti duomenis trijose pagrindinėse fazėse: testavimo pradžioje, kai prasideda apkrova; viduryje, kai apkrova nutraukiama; ir pabaigoje, kai prasideda atkūrimo fazė. Kiekvienos iš šių trijų sekcijų vidurkis apskaičiuojamas ir pažymimas kaip  $P_1, P_2$ , ir  $P_3$ . Tada antros eilės daugianario kvadratinė lygtis interpoliuojama per tris plokštumos taškus:  $(-1, P_1)$ ,  $(0, P_2)$ ,  $(1, P_3)$ . Gauta parabolės lygtis pateikiama forma  $mx^2 + nx + c$ , kur dominantis parametras yra  $m$ . Kadangi sudėtingumo žlugimas dažniausiai įvyksta apkrovos pabaigos taške, t. y. vidurinėje atkarpoje, tikimasi, kad parametro  $m$  reikšmė šioje dalyje bus mažesnė nei kitose. Išsamiau išanalizavus sveikų asmenų  $m$  reikšmes paaiškėjo, kad ši hipotezė pasitvirtina visais atvejais –  $m$  reikšmė vidurinėje dalyje yra mažesnė. Tai rodo, kad  $m$  yra svarbi metrika, leidžianti kiekybiškai įvertinti sudėtingumo žlugimą.

F poskyrio pradžioje, prasidėjus apkrovai, matomi šviesiai mėlyni dryžiai – tai spalvotų dryžių atsiradimas, žymintis širdies ir kraujagyslių sistemos saviorganizaciją. Panašus savaiminis susitvarkymas vėl pastebimas ir sveikimo fazės pradžioje, taip pat atpažįstamas pagal mėlynus dryžius. Galiausiai, sveikatos rodiklių alfa ir beta apskaičiavimas leidžia sugeneruoti trečiąjį rodiklį – gama, kuris veikia kaip sprendimų priėmimo metrika klasifikuojant tiriamuosius.

### **Lyginamoji matricinių algoritmų analizė ekg parametrų analizuoti**

Tobulų Lagranžo skirtumų (PMLD) matricių tyrimai patvirtino jų efektyvumą analizuojant EKG parametrus ir prisidedant prie ankstyvo širdies ligų nustatymo, kaip parodyta ankstesniuose tyrimuose [13, 49, 53]. Šia tyrimo dalimi siekiama šių tikslų: (1) Panaudoti esamą PMLD matricos architektūrą (vadinamą pirminę matricos

struktūra – PMF) ir palyginti jos analitinį bei skaičiavimo efektyvumą su dviem kitomis matricos architektūromis (vadinamomis antrinėmis matricos struktūromis – SMF1 ir SMF2). (2) Transformuoti matricos duomenų rinkinį į skaliarinę seką, naudojant tiek matricos normą, tiek matricos diskriminantą, ir nustatyti, kuris iš šių skaliarinės transformacijos metodų yra tinkamiausias EKG parametrų analizei.

### **Pirminės matricos struktūra (PMF)**

Ši matricos architektūra yra pagrįsta šešiais konkrečiais kriterijais, aprašytais [13]. Neprarandant bendrumo, laikoma, kad yra trys laiko eilutės:  $(x_n: n = 0, 1, 2, 3 \dots)$ ,  $(y_n: n = 0, 1, 2, 3 \dots)$  ir  $(z_n: n = 0, 1, 2, 3 \dots)$  kuris atitinka JT bangą, QRS kompleksą ir RR interval. Čia  $n$  žymi laiko momentą, o parametras  $\delta$  reiškia laiko delsą. Atsižvelgiant į tai, nuskaitomi devyni trečios eilės PMF matricos elementai:

$$\begin{bmatrix} x_n & y_{n+\delta} - x_{n+\delta} & z_{n+\delta} - x_{n+\delta} \\ y_{n-\delta} - x_{n-\delta} & y_n & z_{n+\delta} - y_{n+\delta} \\ z_{n-\delta} - x_{n-\delta} & z_{n-\delta} - y_{n-\delta} & z_n \end{bmatrix}.$$

Panašiai nuskaitomi devyni SMF1 elementai:

$$\begin{bmatrix} 2x_n & x_{n+1} - y_{n+1} & x_{n+1} - z_{n+1} \\ y_{n-1} - x_{n-1} & 2y_n & y_{n+1} - z_{n+1} \\ z_{n-1} - x_{n-1} & z_{n-1} - y_{n-1} & 2z_n \end{bmatrix}.$$

o SMF2 parašyta:

$$\begin{bmatrix} x_n + z_n & x_{n+1} - y_{n+1} & z_{n+1} - x_{n+1} \\ x_{n-1} - y_{n-1} & 2y_n & y_{n+1} - z_{n+1} \\ z_{n-1} - x_{n-1} & y_{n-1} - z_{n-1} & z_n + x_n \end{bmatrix}.$$

### **Reguliuojama matricos architektūros konfigūracija**

Matricos architektūros koreguojamumas reiškia laisvės laipsnį organizuoti matricos elementus skirtingomis konfigūracijomis, laikantis šešių [13]. suformuluotų kriterijų. Šie apribojimai užtikrina, kad elementų išsidėstymas matricoje atitiktų nuoseklų modelį, išsaugant vietinę matricos struktūrą. Toks laisvės laipsnis galimas SMF1 ir PMF matricoms dėl jų leksikografinės pusiausvyros, tačiau jis netaikomas SMF2 matricai. Iš keturių galimų reguliuojamų konfigūracijų tolesnei analizei pasirinkta ta, kuri pateikta (32). Šiai transformacijai gali būti taikomos įvairios atvaizdavimo funkcijos  $\mathcal{F}$ . Pavyzdžiui, matricos norma naudojama [13], o matricos diskriminantas yra pagrindas matricos sekoms konvertuoti į skaliarines laiko eilutes [49]. Šiame skyriuje matrica bus transformuota į skaliarinę seką taikant tiek matricos normą, tiek matricos diskriminantą.

### **Didysis diskriminantas ir matricos norma**

Trečios eilės matricos SMF1 ir SMF2 elementai gali būti pateikti tokia forma:

$$MA_{a^{(n)}} = \begin{bmatrix} a_{11}^{(n)} & a_{12}^{(n)} & a_{13}^{(n)} \\ a_{21}^{(n)} & a_{22}^{(n)} & a_{23}^{(n)} \\ a_{31}^{(n)} & a_{32}^{(n)} & a_{33}^{(n)} \end{bmatrix}. \text{ Didysis diskriminantas (angl. major}$$

discriminant) šiai matricai išreiškiamas taip:  $dsk_1(MA_a^{(n)}) = \rho_{12} * \rho_{13}$ , kur

$$\rho_{12} = [a - \sqrt{a^2 - 3 \cdot b}]^2 \cdot [a + 2\sqrt{a^2 - 3 \cdot b}] - 27c \text{ ir}$$

$$\rho_{13} = [a + \sqrt{a^2 - 3 \cdot b}]^2 \cdot [a - 2\sqrt{a^2 - 3 \cdot b}] - 27c$$

Taip pat,  $a = \text{Inv}_1(MA_a^{(n)}) = a_{11}^{(n)} + a_{22}^{(n)} + a_{33}^{(n)}$ ,  $b = \text{Inv}_2(MA_a^{(n)}) = a_{22}^{(n)} \cdot a_{33}^{(n)} + a_{11}^{(n)} + a_{22}^{(n)} + a_{11}^{(n)} \cdot a_{33}^{(n)} - a_{13}^{(n)} \cdot a_{31}^{(n)} - a_{21}^{(n)} \cdot a_{12}^{(n)} - a_{32}^{(n)} \cdot a_{23}^{(n)}$  ir  $c = \text{Inv}_3(MA_n) = \det(MA_n)$  [107, 138]. [13] Matricos norma naudojama kaip kartografavimo. Šiame darbe ta pati funkcija naudojama palyginant matricos normos ir matricos diskriminanto efektyvumą, siekiant išrinkti geriausią matricos architektūrą. Pirmą, trys EKG parametrai (JT banga, QRS komplekso trukmė ir RR intervalas tarp plakimo), pavaizduoti laiko eilutėmis ( $x_n: n = 0, 1, 2, 3 \dots$ ), ( $y_n: n = 0, 1, 2, 3 \dots$ ), ir ( $z_n: n = 0, 1, 2, 3 \dots$ ), iš anksto apdorojami taikant slenksčio diapazoną, siekiant užtikrinti, kad kiekviena įvesties vertė neviršytų fiziologiškai tikėtinų ribų. Šiuo tikslu kiekvienos laiko eilutės minimalios ir didžiausios reikšmės parenkamos atitinkamai:  $x_{(\min)} = 100 \text{ ms}$ ;  $x_{(\max)} = 400 \text{ ms}$ ;  $y_{(\min)} = 80 \text{ ms}$ ;  $y_{(\max)} = 110 \text{ ms}$ ;  $z_{(\min)} = 600 \text{ ms}$ ; ir  $z_{(\max)} = 1200 \text{ ms}$ .

Bet kokios reikšmės, kurios yra žemesnės už apatinę ribą arba viršija viršutinę ribą, yra koreguojamos iki atitinkamos ribinės reikšmės. Kitaip tariant, laiko eilutės reikšmės  $x_n$ ,  $y_n$  ir  $z_n$  normalizuojamos į intervalą nuo 0 iki 1. Pavyzdžiui, laiko eilutė  $x_n$  normalizuojama kaip  $x_{normalized} = (x - 100)/(400 - 100)$ . Panašiai laiko eilutės  $y_n$  ir  $z_n$  apdorojamos atitinkamai tuo pačiu normalizavimo būdu. Tie patys normalizavimo metodai taip pat naudojami [107].

Iš anksto apdorotos ir normalizuotos laiko eilutės  $x_n$ ,  $y_n$  ir  $z_n$  yra pritaikytos trečiosios eilės matricos architektūroms, kurios atitinkamai atitinka PMF, SMF1 ir SMF2. Norint transformuoti trečiosios eilės matricą į skaliarinę eilutę, naudojant atvaizdavimo funkciją  $\mathcal{F}: \mathbb{R}^{3 \times 3} \rightarrow \mathbb{R}^{1 \times 3}$ , naudojami dveji atvaizdavimo metodai. Didelis matricos diskriminantas naudojamas kaip SMF1 ir SMF2 architektūrų atvaizdavimo funkcija. Norma atitinkamai naudojama kaip PMF architektūros atvaizdavimo funkcija. Vidinis ir išorinis glotninimo būdai taikomi, kai išlyginimo spindulys priderinamas prie [13] optimizuotų verčių. Galiausiai, statistinė metrika, tokia kaip normos dispersija, taip pat didžiojo diskriminanto dispersija, apskaičiuojama kiekvienai laiko sekai iš trijų pradinių laiko eilučių  $x_n$ ,  $y_n$  ir  $z_n$ . Gautos vertės pavaizduotos 17 lentelė (tik sveikų žmonių grupei).

**17 lentelė.** Sveikų kandidatų dispersijos metrika PMF SMF1 ir SMF2

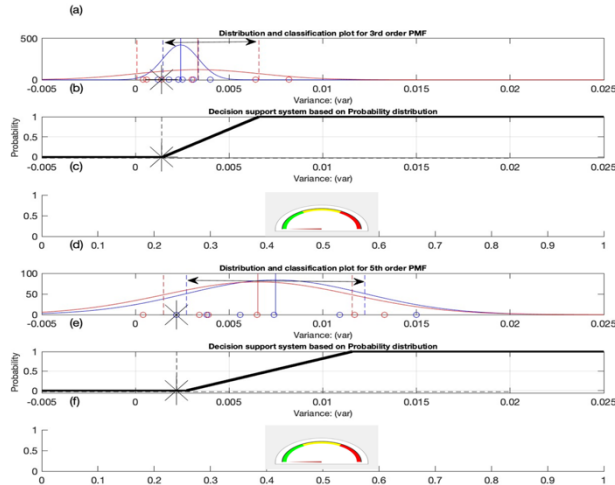
Sveikų tiriamųjų sąrašas, $H_{AFn}$	PMF	SMF1		SMF2	
	Normos dispersija	Didžiojo diskriminan- to dispersija	Normos dispersija	Didžiojo diskriminant o dispersija	Normos dispersija
$H_1$	0,0012	0,0640	0,0016	0,042	0,0010
$H_2$	0,0030	0,0633	0,0047	0,0313	0,0038
$H_3$	0,0023	182,4470	0,0027	16,167	0,0020
$H_4$	0,0014	44,6925	0,0014	1,6402	0,0014
$H_5$	0,0040	608,0258	0,0076	94,7592	0,0052
$H_6$	0,0025	12,4591	0,0026	2,9064	0,0008
$H_7$	0,0031	1618,7723	0,0042	1490,7099	0,0216
$H_8$	0,0018	62,0865	0,0042	65,921	0,0165

17 lentelė pateiktos reikšmės aiškiai rodo, kad normos dispersija suteikia vertingų įžvalgų, reikalingų klasifikavimo tikslais. Priešingai, didelis diskriminantas sukuria skaitines reikšmes, kurios nėra prasmingos tolesniems skaičiavimams. Pavyzdžiui, sveikų žmonių grupėje didžiojo diskriminanto dispersijos minimalus ir didžiausias diapazonas yra nuo 0,042 iki 1618,7723, o panašūs rezultatai gaunami ir nesveikų grupėje. Šios prasmingos įžvalgos rodo, kad šioje konkrečioje tyrimo sistemoje matricos norma, ypač taikoma kartu su PMF, suteikia patikimesnį pagrindą tolesnei EKG parametrų analizei. Kitame skyriuje bus nagrinėjamas PMF diagnostinis potencialas nustatant prieširdžių virpėjimo epizodus.

### **Matrica pagrįstas prieširdžių virpėjimo aptikimo algoritmas (PMF išplečiamumas nuo 2 iki 5 eilės)**

Šis skyrius tęsiasi nuo ankstesnio, tačiau pagrindinis dėmesys skiriamas PMF išplėtimo analizei. Šio tyrimo tikslai yra tokie: (1) Atlikti matricos išplečiamumo analizę nuo 2 eilės iki 5 eilės PMF, įtraukiant penkis EKG parametrus. Yra hipotezė, kad matricos eilės didinimas padidina ir jautrumą, ir kintamumą dėl to, kad sprendimų priėmimo algoritmui pateikiama daugiau informacijos. Šiame tyrime jautrumas apibrėžiamas kaip kiekybinis visos matricos rinkinio matas, užtikrinantis geresnę klasifikaciją. Kita vertus, kintamumas yra kokybinis kategorizavimo slenksčio duomenų paskirstymo taškų matas. Geresnė variacija lemia efektyvesnį asmenų skirstymą į kategorijas. Gaunama plečiama PMF struktūra nuo 2 eilės iki 5 eilės matricių. Pirma, penki EKG parametrai, pavaizduoti laiko eilutėmis ( $x_n: n = 0,1,2,3 \dots$ ), ( $y_n: n = 0,1,2,3 \dots$ ), ( $z_n: n = 0,1,2,3 \dots$ ), ( $u_n: n = 0,1,2,3 \dots$ ) ir ( $v_n: n = 0,1,2,3 \dots$ ) yra įtraukti į PMF matricos architektūrą ir išplečiamos iš 2-osios į 5-osios eilės matricę. Šios laiko eilutės yra įtrauktos į PMF matricos architektūrą ir išplečiamos nuo 2 iki 5 eilės matricos. EKG parametrai yra susieti su kiekviena matricos tvarka, o matricos norma pateikia skaliarinę laiko eilutę. Kiekvienam dalyviui apskaičiuojama šios skaliarinės eilutės dispersija ir pastebima, kad didėjant matricos dydžiui didėja ir jautrumas, ir kintamumas. Matricos jautrumas yra susijęs

su jos gebėjimu sukurti didesnes dispersijos reikšmes, kai matricos dydis didėja, o kintamumas yra geriau pritaikytas duomenų taškams pagal pasiskirstymo kreives. Panašiai kaip ir 3.1 skirsnyje pateiktame tyrime, statistiniai metodai taikomi variacijos intervalui generuoti ir tada kandidatams išbandyti. Vienas iš tokių pavyzdžių parodytas.



**33 pav.** Testo kandidatų klasifikacija: 3 ir 5 eilės PMF architektūra

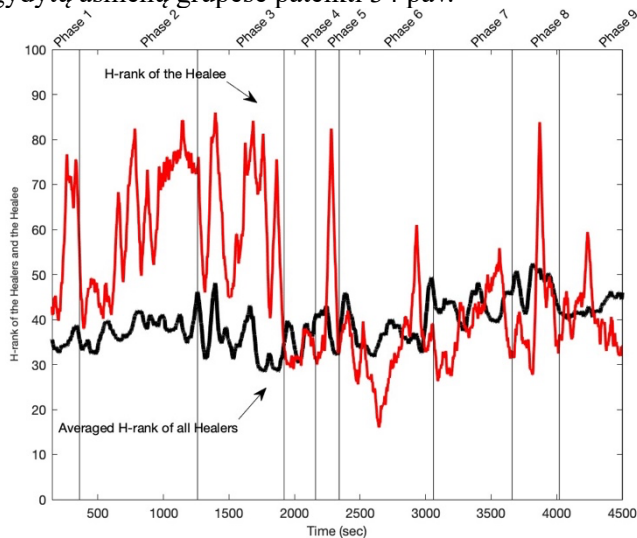
33 pav., a, matyti, kad dispersijos reikšmė tiriamo individo yra kairiajame trečiosios eilės PMLD matricos skirstinio gale. Žvaigždutės simbolis žymi individo vietą klasifikavimo intervale. Dispersijos reikšmė yra perduodama taikant interpoliacijos taisyklės, o sveikam kandidatui suformuluota sąlyga yra patenkinta būtent šiam individui. Be to, tikimybių pasiskirstymo diagrama 33 pav., b, rodo, kad tikimybė, jog tiriamasis priklauso nesveikų grupei, yra mažesnė nei 0,1, kas patvirtina jo priskyrimą sveikų asmenų grupei. Galiausiai, kaip parodyta, 33 pav., c, pateiktas pusapskritimio vizualinis indikatorius demonstruoja rezultatus žalioje zonoje, nurodantioje, kad asmuo yra širdies ir kraujagyslių sveikatos požiūriu saugioje ir sveikoje būsenoje. Panašūs rezultatai gauti ir taikant penktos eilės PMLD matricą, kaip parodyta 33 pav., (d, e, f). Tiek trečiosios, tiek penktosios eilės PMLD matricos konfigūracijos priskiria tiriamąjį sveikų asmenų grupei. Nors buvo žinoma, kad asmeniui nėra prieširdžių virpėjimo, siūlomas algoritmas taip pat teisingai klasifikuoja jį kaip sveiką. Be to, didinant matricos eilę nuo trečios iki penktos, algoritmo jautrumas pagerėja, kas leidžia tiksliau įvertinti tiriamojo sveikatos būklę.

### **Matrica pagrįstas algoritmas šsd analizei atliekant psichologinę sinchronizaciją meditacijos metu**

Šiame tyrime analizuojami RR intervalai dviejų grupių — gydytojų ir pagydytų asmenų. Tyrimo tikslas yra įvertinti sudėtingumo skirtumus tarp šių grupių, taikant Hankelio matricos metodą. Eksperimentas vyko pagal meditacinio gydymo protokolą, trukusį 75 minutes, kurio metu dalyviai atliko įvairias vadovaujamas meditacijos

pozas: sėdėjimą, stovėjimą, gulėjimą, ėjimą bei poziciją, orientuotą į gydymą. Šios pozos buvo suskirstytos į devynias fazes, kurių metu buvo registruojami atitinkami RR intervalai.

Hankelio matrica buvo sudaryta taip, kad kiekviena jos eilutė atitiktų ankstesnės eilutės perkeltą versiją, užtikrinant maksimalų stebėjimo langų persidengimą. Analizėje naudotas 150 x 150 matricos lango dydis, apimantis 300 stebimų duomenų taškų, o matricos rangas svyravo nuo 1 iki maksimalaus 150. Tolesnei analizei buvo pritaikytas vienaskaitos vertės skaidymas (SVD), kurio metu Hankelio matrica išskaidyta į tris komponentus. Hankelio matricos vienaskaitos vertės atspindi skirtingų signalų komponentų svarbą laiko eilutės duomenyse — didesnės vienaskaitos vertės nurodo svarbesnius komponentus. Naudojant iš anksto nustatytą slenkstinę reikšmę ( $\epsilon$ ) galima nustatyti duomenų rangą arba sudėtingumą skirtingais laiko momentais. Siekiant pagerinti analizės aiškumą ir išryškinti HRV (širdies ritmo kintamumo) duomenų tendencijas, rekonstruotoms laiko eilutėms, gautoms iš H rango, taikytas slankiojo vidurkio išlyginimo metodas. Rekonstruoti H rangai gydytojų ir pagydytų asmenų grupėse pateikti 34 pav.



**34 pav.** Dalyvių H reitingų grafikas: (a) aštuonių gydytojų vidutiniai H reitingai (juoda), (b) Healee H reitingai (raudona)

34 pav, ypatingas dėmesys sutelktas į gydytojų vidutinį H rangą (vaizdas juoda spalva) ir gydomojo H rangą (vaizdas raudonai). Pažymima, kad per pirmąsias tris meditacijos pratimo fazes rekonstruotos gydytojų ir gydomojo H rangos laikosi išskirtiniais laiko eilučių modeliais. Prasidėjus ketvirtajai fazei, dalis atkurto vidutinio H rango pradeda labiau derėti su atkurtomis laiko eilutėmis iš sveikojo H rango, ir ši tendencija tęsiasi per ketvirtą, penktą ir šeštą fazę. Septintoje fazėje tampa akivaizdu, kad atkurta vidutinio H laipsnio gydytojų laiko eilutė artėja prie visiškos



sinchronizacijos su gydomojo H laipsnio laiko eilutėmis, o tai reiškia ryšio tarp gydytojų ir gydomojo užmezgimą. Aštuntoje fazėje pasiekama abiejų H eilučių laiko eilučių konvergencija, nurodant sinchronizavimą – procesas šiame tyrime vadinamas sudėtingumo suderinimu. Galiausiai devintoje fazėje, kuri yra meditacijos pratimo pabaiga, pastebimas visiškas abiejų grupių rekonstruotų H rango laiko eilučių sinchronizavimas, kaip 34 pav.

## 6.4 Išvados

Subtilūs širdies ir kraujagyslių sistemos skirtumai tarp asmenų, kurių arterinis kraujospūdis normalus ir kurių padidėjęs, ypač ryškiai atsiskleidžia atliekant streso testą fizinio krūvio fazėje. Antrojo laipsnio PMLD matricinė architektūra suteikia galimybę geriau suprasti šiuos subtilius procesus, vadinamus sudėtingumo žlugimu, ir leidžia juos kiekybiškai įvertinti bei aiškiai vizualizuoti. Ši matricinė architektūra pasirodė esanti veiksminga analizuojant algebrinius tarpusavio ryšius tarp EKG parametrų, tokių kaip RR intervalas ir JT bangos trukmė, taip prisidedant prie ankstyvosios širdies ir kraujagyslių funkcijos pokyčių — sudėtingumo žlugimo — aptikimo.

Algebriniai ryšiai tarp EKG parametrų streso testo metu suteikia vertingų įžvalgų apie svarbius reiškinius, tokius kaip sudėtingumo žlugimas, širdies ir kraujagyslių sistemos saviorganizacija bei adaptacijos greitis. Šios išvados gautos analizuojant EKG parametrų, tokių kaip RR intervalas ir JT bangos trukmė, elgseną tiek fizinio krūvio, tiek atsigavimo fazėse, leidžiant geriau suprasti širdies ir kraujagyslių sistemos funkciją fizinio aktyvumo metu. Antrojo laipsnio laiko uždelstas tobulųjų Lagrange skirtumų matricinis algoritmas kartu su statistiniais metodais suteikia efektyvias priemones šių sudėtingų procesų išgavimui, analizei ir vizualizavimui.

Lyginant tris matricines architektūras – PMF, SMF1 ir SMF2 – nustatyta, kad PMF algoritmas pranoksta kitus dėl savo atitikimo optimalaus EKG analizės matricos kriterijams bei lankstumo matricos dydžio atžvilgiu. Ši savybė suteikia galimybę efektyviau plėtoti ir gilinti EKG analizės metodus.

PMF pritaikomumas ir išplečiamumas buvo patvirtinti kaip veiksmingi, leidžiantys atlikti išsamią penkių EKG parametrų (RR, JT, QRS, AP, DP) matematinę bei statistinę analizę, skirtą vertinti ir prieširdžių virpėjimo epizodams aptikti.

Hankelio matricinis algoritmas pasitvirtino kaip naudingas įrankis nustatant sudėtingumo ir sinchronizacijos reiškinius dviejų grupių, dalyvaujančių gydymosi meditacijos seansuose. Buvo pastebėta, kad psichologinė sinchronizacija vyksta tam tikrose meditacijos fazėse, o šis procesas gali būti ne tik stebimas, bet ir kiekybiškai įvertintas taikant specializuotus statistinius metodus bei būsenų erdvės vizualizaciją.

## REFERENCES

- [1] A. C. Guyton, "Hall JE Textbook of Medical Physiology," *Yiğit G. Pregnancy and Lactation. Missisipi*, vol. 1036, 1996.
- [2] D. P. Zipes, J. Jalife, and W. G. Stevenson, *Cardiac electrophysiology: from cell to bedside E-book*. Elsevier Health Sciences, 2017.
- [3] J. Camm, "Task Force of the European Society of Cardiology and the North American Society of Pacing and Electrophysiology. Heart Rate Variability: Standarts of measurement, physiological interpretation and clinical use," *Circulation*, vol. 93, pp. 1043-1065, 1996.
- [4] F. Shaffer and J. P. Ginsberg, "An overview of heart rate variability metrics and norms," *Frontiers in public health*, p. 258, 2017.
- [5] K. Burke da Silva, "Evolution-centered teaching of biology," *Annual Review of Genomics and Human Genetics*, vol. 13, no. 1, pp. 363-380, 2012.
- [6] C. F. Sing, J. H. Stengård, and S. L. Kardia, "Genes, environment, and cardiovascular disease," *Arteriosclerosis, thrombosis, and vascular biology*, vol. 23, no. 7, pp. 1190-1196, 2003.
- [7] A. Benetos, A. Rudnichi, M. Safar, and L. Guize, "Pulse pressure and cardiovascular mortality in normotensive and hypertensive subjects," *Hypertension*, vol. 32, no. 3, pp. 560-564, 1998.
- [8] P. C. Ivanov *et al.*, "Multifractality in human heartbeat dynamics," *Nature*, vol. 399, no. 6735, pp. 461-465, 1999.
- [9] E. J. Topol, "Individualized medicine from prewomb to tomb," *Cell*, vol. 157, no. 1, pp. 241-253, 2014.
- [10] S. M. Pincus, "Approximate entropy as a measure of system complexity," *Proceedings of the national academy of sciences*, vol. 88, no. 6, pp. 2297-2301, 1991.
- [11] U. R. Acharya *et al.*, "Automated characterization and classification of coronary artery disease and myocardial infarction by decomposition of ECG signals: A comparative study," *Information Sciences*, vol. 377, pp. 17-29, 2017.
- [12] C. Che, P. Zhang, M. Zhu, Y. Qu, and B. Jin, "Constrained transformer network for ECG signal processing and arrhythmia classification," *BMC Medical Informatics and Decision Making*, vol. 21, no. 1, p. 184, 2021.
- [13] P. Ziaukas, A. Alabdulgader, A. Vainoras, Z. Navickas, and M. Ragulskis, "New approach for visualization of relationships between RR and JT intervals," *PloS one*, vol. 12, no. 4, p. e0174279, 2017.
- [14] A. Vainoras, L. Gargasas, R. Ruseckas, V. Miškinis, and R. Jurkonienė, "Computerised exercise electrocardiogram analysis system" Kaunas-Load", " in *24th international congress on Electrocadiology [and] 38th international symposium on Vectorcardiography: abstracts book; Bratislava, Slovak Republic, June 24-28, 1997. Bratislava, 1997, 1997*.
- [15] "World Health Organization," *Cardiovascular diseases (CVDs)*, 2021. [Online]. Available: [https://www.who.int/news-room/fact-sheets/detail/cardiovascular-diseases-\(cvds\)](https://www.who.int/news-room/fact-sheets/detail/cardiovascular-diseases-(cvds)).
- [16] A. S. Update, "Heart disease and stroke statistics–2017 update," *Circulation*, vol. 135, pp. e146-e603, 2017.
- [17] P. Libby, P. M. Ridker, and G. K. Hansson, "Progress and challenges in translating the biology of atherosclerosis," *Nature*, vol. 473, no. 7347, pp. 317-325, 2011.

- [18] A. Gupta, G. Ghimire, and F. G. Hage, "Guidelines in review: 2013 ACCF/AHA Guideline for the Management of Heart Failure," *Journal of Nuclear Cardiology*, vol. 21, pp. 397-399, 2014.
- [19] V. Chairy, "2022 AHA/ACC/HFSA guideline for the management of heart failure," *Journal of the American College of Cardiology*, vol. 79, no. 17, 2022.
- [20] T. Infante *et al.*, "An integrated approach to coronary heart disease diagnosis and clinical management," *American journal of translational research*, vol. 9, no. 7, p. 3148, 2017.
- [21] S. Arab *et al.*, "Cardiovascular proteomics: tools to develop novel biomarkers and potential applications," *Journal of the American College of Cardiology*, vol. 48, no. 9, pp. 1733-1741, 2006.
- [22] S. D. Fihn *et al.*, "2012 ACCF/AHA/ACP/AATS/PCNA/SCAI/STS guideline for the diagnosis and management of patients with stable ischemic heart disease: a report of the American College of Cardiology Foundation/American Heart Association task force on practice guidelines, and the American College of Physicians, American Association for Thoracic Surgery, Preventive Cardiovascular Nurses Association, Society for Cardiovascular Angiography and Interventions, and Society of Thoracic Surgeons," *Journal of the American College of Cardiology*, vol. 60, no. 24, pp. e44-e164, 2012.
- [23] A. C. Skelly *et al.*, "Noninvasive testing for coronary artery disease," 2016.
- [24] G. Prieto-Avalos, N. A. Cruz-Ramos, G. Alor-Hernandez, J. L. Sánchez-Cervantes, L. Rodriguez-Mazahua, and L. R. Guarneros-Nolasco, "Wearable devices for physical monitoring of heart: a review," *Biosensors*, vol. 12, no. 5, p. 292, 2022.
- [25] R. Kotha, C. Streitmatter, A. Serdiuk, N. N. Aldawoodi, and R. S. Ackerman, "Cardiac Remote Monitoring Devices and Technologies: A Review for the Perioperative Physician and Telemedicine Providers," *Cureus*, vol. 16, no. 2, 2024.
- [26] S. B. Rosalki, R. Roberts, H. A. Katus, E. Giannitsis, J. H. Ladenson, and F. S. Apple, "Cardiac biomarkers for detection of myocardial infarction: perspectives from past to present," *Clinical chemistry*, vol. 50, no. 11, pp. 2205-2213, 2004.
- [27] J. A. Leopold and J. Loscalzo, "Emerging role of precision medicine in cardiovascular disease," *Circulation research*, vol. 122, no. 9, pp. 1302-1315, 2018.
- [28] A. T. Reisner, G. D. Clifford, and R. G. Mark, "The physiological basis of the electrocardiogram," *Advanced methods and tools for ECG data analysis*, vol. 1, p. 25, 2006.
- [29] Y. Sattar and L. Chhabra, "Electrocardiogram," in *StatPearls [Internet]*: StatPearls Publishing, 2023.
- [30] D. Fabian and I. Ahmed, "Ambulatory ECG monitoring," 2023.
- [31] D.-g. Fu, "Cardiac arrhythmias: diagnosis, symptoms, and treatments," *Cell biochemistry and biophysics*, vol. 73, no. 2, pp. 291-296, 2015.
- [32] J. Václavík *et al.*, "ECG in patients with acute heart failure can predict in-hospital and long-term mortality," *Internal and emergency medicine*, vol. 9, pp. 283-291, 2014.
- [33] O. Györfi *et al.*, "Accuracy of high-density EEG electrode position measurement using an optical scanner compared with the photogrammetry method," *Clinical neurophysiology practice*, vol. 7, pp. 135-138, 2022.
- [34] K. Katsaliaki and S. Kumar, "The Past, Present, and Future of the Healthcare Delivery System Through Digitalization," *IEEE Engineering Management Review*, vol. 50, no. 4, pp. 21-33, 2022.
- [35] J. Xue and L. Yu, "Applications of machine learning in ambulatory ECG," *Hearts*, vol. 2, no. 4, pp. 472-494, 2021.

- [36] G. Y. Lip and H. S. Lim, "Atrial fibrillation and stroke prevention," *The Lancet Neurology*, vol. 6, no. 11, pp. 981-993, 2007.
- [37] A. Mattu, J. A. Tabas, and W. J. Brady, *Electrocardiography in emergency, acute, and critical care*. American College of Emergency Physicians, 2019.
- [38] P. J. Zimetbaum and M. E. Josephson, "Use of the electrocardiogram in acute myocardial infarction," *New England Journal of Medicine*, vol. 348, no. 10, pp. 933-940, 2003.
- [39] P. Caldarola *et al.*, "ANMCO-SIMEU consensus document: appropriate management of atrial fibrillation in the emergency department," *European Heart Journal Supplements*, vol. 25, no. Supplement\_D, pp. D255-D277, 2023.
- [40] P. Melillo, R. Castaldo, G. Sannino, A. Orrico, G. De Pietro, and L. Pecchia, "Wearable technology and ECG processing for fall risk assessment, prevention and detection," in *2015 37th Annual International Conference of the IEEE Engineering in Medicine and Biology Society (EMBC)*, 2015: IEEE, pp. 7740-7743.
- [41] A. Bansal and R. Joshi, "Portable out-of-hospital electrocardiography: A review of current technologies," *Journal of arrhythmia*, vol. 34, no. 2, pp. 129-138, 2018.
- [42] C. Bernard, *An introduction to the study of experimental medicine*. Courier Corporation, 1957.
- [43] W. Cannon, "The Wisdom of the Body. New York, WW Nort & Company," *Inc. Published online*, 1932.
- [44] N. Wiener, *Cybernetics or Control and Communication in the Animal and the Machine*. MIT press, 2019.
- [45] L. Luciani, *Human physiology v. 1, 1911*. Macmillan & Company, 1911.
- [46] A. C. Guyton, "Cardiac output and its regulation," *Circulatory physiology*, 1973.
- [47] L. Von Bertalanffy, "The theory of open systems in physics and biology," *Science*, vol. 111, no. 2872, pp. 23-29, 1950.
- [48] W. B. Carpenter, *Principles of human physiology*. Blanchard and Lea, 1860.
- [49] N. W. Qammar, U. Orinaitė, V. Šiaučiūnaitė, A. Vainoras, G. Šakalytė, and M. Ragulskis, "The Complexity of the Arterial Blood Pressure Regulation during the Stress Test," *Diagnostics*, vol. 12, no. 5, p. 1256, 2022.
- [50] G. Clermont and D. Angus, "Towards understanding pathophysiology in critical care: the human body as a complex system," in *Yearbook of Intensive Care and Emergency Medicine 2001*: Springer, 2001, pp. 13-22.
- [51] G. Pocock, C. D. Richards, and D. A. Richards, *Human physiology*. Oxford University Press, USA, 2013.
- [52] J. J. Batzel, F. Kappel, D. Schneditz, and H. T. Tran, *Cardiovascular and respiratory systems: modeling, analysis, and control*. SIAM, 2007.
- [53] V. Šiaučiūnaitė, M. Ragulskis, A. Vainoras, B. Dabiri, and E. Kaniusas, "Visualization of complex processes in cardiovascular system during electrical auricular vagus nerve stimulation," *Diagnostics*, vol. 11, no. 12, p. 2190, 2021.
- [54] A. Hollander and L. Bouman, "Cardiac acceleration in man elicited by a muscle-heart reflex," *Journal of Applied Physiology*, vol. 38, no. 2, pp. 272-278, 1975.
- [55] E. W. Faria and I. E. Faria, "Cardiorespiratory responses to exercises of equal relative intensity distributed between the upper and lower body," *Journal of sports sciences*, vol. 16, no. 4, pp. 309-315, 1998.
- [56] S. E. O'Sullivan and C. Bell, "The effects of exercise and training on human cardiovascular reflex control," *Journal of the Autonomic Nervous System*, vol. 81, no. 1-3, pp. 16-24, 2000.

- [57] J. H. Chapman and P. Elliott, "Cardiovascular effects of static and dynamic exercise," *European journal of applied physiology and occupational physiology*, vol. 58, pp. 152-157, 1988.
- [58] M. Eriksen, B. A. Waaler, L. Walløe, and J. Wesche, "Dynamics and dimensions of cardiac output changes in humans at the onset and at the end of moderate rhythmic exercise," *The Journal of physiology*, vol. 426, no. 1, pp. 423-437, 1990.
- [59] N. H. Secher, J. P. Clausen, K. Klausen, I. Noer, and J. Trap-Jensen, "Central and regional circulatory effects of adding arm exercise to leg exercise," *Acta physiologica scandinavica*, vol. 100, no. 3, pp. 288-297, 1977.
- [60] E. O'Brien *et al.*, "Working Group on Blood Pressure Monitoring of the European Society of Hypertension International Protocol for validation of blood pressure measuring devices in adults," *Blood pressure monitoring*, vol. 7, no. 1, pp. 3-17, 2002.
- [61] M. Yamaguchi *et al.*, "Diagnostic usefulness of the post-exercise systolic blood pressure response for the detection of coronary artery disease in patients with diabetes mellitus," *Japanese circulation journal*, vol. 64, no. 12, pp. 949-952, 2000.
- [62] G. Mancia *et al.*, "2007 Guidelines for the management of arterial hypertension: The Task Force for the Management of Arterial Hypertension of the European Society of Hypertension (ESH) and of the European Society of Cardiology (ESC)," *European heart journal*, vol. 28, no. 12, pp. 1462-1536, 2007.
- [63] G. Mancia *et al.*, "Reappraisal of European guidelines on hypertension management: a European Society of Hypertension Task Force document," *Blood pressure*, vol. 18, no. 6, pp. 308-347, 2009.
- [64] G. F. Fletcher *et al.*, "Exercise standards for testing and training: a statement for healthcare professionals from the American Heart Association," *Circulation*, vol. 104, no. 14, pp. 1694-1740, 2001.
- [65] R. Armstrong, G. Warren, and J. Warren, "Mechanisms of exercise-induced muscle fibre injury," *Sports medicine*, vol. 12, pp. 184-207, 1991.
- [66] A. M. Aguilar-Molina, F. Angulo-Brown, and A. Muñoz-Diosdado, "Multifractal spectrum curvature of RR tachograms of healthy people and patients with congestive heart failure, a new tool to assess health conditions," *Entropy*, vol. 21, no. 6, p. 581, 2019.
- [67] A. L. Goldberger, L. A. Amaral, J. M. Hausdorff, P. C. Ivanov, C.-K. Peng, and H. E. Stanley, "Fractal dynamics in physiology: alterations with disease and aging," *Proceedings of the national academy of sciences*, vol. 99, no. suppl\_1, pp. 2466-2472, 2002.
- [68] C. K. Peng, S. Havlin, H. E. Stanley, and A. L. Goldberger, "Quantification of scaling exponents and crossover phenomena in nonstationary heartbeat time series," *Chaos: an interdisciplinary journal of nonlinear science*, vol. 5, no. 1, pp. 82-87, 1995.
- [69] P. C. Ivanov *et al.*, "Scaling behaviour of heartbeat intervals obtained by wavelet-based time-series analysis," *Nature*, vol. 383, no. 6598, pp. 323-327, 1996.
- [70] M. Costa, A. L. Goldberger, and C.-K. Peng, "Multiscale entropy analysis of complex physiologic time series," *Physical review letters*, vol. 89, no. 6, p. 068102, 2002.
- [71] A. Porta *et al.*, "Model-based assessment of baroreflex and cardiopulmonary couplings during graded head-up tilt," *Computers in biology and medicine*, vol. 42, no. 3, pp. 298-305, 2012.
- [72] J. W. Kantelhardt, S. A. Zschiegner, E. Koscielny-Bunde, S. Havlin, A. Bunde, and H. E. Stanley, "Multifractal detrended fluctuation analysis of nonstationary time series," *Physica A: Statistical Mechanics and its Applications*, vol. 316, no. 1-4, pp. 87-114, 2002.

- [73] V. Šiaučiūnaitė, A. Vainoras, Z. Navickas, and M. Ragulskis, "Detection of Ischemic Episodes Based on Two Consecutive Declines in the JT/ST Algebraic Relationship," *Applied Sciences*, vol. 11, no. 11, p. 4805, 2021.
- [74] L. Saunoriene, V. Siauciunaite, A. Vainoras, V. Bertasiute, Z. Navickas, and M. Ragulskis, "The characterization of the transit through the anaerobic threshold based on relationships between RR and QRS cardiac intervals," *PloS one*, vol. 14, no. 5, p. e0216938, 2019.
- [75] N. W. Qammar, A. Vainoras, Z. Navickas, G. Jaruševičius, and M. Ragulskis, "Early Diagnosis of Atrial Fibrillation Episodes: Comparative Analysis of Different Matrix Architectures," *Applied Sciences*, vol. 14, no. 14, p. 6191, 2024.
- [76] G. Von Heijne, "A new method for predicting signal sequence cleavage sites," *Nucleic acids research*, vol. 14, no. 11, pp. 4683-4690, 1986.
- [77] A. Savitzky and M. J. Golay, "Smoothing and differentiation of data by simplified least squares procedures," *Analytical chemistry*, vol. 36, no. 8, pp. 1627-1639, 1964.
- [78] M. Shen, W.-N. Chen, J. Zhang, H. S.-H. Chung, and O. Kaynak, "Optimal selection of parameters for nonuniform embedding of chaotic time series using ant colony optimization," *IEEE Transactions on Cybernetics*, vol. 43, no. 2, pp. 790-802, 2013.
- [79] M. Ragulskis, K. Lukoseviciute, Z. Navickas, and R. Palivonaite, "Short-term time series forecasting based on the identification of skeleton algebraic sequences," *Neurocomputing*, vol. 74, no. 10, pp. 1735-1747, 2011.
- [80] R. Palivonaite and M. Ragulskis, "Short-term time series algebraic forecasting with internal smoothing," *Neurocomputing*, vol. 127, pp. 161-171, 2014.
- [81] J. F. Easton, C. R. Stephens, and M. Angelova, "Risk factors and prediction of very short term versus short/intermediate term post-stroke mortality: a data mining approach," *Computers in Biology and Medicine*, vol. 54, pp. 199-210, 2014.
- [82] K.-Y. Chen, "Combining linear and nonlinear model in forecasting tourism demand," *Expert Systems with Applications*, vol. 38, no. 8, pp. 10368-10376, 2011.
- [83] D.-x. Niu, H.-f. Shi, and D. D. Wu, "Short-term load forecasting using bayesian neural networks learned by Hybrid Monte Carlo algorithm," *Applied Soft Computing*, vol. 12, no. 6, pp. 1822-1827, 2012.
- [84] C. Jia, L. Wei, H. Wang, and J. Yang, "Study of track irregularity time series calibration and variation pattern at unit section," *Computational intelligence and neuroscience*, vol. 2014, no. 1, p. 727948, 2014.
- [85] P. R. A. Firmino, P. S. de Mattos Neto, and T. A. Ferreira, "Correcting and combining time series forecasters," *Neural Networks*, vol. 50, pp. 1-11, 2014.
- [86] M. Landauskas, Z. Navickas, A. Vainoras, and M. Ragulskis, "Weighted moving averaging revisited: an algebraic approach," *Computational and Applied Mathematics*, vol. 36, no. 4, pp. 1545-1558, 2017.
- [87] D. Petkevičiūtė-Gerlach, I. Timofejeva, and M. Ragulskis, "Clocking convergence of the fractional difference logistic map," *Nonlinear Dynamics*, vol. 100, no. 4, pp. 3925-3935, 2020.
- [88] U. Orinaitė and M. Landauskas, "Novel feature extraction technique based on ranks of Hankel matrices with application for ECG analysis," *Mathematical Models in Engineering*, vol. 7, no. 2, pp. 40-49, 2021.
- [89] A. Šliupaitė, Z. Navickas, and A. Vainoras, "Evaluation of complexity of ECG parameters using sample entropy and Hankel matrix," *Elektronika ir elektrotechnika*, no. 4, pp. 107-110, 2009.

- [90] G. Kersulyte, Z. Navickas, A. Vainoras, and L. Gargasas, "Calculation of the Hankel matrix ranks of electric and haemodynamic processes in the heart," *Elektronika ir elektrotechnika*, vol. 91, no. 3, pp. 43-48, 2009.
- [91] Y. Wu, R. M. Rangayyan, Y. Zhou, and S.-C. Ng, "Filtering electrocardiographic signals using an unbiased and normalized adaptive noise reduction system," *Medical Engineering & Physics*, vol. 31, no. 1, pp. 17-26, 2009.
- [92] V. Pandey and V. Giri, "High frequency noise removal from ECG using moving average filters," in *2016 International conference on emerging trends in electrical electronics & sustainable energy systems (ICETEESES)*, 2016: IEEE, pp. 191-195.
- [93] F. Takens, "In dynamical systems of turbulence," *Lecture notes in mathematics*, vol. 898, p. 366, 1981.
- [94] M. Small, *Applied nonlinear time series analysis: applications in physics, physiology and finance*. World Scientific, 2005.
- [95] I. Timofejeva *et al.*, "Identification of a group's physiological synchronization with earth's magnetic field," *International journal of environmental research and public health*, vol. 14, no. 9, p. 998, 2017.
- [96] B. Erem *et al.*, "Extensions to a manifold learning framework for time-series analysis on dynamic manifolds in bioelectric signals," *Physical Review E*, vol. 93, no. 4, p. 042218, 2016.
- [97] J. P. Huke and D. S. Broomhead, "Embedding theorems for non-uniformly sampled dynamical systems," *Nonlinearity*, vol. 20, no. 9, p. 2205, 2007.
- [98] Y. Manabe and B. Chakraborty, "A novel approach for estimation of optimal embedding parameters of nonlinear time series by structural learning of neural network," *Neurocomputing*, vol. 70, no. 7-9, pp. 1360-1371, 2007.
- [99] C. Bandt and B. Pompe, "Permutation entropy: a natural complexity measure for time series," *Physical review letters*, vol. 88, no. 17, p. 174102, 2002.
- [100] L. Zunino, F. Olivares, F. Scholkmann, and O. A. Rosso, "Permutation entropy based time series analysis: Equalities in the input signal can lead to false conclusions," *Physics Letters A*, vol. 381, no. 22, pp. 1883-1892, 2017.
- [101] M. H. Milon, "Comparison on fourier and wavelet transformation for an ecg signal," *American Journal of Engineering Research*, vol. 6, no. 8, pp. 01-07, 2017.
- [102] K.-i. Minami, H. Nakajima, and T. Toyoshima, "Real-time discrimination of ventricular tachyarrhythmia with Fourier-transform neural network," *IEEE transactions on Biomedical Engineering*, vol. 46, no. 2, pp. 179-185, 1999.
- [103] I. Romero and L. Serrano, "ECG frequency domain features extraction: A new characteristic for arrhythmias classification," in *2001 Conference Proceedings of the 23rd Annual International Conference of the IEEE Engineering in Medicine and Biology Society*, 2001, vol. 2: IEEE, pp. 2006-2008.
- [104] P. De Chazel and R. Reilly, "A comparison of the ECG classification performance of different feature sets," in *Computers in Cardiology 2000. Vol. 27 (Cat. 00CH37163)*, 2000: IEEE, pp. 327-330.
- [105] A. Josko, "Discrete wavelet transform in automatic ECG signal analysis," in *2007 IEEE Instrumentation & Measurement Technology Conference IMTC 2007*, 2007: IEEE, pp. 1-3.
- [106] N. Ahmed and Y. Zhu, "Early detection of atrial fibrillation based on ECG signals," *Bioengineering*, vol. 7, no. 1, p. 16, 2020.
- [107] V. Petkus *et al.*, "Method for prediction of acute hypotensive episodes," *Elektronika ir elektrotechnika*, vol. 22, no. 1, pp. 44-48, 2016.



- [108] N. W. Qammar, M. Ragulskis, L. Saunoriene, R. Smidtaite, A. Vainoras, and G. Jaruševičius, "Early Diagnosis of Problems Related to the Self-Organization of the Cardiovascular System Based on the Interplay between RR and JT Cardiac Intervals," *Diagnostics*, vol. 14, no. 13, p. 1410, 2024.
- [109] A. K. Jaiswal and B. B. Sharma, "Cluster Synchronization of Networks of Chaotic Systems: A Comprehensive Review of Theory and Applications," *IETE Technical Review*, pp. 1-20, 2024.
- [110] M. Mobini and G. Kaddoum, "Deep chaos synchronization," *IEEE Open Journal of the Communications Society*, vol. 1, pp. 1571-1582, 2020.
- [111] R. Brown, N. F. Rulkov, and E. R. Tracy, "Modeling and synchronizing chaotic systems from time-series data," *Physical Review E*, vol. 49, no. 5, p. 3784, 1994.
- [112] J. M. González-Miranda, "Amplitude envelope synchronization in coupled chaotic oscillators," *Physical Review E*, vol. 65, no. 3, p. 036232, 2002.
- [113] W. Sun, S. Wang, G. Wang, and Y. Wu, "Lag synchronization via pinning control between two coupled networks," *Nonlinear Dynamics*, vol. 79, no. 4, pp. 2659-2666, 2015.
- [114] M. Ahmadlou and H. Adeli, "Visibility graph similarity: A new measure of generalized synchronization in coupled dynamic systems," *Physica D: Nonlinear Phenomena*, vol. 241, no. 4, pp. 326-332, 2012.
- [115] Y. Hoon, M. A. Mohd Radzi, M. A. A. Mohd Zainuri, and M. A. M. Zawawi, "Shunt active power filter: A review on phase synchronization control techniques," *Electronics*, vol. 8, no. 7, p. 791, 2019.
- [116] P. Wang, G. Wen, X. Yu, W. Yu, and T. Huang, "Synchronization of multi-layer networks: From node-to-node synchronization to complete synchronization," *IEEE Transactions on Circuits and Systems I: Regular Papers*, vol. 66, no. 3, pp. 1141-1152, 2018.
- [117] N. Nazmi, S. A. Mazlan, H. Zamzuri, and M. A. A. Rahman, "Fitting distribution for electromyography and electroencephalography signals based on goodness-of-fit tests," *Procedia Computer Science*, vol. 76, pp. 468-473, 2015.
- [118] A. GHAFARI, M. R. Homaeinezhad, Y. Ahmadi, M. Rahnavard, and R. Rahmani, "Macroscopic Visualization of the Heart Electrical Activity Via an Algebraic Computer Model," 2009.
- [119] N. W. Qammar, V. Šiaučiūnaitė, V. Zabiela, A. Vainoras, and M. Ragulskis, "Detection of atrial fibrillation episodes based on 3D algebraic relationships between cardiac intervals," *Diagnostics*, vol. 12, no. 12, p. 2919, 2022.
- [120] R. LB, "Circulatory responses to upright posture," *Human Cardiovascular Control: Reflex Control During Orthostasis*, pp. 39-74, 1993.
- [121] L. Gargasas, A. Vainoras, H. Schwela, G. Jaruševičius, R. Ruseckas, and V. Miškinis, "JT interval changes during bicycle ergometry," *Kardiologia Polska: II międzynarodowy kongres Polskiego towarzystwa kardiologicznego: 4-6 września/September 1998, Katowice, Poland. Katowice., 1998, t. 49, supl. 1, abstract no. P153*, 1998.
- [122] F. Shaffer, R. McCraty, and C. L. Zerr, "A healthy heart is not a metronome: an integrative review of the heart's anatomy and heart rate variability," *Frontiers in psychology*, vol. 5, p. 1040, 2014.
- [123] R. McCraty, M. Atkinson, D. Tomasino, and R. T. Bradley, "The coherent heart heart-brain interactions, psychophysiological coherence, and the emergence of system-wide order," *Integral Review: A Transdisciplinary & Transcultural Journal for New Thought, Research, & Praxis*, vol. 5, no. 2, 2009.

- [124] S. C. Segerstrom and L. S. Nes, "Heart rate variability reflects self-regulatory strength, effort, and fatigue," *Psychological science*, vol. 18, no. 3, pp. 275-281, 2007.
- [125] G. Roukema, J. P. Singh, M. Meijis, C. Carvalho, and G. Hart, "Effect of exercise-induced ischemia on QT interval dispersion," *American heart journal*, vol. 135, no. 1, pp. 88-92, 1998.
- [126] M. Yoshimura, H. Yasue, and H. Ogawa, "Pathophysiological significance and clinical application of ANP and BNP in patients with heart failure," *Canadian journal of physiology and pharmacology*, vol. 79, no. 8, pp. 730-735, 2001.
- [127] M. Shahid, M. Ashraf, and S. S. Sharma, "StatPearls Publishing; Treasure Island, FL, USA: 2021," *Physiology, thyroid hormone*.[\[Google Scholar\]](#).
- [128] L. Gargasas, A. Vainoras, R. Ruseckas, R. Jurkonienė, V. Jurkonis, and V. Miskinis, "A new software for ECG monitoring system," in *6th Nordic Conference on eHealth and Telemedicine: Proceedings*, 2006: Citeseer, pp. 255-256.
- [129] R. Žumbakytė, A. Kajėnienė, and A. Vainoras, "Computerized evaluation of recovery phase in football and basketball players after bicycle stress test," *Clermont-Ferrand*, 2004, 2004.
- [130] P. Kligfield and M. S. Lauer, "Exercise electrocardiogram testing: beyond the ST segment," *Circulation*, vol. 114, no. 19, pp. 2070-2082, 2006.
- [131] P. M. Okin and P. Kligfield, "Heart rate adjustment of ST segment depression and performance of the exercise electrocardiogram: a critical evaluation," *Journal of the American College of Cardiology*, vol. 25, no. 7, pp. 1726-1735, 1995.
- [132] C. R. Cole, E. H. Blackstone, F. J. Pashkow, C. E. Snader, and M. S. Lauer, "Heart-rate recovery immediately after exercise as a predictor of mortality," *New England journal of medicine*, vol. 341, no. 18, pp. 1351-1357, 1999.
- [133] R. Lehtinen, H. Sievänen, J. Viik, V. Turjanmaa, K. Niemelä, and J. Malmivuo, "Accurate detection of coronary artery disease by integrated analysis of the ST-segment depression/heart rate patterns during the exercise and recovery phases of the exercise electrocardiography test," *The American journal of cardiology*, vol. 78, no. 9, pp. 1002-1006, 1996.
- [134] R. Žumbakytė, A. Kajėnienė, and A. Vainoras, "Computerized evaluation of recovery phase in women after bicycle test," in *1st Meeting of complex systems and sport & 4th International conference of computer science in sport: Barcelona, 14-17 May 2003*, 2003.
- [135] J. Poderys, A. Buliuolis, K. Poderytė, and R. Sadzevičienė, "Mobilization of cardiovascular function during the constant-load and all-out exercise tests," *Medicina*, vol. 41, no. 12, pp. 1048-1053, 2005.
- [136] R. Smidtaite, L. Saunoriene, and M. Ragulskis, "Detection of lag synchronization based on matrices of delayed differences," *Communications in Nonlinear Science and Numerical Simulation*, vol. 116, p. 106864, 2023.
- [137] D. Gu, Y. Mi, and A. Lin, "Application of time-delay multiscale symbolic phase compensated transfer entropy in analyzing cyclic alternating pattern (CAP) in sleep-related pathological data," *Communications in Nonlinear Science and Numerical Simulation*, vol. 99, p. 105835, 2021.
- [138] K. Berskiene *et al.*, "Analysis of dynamical interrelations of electrocardiogram parameters," *Elektronika ir elektrotechnika*, vol. 95, no. 7, pp. 95-98, 2009.
- [139] R. McCraty and F. Shaffer, "Heart rate variability: new perspectives on physiological mechanisms, assessment of self-regulatory capacity, and health risk," *Global advances in health and medicine*, vol. 4, no. 1, pp. 46-61, 2015.

- [140] S. Naghsh, M. Ataei, M. Yazdchi, and M. Hashemi, "Chaos-based analysis of heart rate variability time series in obstructive sleep apnea subjects," *Journal of Medical Signals and Sensors*, vol. 10, no. 1, p. 53, 2020.
- [141] K. Martinmäki and H. Rusko, "Time-frequency analysis of heart rate variability during immediate recovery from low and high intensity exercise," *European journal of applied physiology*, vol. 102, no. 3, pp. 353-360, 2008.
- [142] M. F. de Godoy, "Nonlinear analysis of heart rate variability: a comprehensive review," *Journal of Cardiology and Therapy*, vol. 3, no. 3, pp. 528-533, 2016.
- [143] V. Steven, "Heart Rate Variability: linear and non-linear analysis with applications in humans physiology," *Doctoral Thesis of Faculty of Electrical Engineering Kasteelpark Arenberg. Belgium*, 2010.
- [144] G. A. Fava, F. Cosci, J. Guidi, and E. Tomba, "Well-being therapy in depression: New insights into the role of psychological well-being in the clinical process," *Depression and anxiety*, vol. 34, no. 9, pp. 801-808, 2017.
- [145] M. A. Stewart, I. R. McWhinney, and C. W. Buck, "The doctor/patient relationship and its effect upon outcome," *The Journal of the Royal College of General Practitioners*, vol. 29, no. 199, pp. 77-82, 1979.
- [146] S. Del Canale *et al.*, "The relationship between physician empathy and disease complications: an empirical study of primary care physicians and their diabetic patients in Parma, Italy," *Academic medicine*, vol. 87, no. 9, pp. 1243-1249, 2012.
- [147] S. J. Guastello and L. S. Liebovitch, "Introduction to nonlinear dynamics and complexity," 2009.
- [148] R. V. Palumbo *et al.*, "Interpersonal autonomic physiology: A systematic review of the literature," *Personality and Social Psychology Review*, vol. 21, no. 2, pp. 99-141, 2017.
- [149] H. Azami and J. Escudero, "Improved multiscale permutation entropy for biomedical signal analysis: Interpretation and application to electroencephalogram recordings," *Biomedical Signal Processing and Control*, vol. 23, pp. 28-41, 2016.

## **CURRICULUM VITAE**

### **Personal information:**

Date of Birth: 20 November 1993.

Place of Birth: Peshawar, Pakistan.

### **Education:**

2012-2016 Bachelor of Science in Electrical Engineering, University of Engineering & Technology, (UET) Peshawar, Pakistan.

2018-2020 Master of Science in Energy Management and Sustainability, US- Pakistan Centre for Advanced Studies in Energy, (USPCASE) Peshawar, Pakistan.

2021-2025 Doctorate Studies in Informatics (N009), Department of Mathematical Modelling, Faculty of Mathematics and Natural Sciences, Kaunas University of Technology, Kaunas Lithuania.

### **Professional Experience:**

2019-2020 Lecturer in the Electrical Engineering Department in the City University of Science, Information & Technology (CUSIT), Peshawar Pakistan.

### **Research Area:**

Non-linear time series analysis, specifically the analysis of the interrelationship between and among the ECG signal to detect the short-term fluctuations for the cardiac disease detection and monitoring for the clinical applications.

## LIST OF PUBLICATIONS AND CONFERENCES

### Publications in Journals of the Institute of Scientific Information (ISI):

1. **Qammar, N. W.**, Orinaitė, U., Šiaučiūnaitė, V., Vainoras, A., Šakalytė, G., & Ragulskis, M. (2022). The complexity of the arterial blood pressure regulation during the stress test. *Diagnostics*, 12(5), 1-20. doi:10.3390/diagnostics12051256
2. **Qammar, Naseha Wafa;** Ragulskis, Minvydas; Saunoriene, Loreta; Smidtaite, Rasa; Vainoras, Alfonsas; Jaruševičius, Gediminas. Early diagnosis of problems related to the self-organization of the cardiovascular system based on the interplay between RR and JT cardiac intervals // *Diagnostics*. Basel: MDPI. ISSN 2075-4418. 2024, vol. 14, iss. 13, art. no. 1410, p. 1-22. DOI: 10.3390/diagnostics14131410
3. **Qammar, Naseha Wafa;** Vainoras, Alfonsas; Navickas, Zenonas; Jaruševičius, Gediminas; Ragulskis, Minvydas. Early diagnosis of atrial fibrillation episodes: comparative analysis of different matrix architectures // *Applied sciences*. Basel: MDPI. ISSN 2076-3417. 2024, vol. 14, iss. 14, art. no. 6191, p. 1-18. DOI: 10.3390/app14146191
4. **Qammar, N. W.**, Šiaučiūnaitė, V., Zabiela, V., Vainoras, A., & Ragulskis, M. (2022). Detection of atrial fibrillation episodes based on 3D algebraic relationships between cardiac intervals. *Diagnostics*, 12(12), 1-19. doi:10.3390/diagnostics12122919

### Conferences attended:

1. **Naseha Wafa Qammar.** *Understanding the Complexity of Arterial Blood Pressure Regulation Through the Lens of Perfect Matrices of Lagrange Differences* 65th Scientific and Technical Conference on Biomedical Engineering, Riga Technical University (RTU), Riga, Latvia, Date: April 22, 2024, Presentation Format: Oral presentation only.
2. **Naseha Wafa Qammar,** Minvydas Ragulskis, *Enhancing Atrial Fibrillation Detection: A Multifaceted Computational Approach Incorporating Higher-Order Perfect Matrices of Lagrange Differences (PMLD) and Decision Support Systems*, Poster presentation at Heart Rhythm Congress (HRC), International Convention Centre, Birmingham, UK, Date: October 7, 2024, Published in the *European Journal of Arrhythmia & Electrophysiology* (2024;10)

## ACKNOWLEDGEMENTS

First and foremost, my deepest gratitude is to the Almighty God for His guidance. I am profoundly thankful to my beloved late father, whose memory continues to inspire me every day. I owe special thanks to my mother, whose unwavering strength and support have sustained me throughout this journey and enabled me to reach this milestone.

I am sincerely and deeply grateful to my supervisor, Prof. Dr. Hab. Minvydas Ragulskis, whose indispensable mentorship and guidance have been vital throughout this journey. I am also sincerely thankful to the doctoral committee for their valuable feedback, which has played a pivotal role in shaping my thesis.

I would like to extend my heartfelt appreciation to my dissertation reviewers: Assoc. Prof. Dr. Mantas Landauskas, Prof. Dr. Kristina Berškienė and Prof. Dr. Dalia Čalnerytė, for their insightful and constructive comments, which have played a key role in improving and enhancing this dissertation.

My sincere thanks go to my colleagues in the Department of Mathematical Modelling for their support, pleasant communication, and valuable advice during my studies. I am equally grateful to the staff and editors of the Doctoral School administration for their assistance and guidance throughout this process.

Finally, my heartfelt thanks go to my siblings, whose love, motivation, and constant encouragement helped me through every challenge along the way.

## ANNEX

### A. Bioethical permit BE-1-30 (Original)



#### KAUNO REGIONINIS BIOMEDICININIŲ TYRIMŲ ETIKOS KOMITETAS

Lietuvos sveikatos mokslų universitetas, A. Mickevičiaus g. 9, LT 44307 Kaunas, tel. (+370) 37 32 68 89, el. paštas: kaunorbtek@lsmuni.lt

#### LEIDIMAS ATLIKTI BIOMEDICININĮ TYRIMĄ

2020-06-02 Nr. BE-1-30

<b>Biomedicininio tyrimo pavadinimas: „Invazinio arterinio kraujo spaudimo monitoravimo nauda gydamosios vainikinių arterijų intervencijos sėkmingumo bei pacientų išgyvenamumo ir gyvenimo kokybės vertinimui“.</b>	
Protokolo Nr.:	<b>PulseWave20</b>
Data:	<b>2020-04-01</b>
Versija:	<b>1.0</b>
Asmens informavimo forma	<b>Versija 1.0, data 2020-04-01</b>
Pagrindinis tyrėjas:	<b>Gediminas Jaruševičius</b>
Biomedicininio tyrimo vieta:	<b>LSMU Kardiologijos klinika</b>
Ištaigos pavadinimas:	<b>Eivenių g. 2, LT 50140 Kaunas</b>
Adresas:	

#### Išvada:

Kauno regioninio biomedicininis tyrimų etikos komiteto posėdžio, įvykusio **2020 m. birželio mėn. 2 d.** (protokolo Nr. BE-10-6) sprendimu pritarta biomedicininio tyrimo vykdymui.

Mokslinio eksperimento vykdytojai įsipareigoja: (1) nedelsiant informuoti Kauno Regioninį biomedicininis Tyrimų Etikos komitetą apie visus nenumatytus atvejus, susijusius su studijos vykdymu, (2) iki sausio 15 dienos – pateikti metinį studijos vykdymo apibendrinimą bei, (3) per mėnesį po studijos užbaigimo, pateikti galutinį pranešimą apie eksperimentą.

Kauno regioninio biomedicininis tyrimų etikos komiteto nariai			
Nr.	Vardas, Pavardė	Veiklos sritis	Dalyvavo posėdyje
1.	Prof. Edgaras Stankevičius	Fiziologija, farmakologija	Taip
2.	Prof. Skaidrus Miliuskas	Pulmonologija, vidaus ligos	Taip
3.	Med. dr. Jonas Andriuskevičius	Chirurgija	Taip
4.	Doc. Gintautas Gumbrevičius	Klinikinė farmakologija	Taip
5.	Prof. Kęstutis Petrikonis	Neurologija	Taip
6.	Dr. Ramunė Kasperavičienė	Filologija	Taip
7.	Zydrūnė Luneckaitė	Visuomenės sveikata	Taip
8.	Aušra Degutytė	Visuomenės sveikata	Taip
9.	Jurgita Laurinaitė	Teisė	Ne

Kauno regioninis biomedicininis tyrimų etikos komitetas dirba vadovaudamasis etikos principais nustatytais biomedicininis tyrimų Etikos įstatyme, Helsinkio deklaracijoje, vaisingų tyrimų Geros klinikinės praktikos taisyklėmis.

Kauno RBTEK pirmininkas

Prof. Edgaras Stankevičius



## B. Bioethical permit BE-1-30 (Translated)



*Translation from Lithuanian*

### KAUNAS REGIONAL BIOMEDICAL RESEARCH ETHICS COMMITTEE

Lithuanian University of Health Sciences, A. Mickevičiaus St. 9, LT 44307 Kaunas, tel. (+370) 37 32 68 89; e-mail: kaunorbttek@lsmun.lt

#### A PERMIT TO CONDUCT BIOMEDICAL RESEARCH

06/02/2020 No. BE-1-30

<b>Title of the biomedical research:</b> "The benefit of invasive arterial blood pressure monitoring for the assessment of success of therapeutic coronary intervention and patient survival and quality of life".	
Protocol No.:	<b>PulseWave20</b>
Date:	<b>04/01/2020</b>
Version:	<b>1.0</b>
Form for informing the person	<b>Version 1.0, date 04/01/2020</b>
Lead researcher:	<b>Gediminas Jaruševičius</b>
Place of biomedical research:	<b>LUHS Cardiology clinics</b>
Name of the institution:	<b>Eivenių St. 2, LT 50140 Kaunas</b>
Address:	

#### Opinion:

By the decision of the Kaunas Regional Biomedical Research Ethics Committee meeting held on **2 June 2020** (Protocol No BE-10-6), the biomedical research was approved.

The participants of the scientific experiment are obliged to: (1) immediately inform the Kaunas Regional Biomedical Research Ethics Committee of any unforeseen events related to the conduct of the study, (2) submit an annual summary of the conduct of the study by 15 January, and (3) submit a final report on the experiment within one month of the completion of the study.

Members of the Kaunas Regional Biomedical Research Ethics Committee			
No.	Full name	Field of activity	Participated in the meeting
1.	Prof. Edgaras Stankevičius	Physiology, pharmacology	Yes
2.	Prof. Skaidrius Miliauskas	Pulmonology, internal medicine	Yes
3.	MD-PhD Jonas Andriuskevicius	Surgery	Yes
4.	Assoc. Prof. Gintautas Gumbrevičius	Clinical pharmacology	Yes
5.	Prof. Kęstutis Petrikonis	Neurology	Yes
6.	PhD Ramunė Kasperavičienė	Philology	Yes
7.	Zydrūnė Luneckaitė	Public health	Yes
8.	Aušra Degutytė	Public health	Yes
9.	Jurgita Laurinaitytė	Law	No

Kaunas Regional Biomedical Research Ethics Committee works in accordance with the ethical principles set out in the Law on Ethics in Biomedical Research, the Declaration of Helsinki, and the Rules of Good Clinical Practice for Drug Research.

President of Kaunas RBREC

/Signature/

Prof. Edgaras Stankevičius

/Round stamp: LITHUANIAN UNIVERSITY OF HEALTH SCIENCES\*KAUNAS REGIONAL BIOMEDICAL RESEARCH ETHICS COMMITTEE/

*The translation is true, accurate, and correct "to the best of my knowledge and ability". I take responsibility for the correctness of translation from Lithuanian to English: translator Jolanta Kvačkaitė, licence No. 762313, residing at Rygos St. 21-11, Vilnius, Lithuania.*

04/01/2024

*Jolanta Kvačkaitė*



## C. Bioethical permit BE-2-4 (Original)



KAUNO REGIONINIS BIOMEDICININIŲ TYRIMŲ ETIKOS KOMITETAS  
Lietuvos sveikatos mokslų universitetas, A. Mickėvičiaus g. 9, LT-44307 Kaunas, tel. (+370) 37 32 68 89; el. paštas: kaunortek@tsumuni.lt

### LEIDIMAS ATLIKTI BIOMEDICININĮ TYRIMĄ

2016-03-15 Nr. BE-2-4

Biomedicininio tyrimo pavadinimas:	"Veiksniai sąlygojantys sinusinio ritmo ilgalaikiškumą po elektrinės kardioversijos dėl persistentinio prieširdžių virpėjimo: integruotas klinikinių laboratorinių ir vaizdinių rodiklių vertinimas"
Protokolo Nr.:	12/2015
Data:	2015-12-01
Versija:	I
Asmens informavimo forma	Versija Nr. 2, 2016-01-11
Pagrindinis tyrėjas:	Prof. Aušra Kavolūnienė
Biomedicininio tyrimo vieta:	LSMUL VŠĮ Kauno klinikos,
Ištaigos pavadinimas:	Kardiologijos klinika
Adresas:	Eivenių g. 2, LT-50009, Kaunas, Lietuva

#### Išvada:

Kauno regioninio biomedicininio tyrimų etikos komiteto posėdžio, įvykusio 2016 m. sausio mėn. 5 d. (protokolo Nr. BE-10-4) sprendimu pritarta biomedicininio tyrimo vykdymui.

Mokslinio eksperimento vykdytojai įsipareigoja: (1) nedelsiant informuoti Kauno Regioninį biomedicininio Tyrimų Etikos komitetą apie visus nenumatytus atvejus, susijusius su studijos vykdymu, (2) iki sausio 15 dienos – pateikti metinį studijos vykdymo apibendrinimą bei, (3) per mėnesį po studijos užbaigimo, pateikti galutinį pranešimą apie eksperimentą.

Kauno regioninio biomedicininio tyrimų etikos komiteto nariai			
Nr.	Vardas, Pavardė	Veiklos sritis	Dalyvavo posėdyje
1.	Prof. Romaldas Mačiulaitis	Klinikinė farmakologija	taip
2.	Prof. Edgaras Stankevičius	Fiziologija, farmakologija	taip
3.	Doc. Eimantas Pečiūš	Filosofija	taip
4.	Dr. Ramunė Kasperavičienė	Kabotvra	taip
5.	Med. dr. Jonas Andriuskevičius	Chirurgija	taip
6.	Agnė Krūšinskaitė	Teisė	taip
7.	Prof. Skaidrius Miliauskas	Pulmonologija, vidaus ligos	taip
8.	Med. dr. Rokas Bagdonas	Chirurgija	ne
9.	Eglė Vaižgelienė	Visuomenės sveikata	taip

Kauno regioninis biomedicininis tyrimų etikos komitetas dirba vadovaudamasis etikos principais nustatytais biomedicininio tyrimų Etikos įstatyme, Helsinkio deklaracijoje, vaisių tyrinėjimo Geros klinikinės praktikos taisyklėmis.

Pirmininkas

Prof. Romaldas Mačiulaitis



UDK 004.421.2+616.12-073.7] (043.3)

SL344. 2021-\*-\* , \* leidyb. apsk. 1. Tiražas 14 egz. Užsakymas \*.

Išleido Kauno technologijos universitetas, K. Donelaičio g. 73, 44249 Kaunas  
Spausdino leidyklos „Technologija“ spaustuvė, Studentų g. 54, 51424 Kaunas